INSTITUTO TECNOLÓGICO
Y DE ESTUDIOS SUPERIORES DE OCCIDENTE

Reconocimiento de validez oficial de estudios de nivel superior según acuerdo secretarial 15018, publicado en el Diario Oficial de la Federación el 29 de noviembre de 1976.

Departamento de Electrónica, Sistemas e Informática

DOCTORADO EN CIENCIAS DE LA INGENIERÍA

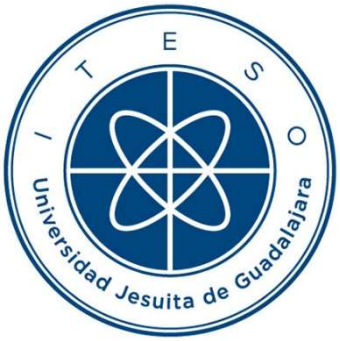

DISEÑO DE DETECTORES GFSK DE BAJA COMPLEJIDAD PARA DISPOSITIVOS IoT BLE

Tesis que para obtener el grado de

DOCTOR EN CIENCIAS DE LA INGENIERÍA

presenta: José María Valencia Velasco

Director de tesis: Dr. Omar Humberto Longoria Gándara

Tlaquepaque, Jalisco. Diciembre de 2020

DOCTOR EN CIENCIAS DE LA INGENIERÍA (2020) ITESO, Tlaquepaque, Jal., México

TÍTULO: **Diseño de detectores GFSK de baja complejidad para dispositivos IoT BLE**

AUTOR: José María Valencia Velasco
Ingeniero en Electrónica (CETI, México)
Maestro en Diseño Electrónico (ITESO, México)

DIRECTOR DE TESIS: Omar Humberto Longoria Gándara
Departamento de Electrónica, Sistemas e Informática, ITESO
Ingeniero en Electrónica y Comunicaciones (ITESM, Campus Monterrey, México)
Maestro en Ciencias de Ingeniería Eléctrica, opción Telecomunicaciones (CINVESTAV, México)
Doctor en Ciencias de Ingeniería Eléctrica, opción Telecomunicaciones (CINVESTAV, México)

NÚMERO DE PÁGINAS: xxv, 102

ITESO – The Jesuit University of Guadalajara

Department of Electronics, Systems, and Informatics

DOCTORAL PROGRAM IN ENGINEERING SCIENCES

DESIGN OF LOW-COMPLEXITY GFSK DETECTORS FOR IOT BLE DEVICES

Thesis to obtain the degree of

DOCTOR IN ENGINEERING SCIENCES

Presents: José María Valencia Velasco

Thesis Director: Dr. Omar Humberto Longoria Gándara

Tlaquepaque, Jalisco, Mexico
December 2020

PHD IN ENGINEERING SCIENCES (2020) ITESO, Tlaquepaque, Jal., Mexico

TITLE: **Title of the Doctoral Thesis in English (Notice that the Title here is in English Title Style)**

AUTHOR: José María Valencia-Velasco
Bachelor´s degree in electronics (CETI, México)
Master's degree in electrical engineering (ITESO, México)

THESIS DIRECTOR: Omar Humberto Longoria-Gándara
Department of Electronics, Systems, and Informatics, ITESO
Bachelor's degree in electronics engineering (ITESM, Mexico)
Master's degree in electrical engineering (CINVESTAV, Mexico)
Ph.D. degree in electrical engineering (CINVESTAV, Mexico)

NUMBER OF PAGES: xxv, 102

This thesis is dedicated to:

My wife Beatriz and my children María José, Natalia, and Emiliano, whose unconditional love, patience, and support allow me to complete this thesis.

My parents José María and Francisca, for their complete support and their words of encouragement.

My sister Angeles and my brothers Francisco Ignacio and Gerardo, for always being present at all times.

Resumen

Internet de las cosas (IoT, por sus siglas en inglés) es una tecnología que ha crecido demasiado y cuyo interés radica en la conexión de diversos tipos de dispositivos para recopilar e intercambiar datos. Dado que la mayoría de los dispositivos de IoT son móviles, los recursos de hardware son bastante limitados. Por tanto, la reducción de la complejidad es relevante en este contexto. El estándar Bluetooth de bajo consumo (BLE, por sus siglas en inglés) ocupa un lugar importante en IoT debido a que emplea modulación por desplazamiento de frecuencia Gaussiano (GFSK, por siglas en inglés) en la capa física, lo que proporciona una eficiencia espectral y energética bastante aceptables. Sin embargo, debido a la naturaleza no lineal de la modulación GFSK, la complejidad de los detectores GFSK es alta. En esta tesis doctoral se proponen dos novedosos detectores GFSK de baja complejidad: en el primer detector se obtiene una estimación de los símbolos transmitidos a partir de un modelo lineal que se basa en el sobremuestreo de la señal GFSK y que, por su linealidad, la complejidad de su implementación es baja. La segunda propuesta se basa en un nuevo paradigma que transforma la señal de banda base I-Q y utiliza las métricas propuestas de baja complejidad en el algoritmo Viterbi. Los resultados teóricos y simulados muestran un desempeño muy cercano al receptor Viterbi subóptimo bajo un modelo de canal de ruido blanco Gaussiano aditivo (AWGN, por sus siglas en inglés). Adicionalmente, los detectores cumplen con las especificaciones del estándar Bluetooth. Por lo tanto, los detectores propuestos resultan atractivos para dispositivos IoT BLE.

Summary

The Internet of Things (IoT) is a technology that has overgrown and whose interest lies in the connection of diverse kinds of devices to collect and exchange data. Since most IoT devices are mobile, the hardware resources are hard-limited. Thus, complexity reduction becomes a relevant concern in this context. Bluetooth low energy (BLE) communication standard has an essential position in IoT due to its Gaussian frequency shift keying (GFSK) modulation scheme employed in the physical layer, which provides both attractive spectral and power efficiency. However, due to the nonlinear nature of GFSK signaling, the complexity of the GFSK detectors is high. In this doctoral dissertation, two novel low-complexity GFSK detectors are proposed: the first detector presented obtains an estimation of the transmitted symbols from a linear data model based on oversampling the GFSK signal and, because of its linearity, has a low-complexity implementation. The second proposal is based on a new paradigm that transforms the I-Q baseband signal and uses the Viterbi algorithm with a reduced-complexity proposed metrics. Theoretical and simulated results show a performance close to the near-optimal Viterbi receiver in the additive white Gaussian noise (AWGN) channel model. The proposed detectors are an attractive scheme for IoT BLE devices since the Bluetooth standard is complied.

Acknowledgments

The author wishes to express his sincere appreciation to Dr. Omar Humberto Longoria-Gándara, professor of the Department of Electronics, Systems, and Informatics at ITESO, for his encouragement, expert guidance, valuable support, and keen supervision as doctoral thesis director throughout this work. The author offers his gratitude to Dr. Arturo Veloz-Guerrero, Dr. Javier Vázquez-Castillo, Dr. Abisai Ramírez-Peréz and Dr. José Luis Pizano-Escalante, members of his Ph.D. Thesis Committee for their interest, assessment, and suggestions.

I want to give special thanks to Rodrigo Aldana for their cooperation, valuable support, and helpful technical discussions.

The author gratefully acknowledges the financial assistance through the scholarship (CVU 625492) granted by the Consejo Nacional de Ciencia y Tecnología (CONACYT), Mexican Government.

Finally, special thanks are due to my family: my wife Beatriz and my children María José, Natalia, and Emiliano. My parents José María and Francisca, my sister Angeles, and my brothers Francisco Ignacio, and Gerardo for their understanding, patience, and continuous loving support.

Contenido

Contents

List of Figures

List of Tables

Introduction

Communications systems can be classified in terms of four kinds of efficiencies: radio spectrum utilization (bandwidth efficiency), bit error rate (BER) efficiency (noise immunity), power efficiency (link budget, selection of the amplifiers and the number of antennas), and cost efficiency (low hardware and software resources in transmitters and receivers). The design of wireless communication systems implies a trade-off between these four categories, the environment and the use case required, e.g., telemetry in aerospace applications, telephony, or the Internet of Things (IoT) applications. The selection of a specific digital modulation technique mainly impacts the spectrum utilization and the cost parameters.

Continuous phase modulation (CPM) [Sundberg-86] is a class of digital modulation that includes frequency-shift keying (FSK) and phase-shift keying (PSK) techniques with constant envelope and a signal phase constrained to be continuous, which provide both power and bandwidth efficiency [Proakis-08], [Xiong-06].

Industrial communications standards have confirmed the efficiency of CPM techniques. For example, MILSTD-188-181B for voice-over-satellite communications [Peterson-02] uses the dual-h CPM, IRIG-106-15 aeronautical telemetry standard [Telemetry Group-16] uses CPFSK and Bluetooth low energy (BLE) standard, uses Gaussian FSK (GFSK).

Optimal receivers for CPM detectors use a maximum-likelihood sequence estimator (MLSE), whose implementation is prohibitive in various applications due to the high amount of hardware resources required. In this sense, the complexity reduction in the implementation of the receiver, while the bandwidth efficiency and noisy immunity are conserved, is of particular interest.

In this doctoral dissertation, the complexity reduction problem in GFSK detectors is addressed. Then, two novel linear GFSK demodulators which are compatible with IoT devices and with a reduced complexity implementation are proposed.

In the first proposal, an estimation of the transmitted symbols is obtained based on the linear data model detailed in [Liang-97], which oversamples the GFSK signal and neglects the nonlinear terms. The proposed demodulator has the following attractive features: i) because of its linearity, it has a structure with low complexity; ii) the performance is very close to the near-

optimal Viterbi receiver in the additive white Gaussian noise (AWGN) channel model; iii) its structure allows it to operate with both the "exact" (direct generation of GFSK signals) and linear modulators described in [Liang-97].

In the second proposal, a GFSK receiver based on a new paradigm that transforms the I (in-phase) and Q (quadrature) components of the baseband signal is presented. The transformation consists of quantizing the baseband components with the values $+1$ and -1. This processing allows the use of two simplified metrics in the implementation of the Viterbi algorithm. The proposed metrics attain a reduction of computational complexity and hardware resources.

Since most IoT devices are mobile, the hardware resources are hard-limited. Therefore, complexity reduction becomes a relevant concern in this context. Under these circumstances, the proposals are very engaging since less memory, and arithmetic blocks are required, which means a complexity reduction in the hardware implementation. Theoretical and simulated results, under the additive white Gaussian noise (AWGN) channel, corroborate the evidence that the proposals comply with BLE performance in terms of BER.

This document is organized as follows: in Chapter 1 is presented the system model that describes the GFSK digital modulation. Chapter 2 is focused on the theoretical GFSK error performance, and the expression that describes it is obtained. In Chapter 3 are described two linear approximations of the GFSK signals: the Laurent decomposition (LD) and the Liang-Paulraj approach. Chapter 4 describes the design of two novel reduced-complexity detectors, which are based on the Liang-Paulraj approach and in the transformation of the in-phase (I) and quadrature (Q) components of the baseband GFSK signal. Theoretical and simulated error performance is presented and compared with Viterbi-based and BPSK detectors. Finally, in Chapter 5 is presented an introduction to the space-time diversity techniques for CPM signaling, and some interesting research in this area is also presented.

1. GFSK Signal Model

Continuous phase FSK (CPFSK) is a CPM subclass oriented to bandwidth conservation (spectral efficiency) with constant-envelope behavior (hence its robustness to nonlinear impairments), fixed modulation index and memory (which derive in a high-complexity implementation) due to its continuous phase. According to the shape and the modulation index of the baseband digital signal used in CPFSK, it is possible to have different schemes such as Minimum Shift Keying (MSK) and Gaussian FSK (GFSK) with rectangular and Gaussian pulse shaping, respectively.

1.1. The Importance of GFSK in the Context of IoT

The Internet of Things (IoT) is a leading-edge technology that allows connecting a variety of devices with the purpose of interchange information without human intervention [Chen-14]. Among the wide range of communication standards used by these devices, Bluetooth low energy (BLE) has gained special attention due to its low power consumption [Zanella-14], [Collota-18]. The BLE standard specification establishes Gaussian frequency shift keying (GFSK) as modulation scheme at the physical layer [S.I.G. Bluetooth-19]. This modulation scheme is attractive due to its spectral efficiency, and that allows the power amplifiers to operate in an efficient way, which results in extended battery life.

Under this scenario, GFSK plays an essential role in wireless communications technology. Thus, studies and research focused on improving performance and reducing complexity implementation of GFSK communication systems are of particular interest.

1.2. Description of the GFSK Signal

In Fig. 1.1, the general block diagram of a GFSK communications system is shown; the first part of the system is a differential encoder that converts the input symbols $\{s_0, s_1, ..., s_n\}$ into symbols $\{\alpha_0, \alpha_1, ..., \alpha_n\}$ that are defined as follows:

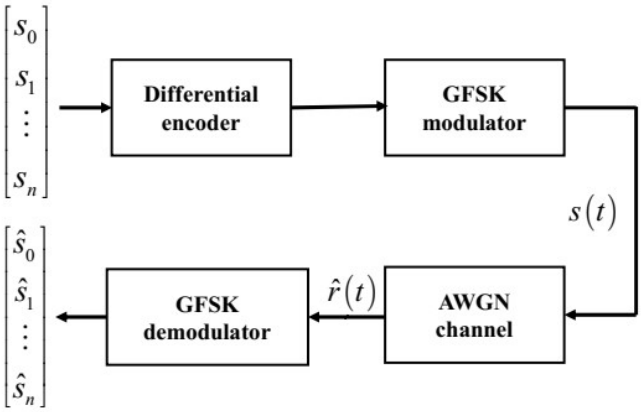

Fig. 1.1 General block diagram of a communication system with GFSK modulation.

$$\alpha_n = \begin{cases} s_n s_{n-1} & , n > 0 \\ s_0 & , n = 0 \end{cases} \tag{1-1}$$

where $s_n \in \{+1, -1\}$ and $\alpha_n \in \{+1, -1\}$.

The GFSK modulator, represented in Fig. 1.2a and described in [Anderson-86], takes the symbols α_n and generates a pulse train $p(t)$ defined as

$$p(t) = \sum_n \alpha_n g(t - nT) \tag{1-2}$$

where $n \in \mathbb{Z}$, T represents the symbol-time duration and $g(t)$ is the pulse-shaping based on a Gaussian function described as

$$g(t) = \frac{1}{2T}\left[Q\left(2\pi BT \left(\frac{t - T/2}{\sqrt{\ln(2)}T} \right) \right) - Q\left(2\pi BT \left(\frac{t + T/2}{\sqrt{\ln(2)}T} \right) \right) \right] \tag{1-3}$$

where B is the $-3dB$ bandwidth, BT is the bandwidth-time product and $Q(t)$ is the Q-function defined as

$$Q(t) = \frac{1}{\sqrt{2\pi}} \int_t^{\infty} \exp\left(-\tau^2 / 2\right) d\tau \tag{1-4}$$

The signal $p(t)$ in (1-2) is integrated and used to modulate a complex exponential, generating what is called the baseband form or complex envelope of the GFSK signal:

$$s(t) = \exp\left(j2\pi\lambda \int_{-\infty}^{t} p(\tau) d\tau \right) = \exp\left(j\varphi(t) \right) \tag{1-5}$$

in which λ is the modulation index and

$$\varphi(t) = 2\pi\lambda \int_{-\infty}^{t} p(\tau)d\tau \tag{1-6}$$

represents the phase signal, as is described in [Proakis-08]. The modulation index is defined as

$$\lambda = 2T\Delta_f \tag{1-7}$$

For example, in BLE, the nominal value of λ is 0.5. Then, the maximum frequency deviation is $\Delta_f = \frac{1}{4T}$.

In Fig. 1.3 is shown the shape of $g(t)$ for various values of BT with a pulse duration L of 6 symbol periods. It is important to note that $g(0) = \frac{1}{2T}$ for $BT \to \infty$ and the pulse duration is only one symbol period, that corresponds to the full-response CPM. In the case of BLE, $BT = 0.5$ and the duration of $g(t)$ is approximately $3T$, this is known as partial-response CPM signaling. For instance, MSK modulation scheme is a full-response CPM signaling with rectangular pulse shaping and $\lambda = 0.5$. The power spectrum density of MSK and GFSK is shown in Fig. 1.4. It is worth noting that GFSK signal has better spectral efficiency than MSK due to the Gaussian pulse shaping.

The scheme presented in Fig. 1.2b shows an alternative generation of $s(t)$, which is based on [Rappaport-02]. In this approach, $p(t)$ is described as

$$p(t) = \sum_n \alpha_n \prod_T (t - nT) * h(t) \tag{1-8}$$

where * indicates the convolution operator, $\prod_T(t)$ represents a square pulse defined as

$$\prod_T(t) = \begin{cases} 1/T & for \quad |t - T/2| < 0 \\ 0 & otherwise \end{cases} \tag{1-9}$$

and $h(t)$ is the impulse response of a Gaussian filter expressed as

$$h(t) = \frac{1}{\sqrt{2\pi}\sigma_h T} \exp\left(\frac{-t^2}{2\sigma_h{}^2 T^2}\right) \tag{1-10}$$

where $\sigma_h = \frac{\sqrt{\ln(2)}}{2\pi BT}$.

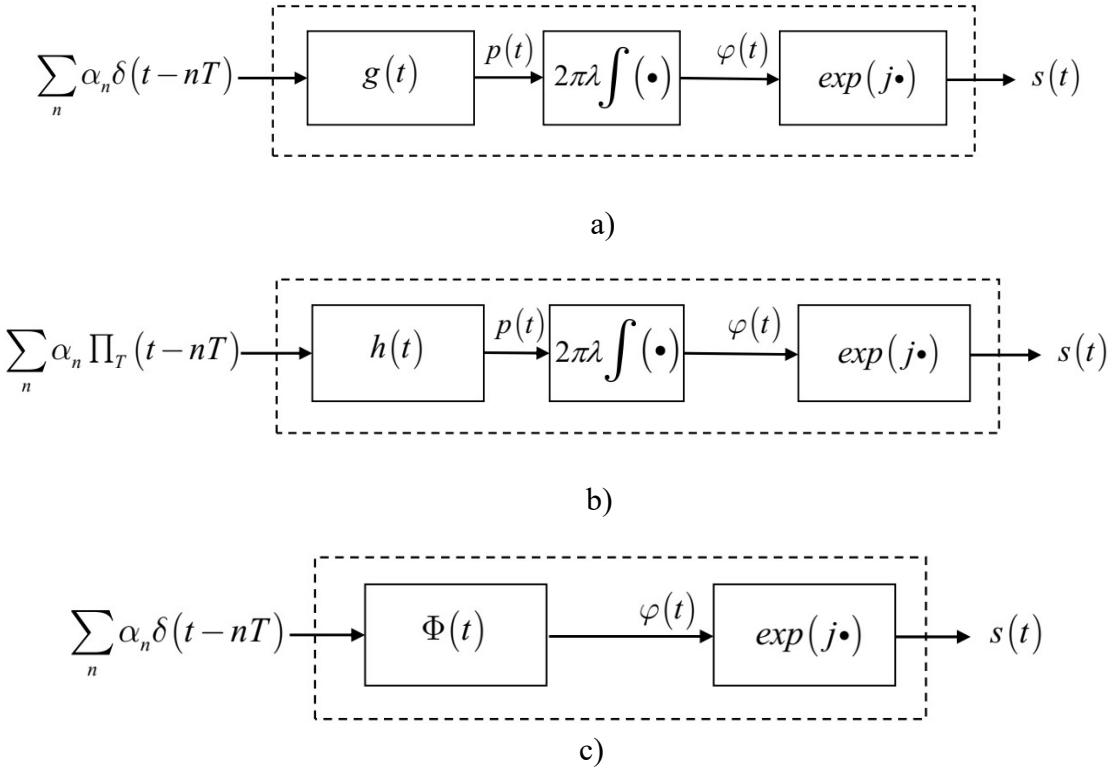

Fig. 1.2 Baseband model for three different approaches of GFSK modulators with: a) $g(t)$ pulse shaping; b) $h(t)$ pulse shaping; c) $\Phi(t)$ pulse shaping.

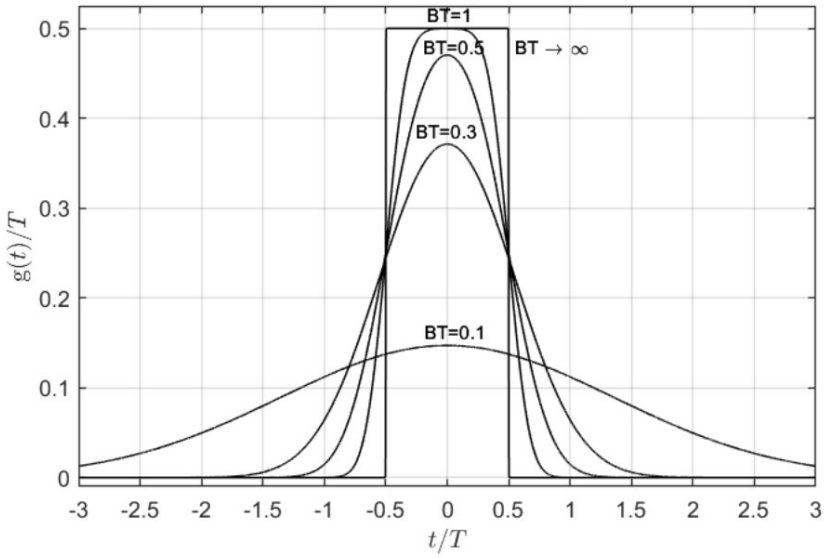

Fig. 1.3 Pulse shaping $g(t)$ for different values of BT .

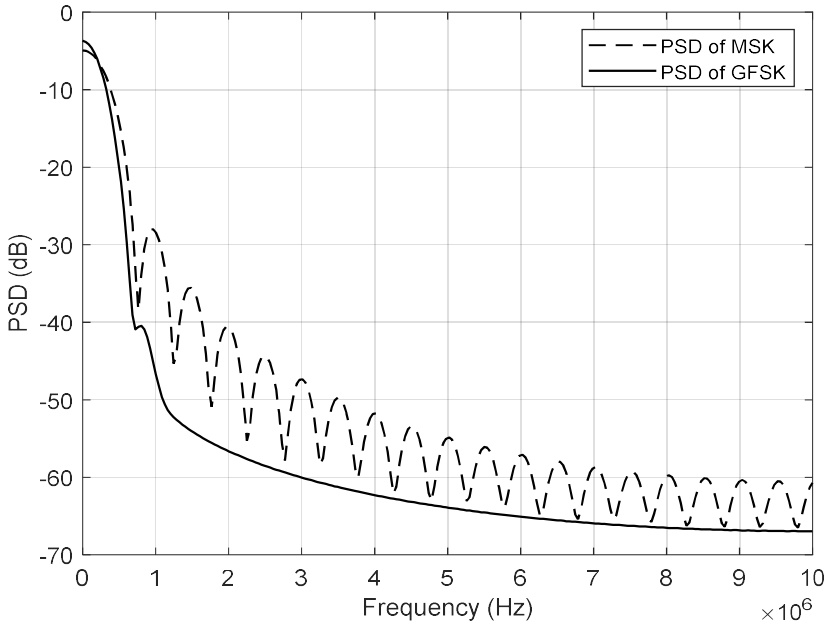

Fig. 1.4 Power spectral density of MSK and GFSK. It can be noted a spectrum efficiency improvement in the last one.

Another implementation for generating $s(t)$ is based on [Liang-97], and it can be obtained as follows. Let a function be defined as

$$\Phi(t) = 2\pi\lambda \int_{-\infty}^{t} g(\tau)\, d\tau \tag{1-11}$$

According to Fig. 1.2c, the phase signal, $\varphi(t)$, is expressed as

$$\varphi(t) = \sum_{n} \alpha_n \Phi(t - nT) \tag{1-12}$$

that is equivalent to the previous two schemes. Due to the definition of $g(t)$ given in (1-3), then

$$\int_{-\infty}^{\infty} g(\tau)\, d\tau = \frac{1}{2} \tag{1-13}$$

Considering (1-11) with the modulation index for BLE, $\lambda = 0.5$, and (1-13) then

$$\lim_{t\to\infty} \Phi(t) = \frac{\pi}{2} \tag{1-14}$$

Thus, $\Phi(t) = 0$ for $t \to -\infty$ and $\Phi(t) = \pi/2$ for $t \to \infty$, resulting in a sigmoid function that is shown in Fig. 1.5. In this way, each value of α_n causes a phase change of $\pi/2$ and $-\pi/2$ for the

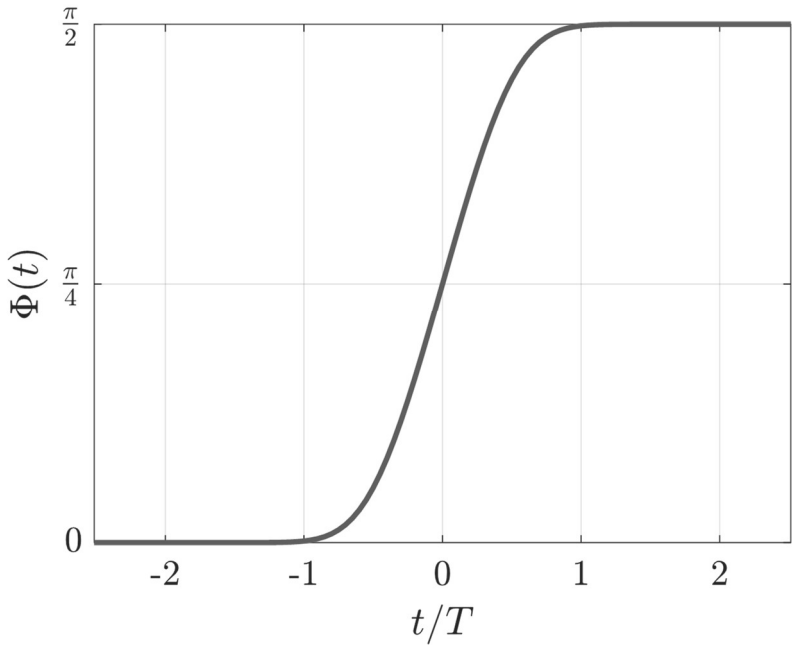

Fig. 1.5 Sigmoid function $\Phi(t)$ used in Fig. 1.2c.

values $+1$ and -1, respectively, as is illustrated in Fig. 1.6.

The signals of the GFSK implementations presented in Fig. 1.2a, Fig. 1.2b, and Fig. 1.2c are depicted in Fig. 1.7, Fig. 1.8, and Fig. 1.9, respectively. It can be noted that the output signals are identical for the same input data stream. Thus, the equivalence of these implementations is established.

Using any GFSK baseband signal of the three implementations showed in Fig. 1.2, the received signal under AWGN channel is given by

$$r(t) = s(t) + \eta(t) \tag{1-15}$$

with $\eta(t)$ being a complex white Gaussian noise, a mean of zero and a variance of $\sigma^2 = N_0 / 2$ per real and imaginary dimension.

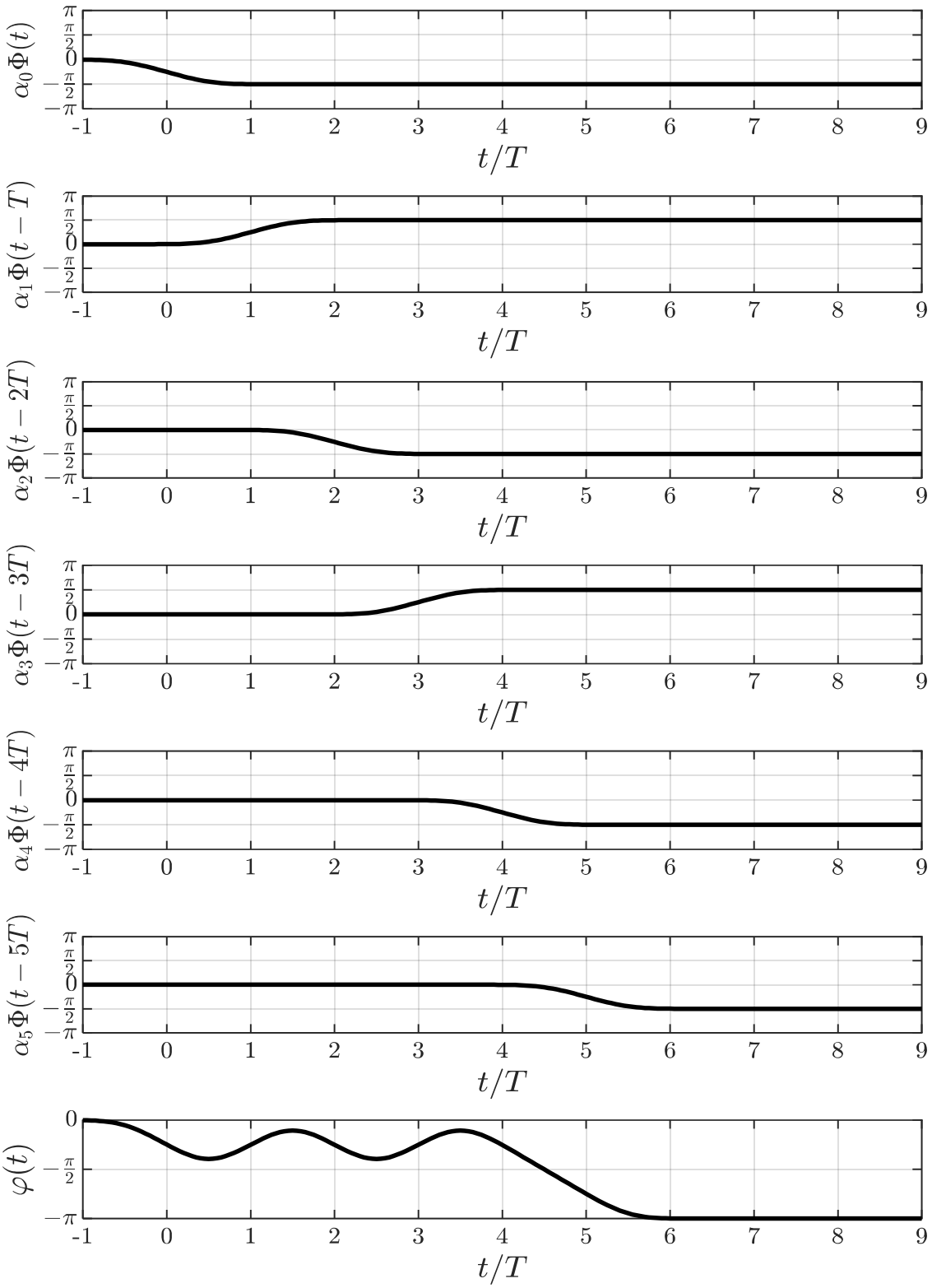

Fig. 1.6 Phase changes of $\varphi(t)$ according to the expression (1-12) and the sequence $\alpha_n = \{-1,1,-1,1,-1,-1\}$.

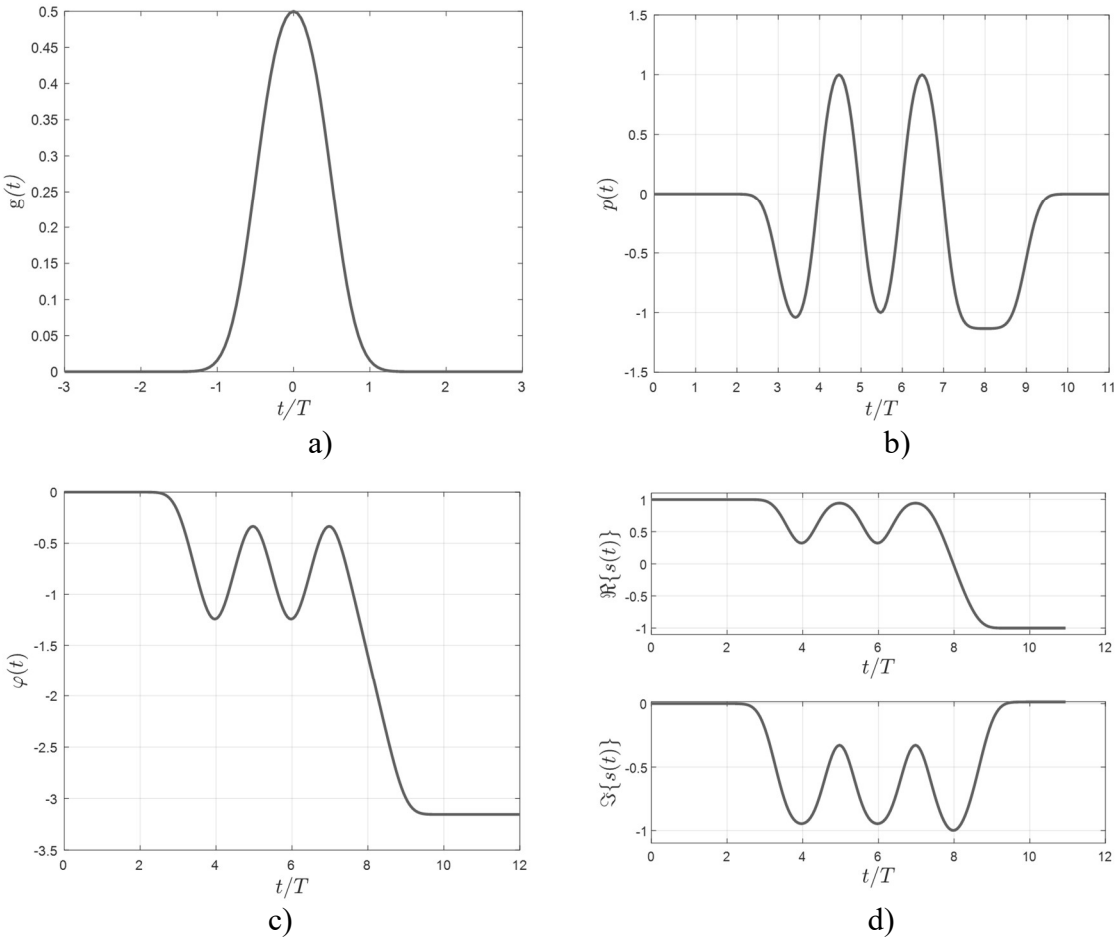

Fig. 1.7 Signals of the GFSK implementation described in Fig. 2a: a) Gaussian pulse $g(t)$; b) pulse train $p(t)$; c) phase signal $\varphi(t)$ for a sequence $\alpha_n = \{-1,1,-1,1,-1,-1\}$; d) real and imaginary part of the baseband GFSK signal, $s(t)$.

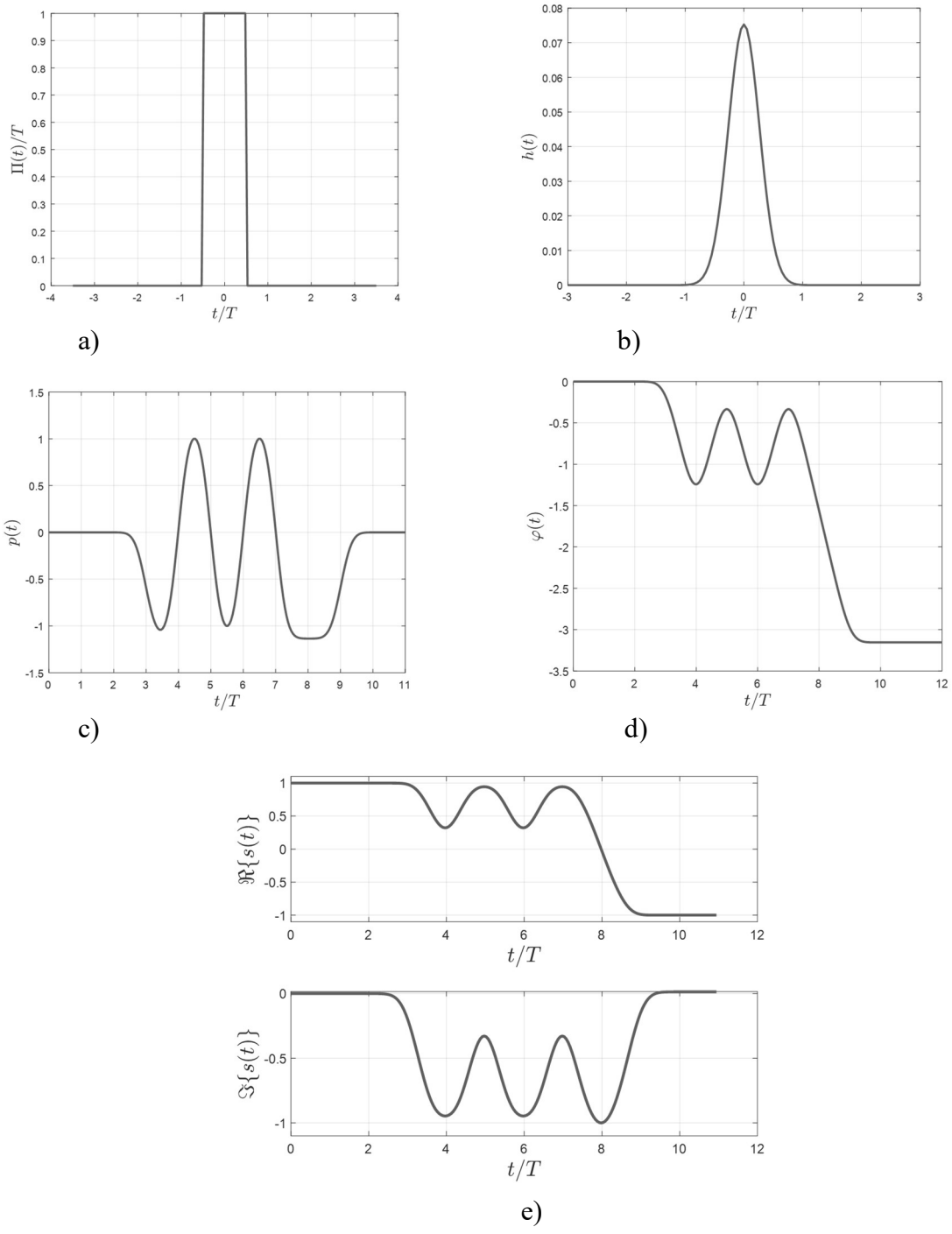

Fig. 1.8 Signals of the GFSK implementation described in Fig. 2b: a) squared pulse $\Pi_T(t)$; b) impulse response of the Gaussian filter $h(t)$; c) pulse train $p(t)$; d) phase signal $\varphi(t)$ for a sequence $\alpha_n = \{-1,1,-1,1,-1,-1\}$; e) the real and imaginary part of the baseband GFSK signal, $s(t)$.

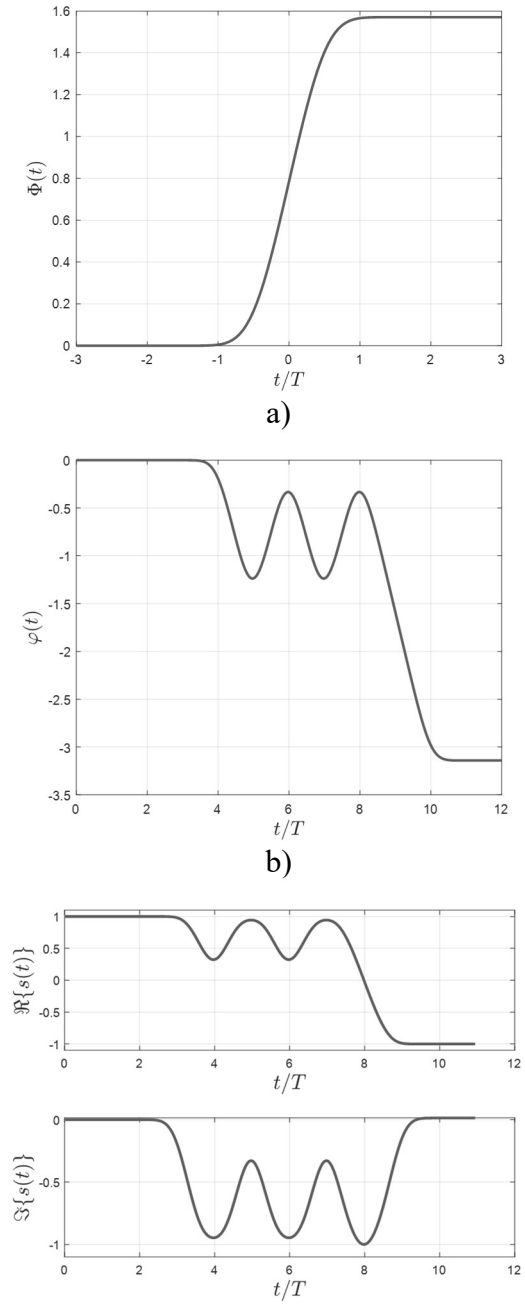

Fig. 1.9 Signals of the GFSK implementation described in Fig. 2c: a) $\Phi(t)$ pulse; b) phase signal $\varphi(t)$ for a sequence $\alpha_n = \{-1,1,-1,1,-1,-1\}$; c) the real and imaginary part of the baseband GFSK signal, $s(t)$.

1.3. Conclusions

In this Chapter, the importance of the GFSK modulation scheme in the context of IoT was described. Due to its spectral and error performance efficiencies, the GFSK modulation scheme is used in a wide variety of BLE communications devices

The GFSK system model was presented and, three different alternatives used to represent the GSFK signal were described. The equivalence of the three approaches is verified since the output signals match perfectly for the same input data sequence. In addition, it was shown that the GFSK signal is entirely defined by the phase signal, $\varphi(t)$, which consist of the superposition of $\Phi(t)$ pulses, as is shown in Fig. 1.5.

2. The error performance of GFSK digital modulation

Optimal detection of CPM signaling, where is included GFSK, can be achieved using the maximum likelihood sequence estimation (MLSE), which is implemented usually through a Viterbi processor. The MLSE detector observes the received signal over an infinite time interval and selects the infinite length sequence that minimizes the error probability. Since the observation of a signal over an infinite time interval is practically impossible, the suboptimal detector observes the received signal over N symbol intervals. The most likely sequence is chosen considering different metrics [Hassan-14], where the most employed metric is the Euclidean distance [Svensson-84]. Therefore, this metric determines the error performance in CPM modulation schemes [Rimoldi-91], [Anderson-86], and [Proakis-08].

2.1. Theoretical performance of GFSK

Considering the complex envelope of a binary GFSK signal encoded by a sequence of N symbols $\boldsymbol{\alpha} = \{\alpha_0, \alpha_1, \alpha_2, \ldots, \alpha_{N-1}\}$:

$$s(t, \boldsymbol{\alpha}) = \sqrt{\frac{E_s}{T}} \exp\left(j\varphi(t, \boldsymbol{\alpha})\right) \tag{2-1}$$

where E_s is the energy of a symbol during an interval of length T and regarding Fig. 1.2c, the phase signal is described as:

$$\varphi(t, \boldsymbol{\alpha}) = \sum_{i=0}^{k} \alpha_i \Phi(t - iT) \quad kT \le t < (k+1)T \tag{2-2}$$

with $\alpha_i \in \{+1, -1\}$. The sequence error probability is defined as the probability of detecting a sequence $\boldsymbol{\alpha}^j$ when the sequence $\boldsymbol{\alpha}^i$, with $j \neq i$, was transmitted. This can be described precisely by defining the following events: let the event of transmitting a sequence $\boldsymbol{\alpha}^i$ be represented as E_T^i and the event of detecting a sequence $\boldsymbol{\alpha}^j$ at the receiver be represented as E_R^j. Therefore, an error is defined as the event $E_T^i \cap E_R^j$ with $j \neq i$, and the error probability is the probability of the union

of all possible error events:

$$P_e = P\left(\bigcup_{i=1}^{M}\bigcup_{j\neq i} E_T^i \cap E_R^j\right) \leq \sum_{i=1}^{M}\sum_{j\neq i} P\left(E_T^i \cap E_R^j\right) \tag{2-3}$$

where the inequality in the preceding relation follows from the well-known Boole's union inequality and $M = 2^N$ is the number of different symbol sequences. Furthermore, by using the definition of conditional probability, $P\left(E_R^j \mid E_T^i\right)$ is the probability that the sequence $\boldsymbol{\alpha}^j$ was detected assuming that the sequence $\boldsymbol{\alpha}^i$ was transmitted. Hereafter, (2-3) can be expressed as:

$$P_e \leq \sum_{i=1}^{M}\sum_{j\neq i} P\left(E_R^j \mid E_T^i\right) P\left(E_T^i\right) \tag{2-4}$$

Assuming that all M sequences have the same probability of being transmitted, then $P(E_T^i) = 1/M$, $\forall \;\; i = 1,2,\ldots,M$. Consequently, (2-4) becomes:

$$P_e \leq \frac{1}{M}\sum_{i=1}^{M}\sum_{j\neq i} P\left(E_R^j \mid E_T^i\right) \tag{2-5}$$

To compute (2-5), note that the term $P\left(E_R^j \mid E_T^i\right)$ is determined by the MLSE detection process, which finds the maximum-likelihood sequence for the received signal $s\left(t,\boldsymbol{\alpha}^i\right)$ based on the Euclidean distance metric criterion. The signals $s\left(t,\boldsymbol{\alpha}^j\right) \;\; \forall \;\; j = 1,2,\ldots,M$ belong to a signal space where the distance is measured in terms of the Euclidean distance operator $\Delta\left\{s\left(t,\boldsymbol{\alpha}^i\right), s\left(t,\boldsymbol{\alpha}^j\right)\right\}$, defined as:

$$\Delta\left\{s\left(t,\boldsymbol{\alpha}^i\right), s\left(t,\boldsymbol{\alpha}^j\right)\right\} = \Delta^{ij} = \sqrt{\int_0^{NT} \left\|s(t,\boldsymbol{\alpha}^i) - s(t,\boldsymbol{\alpha}^j)\right\|^2 dt} \tag{2-6}$$

with $\|\bullet\|$ denoting the norm of a vector. The Euclidean distance Δ^{ij} between two pair of signals can be expressed in terms of the difference of the encoding sequences $\boldsymbol{\gamma}^{ij} = \boldsymbol{\alpha}^i - \boldsymbol{\alpha}^j$ [Aulin-81a]:

$$\begin{aligned}\left(\Delta^{ij}\right)^2 &= \int_0^{NT}\left[s(t,\boldsymbol{\alpha}^i)-s(t,\boldsymbol{\alpha}^j)\right]\left[s(t,\boldsymbol{\alpha}^i)-s(t,\boldsymbol{\alpha}^j)\right]^* dt \\ &= \int_0^{NT}\left[s(t,\boldsymbol{\alpha}^i)-s(t,\boldsymbol{\alpha}^j)\right]\left[s(t,\boldsymbol{\alpha}^i)^*-s(t,\boldsymbol{\alpha}^j)^*\right]dt \\ &= \int_0^{NT}\left\|s(t,\boldsymbol{\alpha}^i)\right\|^2+\left\|s(t,\boldsymbol{\alpha}^j)\right\|^2-s(t,\boldsymbol{\alpha}^i)\left[s(t,\boldsymbol{\alpha}^j)\right]^*-s(t,\boldsymbol{\alpha}^j)\left[s(t,\boldsymbol{\alpha}^i)\right]^* dt \\ &= 2NE_s-\frac{E_s}{T}\int_0^{NT}\exp\left(j\left(\varphi(t,\boldsymbol{\alpha}^i)-\varphi(t,\boldsymbol{\alpha}^j)\right)\right)+\exp\left(j\left(\varphi(t,\boldsymbol{\alpha}^j)-\varphi(t,\boldsymbol{\alpha}^i)\right)\right)dt \\ &= 2NE_s-\frac{2E_s}{T}\int_0^{NT}\cos\left(\varphi\left(t,\boldsymbol{\alpha}^i\right)-\varphi\left(t,\boldsymbol{\alpha}^j\right)\right)dt\end{aligned} \tag{2-7}$$

where $[\bullet]^*$ stands for the complex conjugate. Considering $\boldsymbol{\alpha}=\{\alpha_0,\alpha_1,\alpha_2,\ldots,\alpha_{N-1}\}$ and defining $\boldsymbol{\Phi}(t)=\left(\Phi(t),\Phi(t-T),\ldots,\Phi\left(t-(N-1)T\right)\right)$, (2-2) can be written as

$$\varphi(t,\boldsymbol{\alpha})=\boldsymbol{\alpha}\boldsymbol{\Phi}'(t)\quad kT\le t<(k+1)T$$

with $\bullet'$ denoting the transpose operator. Then, (2-7) can be expressed as follows

$$\begin{aligned}\left(\Delta^{ij}\right)^2 &= 2E_s\left(N-\frac{1}{T}\int_0^{NT}\cos\left(\boldsymbol{\alpha}^i\boldsymbol{\Phi}'(t)-\boldsymbol{\alpha}^j\boldsymbol{\Phi}'(t)\right)dt\right) \\ &= 2E_s\left(N-\frac{1}{T}\int_0^{NT}\cos\left(\left(\boldsymbol{\alpha}^i-\boldsymbol{\alpha}^j\right)\boldsymbol{\Phi}'(t)\right)dt\right) \\ &= 2E_s\left(N-\frac{1}{T}\int_0^{NT}\cos\left(\varphi\left(t,\boldsymbol{\alpha}^i-\boldsymbol{\alpha}^j\right)\right)dt\right) \\ &= 2E_s\left(N-\frac{1}{T}\int_0^{NT}\cos\left(\varphi\left(t,\gamma^{ij}\right)\right)dt\right)\end{aligned} \tag{2-8}$$

Given that $s\left(t,\boldsymbol{\alpha}^j\right)$ was transmitted, then $r(t)=s\left(t,\boldsymbol{\alpha}^j\right)+\eta(t)$, where $\eta(t)$ represents the Gaussian noise, is detected as $s\left(t,\boldsymbol{\alpha}^i\right)$ when is accomplished the following relation of Euclidean distance

$$\Delta\left\{r(t),s\left(t,\boldsymbol{\alpha}^i\right)\right\}\le\Delta\left\{r(t),s\left(t,\boldsymbol{\alpha}^j\right)\right\} \tag{2-9}$$

Consequently, an error occurs in the detection process. Therefore,

$$P\left(E_R^j\mid E_T^i\right)=P\left(\Delta\left\{r(t),s\left(t,\boldsymbol{\alpha}^i\right)\right\}\le\Delta\left\{r(t),s\left(t,\boldsymbol{\alpha}^j\right)\right\}\right) \tag{2-10}$$

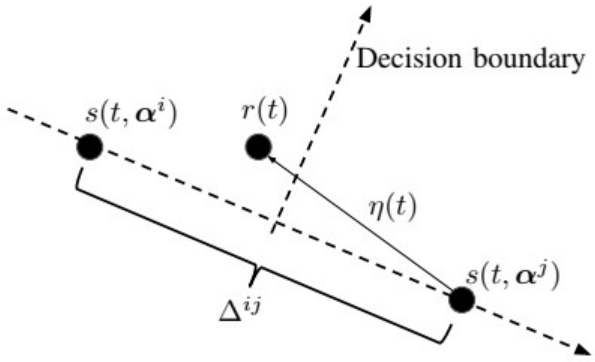

Fig. 2.1 Signal space representation of the received signal $r(t)$ in AWGN channel and the decision boundary between $s(t,\boldsymbol{\alpha}^i)$ and $s(t,\boldsymbol{\alpha}^j)$.

can be expressed in terms of the noise power in the following way. Taking as a reference Fig. 2.1 and choosing a coordinate system in the signal space with one axis placed from $s(t,\boldsymbol{\alpha}^i)$ to $s(t,\boldsymbol{\alpha}^j)$. Then, condition (2-9) is equivalent to saying that the component of $\eta(t)$ along that axis is bigger than the distance $\Delta^{ij}/2$. Therefore,

$$P\left(E_R^j \mid E_T^i\right) = \int_{\Delta^{ij}/2}^{\infty} \frac{1}{\sqrt{\pi N_0}} exp\left(\frac{\eta^2}{N_0}\right) d\eta = Q\left(\frac{\Delta^{ij}}{\sqrt{2N_0}}\right) \tag{2-11}$$

Hence, (2-5) is expressed as:

$$P_e \le \frac{1}{M} \sum_{i=1}^{M} \sum_{j \ne i} Q\left(\frac{\Delta^{ij}}{\sqrt{2N_0}}\right) \tag{2-12}$$

In order to obtain a tight upper bound for P_e, it is necessary to obtain the Δ^{ij} with the least distance, i.e.,

$$\Delta_{\min} = \min_{\substack{i,j \\ i \ne j}} \Delta^{ij}. \tag{2-13}$$

since the $Q(\bullet)$ function is a monotonically decreasing function. Furthermore, K pairs of signals comply with $\Delta_{\min}$, and each pair is counted twice in the double sum of (2-12). Thus, the tight upper bound for P_e in (2-12) is expressed as

$$P_e \leq \frac{2K}{M} Q\left(\frac{\Delta_{\min}}{\sqrt{2N_0}}\right) \tag{2-14}$$

Moreover, by defining $d_{\min} = \frac{\Delta_{\min}}{\sqrt{2E_s}}$, (2-14) can be written as

$$P_e \leq \frac{2K}{M} Q\left(d_{\min}\sqrt{\frac{E_s}{N_0}}\right) \tag{2-15}$$

where $d_{\min}^2$ denotes the minimum squared Euclidean distance (MSED) and determines the upper bound for P_e. A more detailed and complete explanation of the error probability in CPM communication systems is given in [Svensson-84], [Anderson-86], [Aulin-81a] and [Safak-17].

2.2. Euclidean metric performance for GFSK

Due to CPM signaling is entirely defined by the phase of the signal, the MSED depends on all phase trajectories of the signal over N symbol time intervals, as was described in (2-8). An important tool employed to find the MSED is the phase tree, which is a set of all possible phase trajectories of the signal, as is shown in Fig. 2.2a for a binary CPM signal with a rectangular pulse shape and pulse length $L = 1$, 1REC. It can be noted that as N increases, the number of phase trajectories grows exponentially. Taking as reference Fig. 2.2a, in which $N = 10$ symbols are considered, the number of phase trajectories is $M = 2^{10} = 1024$. According to (2-12), the computation of the error probability, for the case of $N = 10$, requires calculating the Euclidean distance $M^2 - M = 1{,}047{,}552$ times. Thus, this process becomes practically unrealizable. However, using (2-15), an upper bound for P_e can be found considering only the phase trajectories with the MSED.

From the phase tree shown in Fig. 2.2a, it is determined that the number of phase trajectories pairs with the MSED is 1024. Each pair of these phase trajectories has the characteristic that in the first symbol interval, they separate and, at the end of the second interval and hereafter, they join, as is shown in Fig. 2.2b for a particular pair of phase trajectories. Then, it can be assumed that a pair of phase trajectories (modulo 2π) that merge as soon as possible in a

specific time t_m and hereafter must be considered to determine the upper bound for P_e.

It is said that two sequences merge at a time t_m if they coincide for all $t \geq t_m$. Hence, considering that all symbols before $t = 0$ are known, the pair of sequences $\{+1-1, \alpha_2, \alpha_3, \ldots\}$ and $\{-1, +1, \alpha_2, \alpha_3, \ldots\}$ can be used in (2-7) to obtain the upper bound for P_e. By definition, the first symbol in both sequences must be different. Since the difference phase trajectory, $\varphi\left(t, \boldsymbol{\gamma}^{ij}\right)$, is zero after $t = 2T$, as is shown in Fig. 2.2c, there is no contribution to the MSED beyond this time. Furthermore, according to (2-7), the difference phase trajectory, $\varphi\left(t, \boldsymbol{\gamma}^{ij}\right)$, can be employed to determine the MSED.

The phase tree for CPM signaling with rectangular and Gaussian pulse shape with $L = 3$, 3REC and 3GAUSS, are shown in Fig. 2.3a, and Fig. 2.4a, respectively. As in the previous case, an upper bound for P_e can be found by considering pairs of input symbol sequences whose phase trajectories merge as soon as possible, as is shown in Fig. 2.3b, and Fig. 2.4b. Although the two input sequences considered are the same as in the case of 1REC, the merge point is at $t_m = 4T$. In general, the first merge point appears at $t_m = (L+1)T$. The difference phase trajectories for 3REC and 3GAUSS are also depicted in Fig. 2.3c, and Fig. 2.4c, respectively. It is important to mention that merge points could appear at $t_m = (L+2)T$, but the resulting Euclidean distance between that phase trajectories is more larger than those with merger points at $t_m = (L+1)T$. Then, these trajectories are not useful for obtaining an upper bound for P_e.

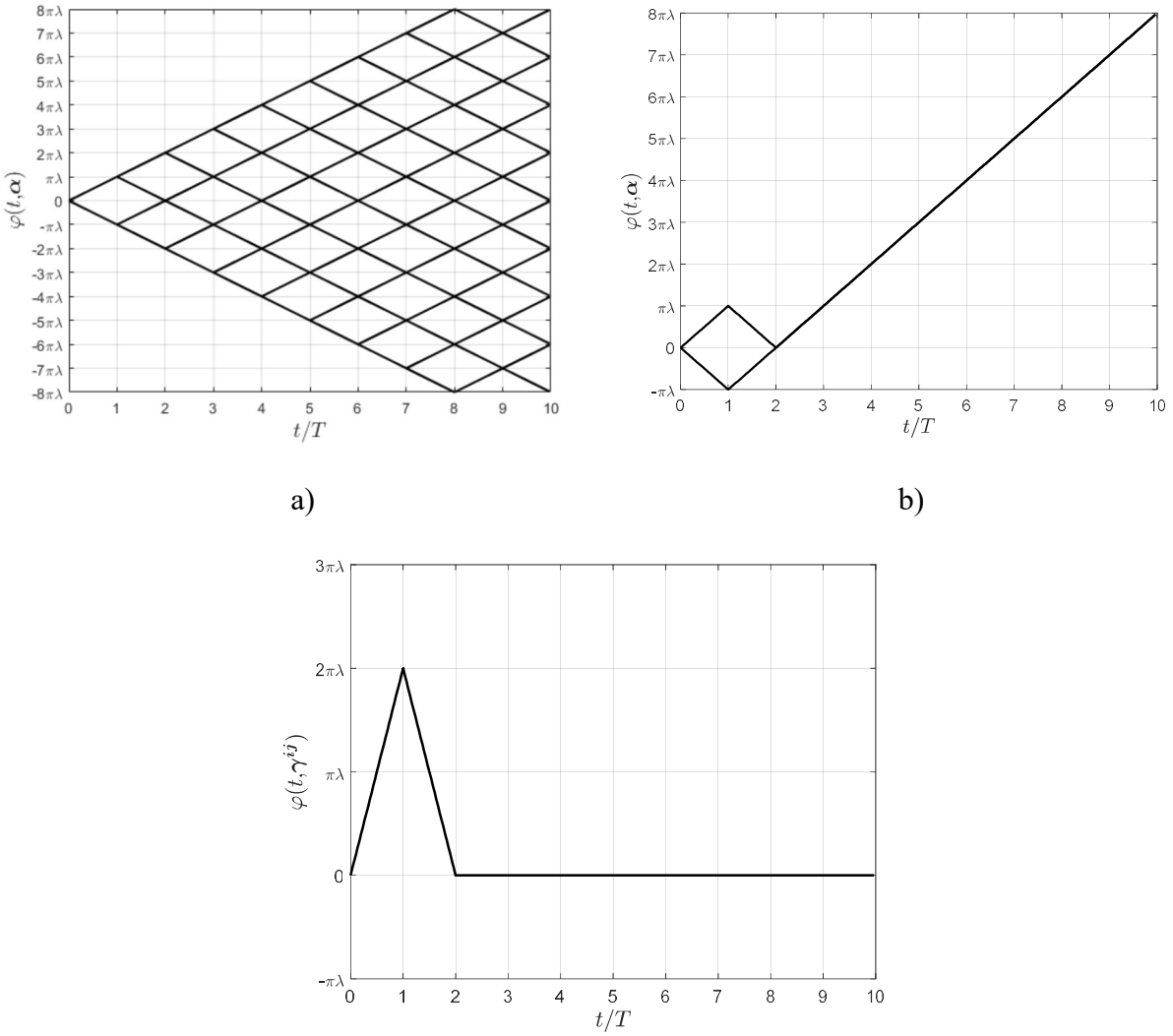

Fig. 2.2 Phase tree for a binary CPM signal with rectangular pulse shape and $L=1$ considering a) all the phase trajectories, b) two phase trajectories generated by the input sequences $\{+1,-1,\alpha_2,\alpha_3,\ldots\}$ and $\{-1,+1,\alpha_2,\alpha_3,\ldots\}$. c) The difference phase trajectory, $\varphi\left(t,\boldsymbol{\gamma}^{ij}\right)$.

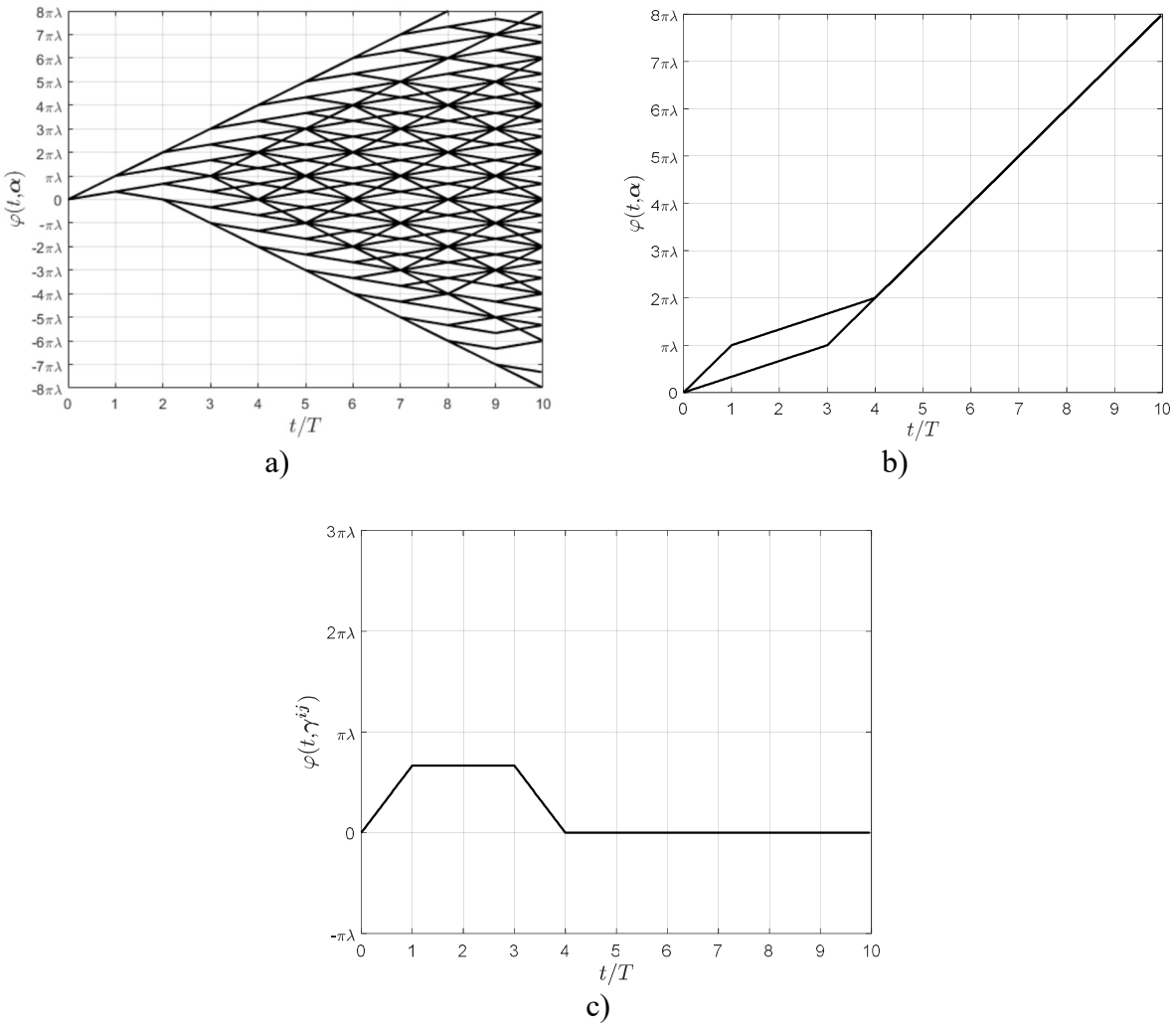

Fig. 2.3 Phase tree for a binary CPM signal with rectangular pulse shape, $L=3$, considering a) all the phase trajectories, b) two phase trajectories generated by the input sequences $\{+1,-1,\alpha_2,\alpha_3,\ldots\}$ and $\{-1,+1,\alpha_2,\alpha_3,\ldots\}$. c) The difference phase trajectory, $\varphi\left(t,\boldsymbol{\gamma}^{ij}\right)$,

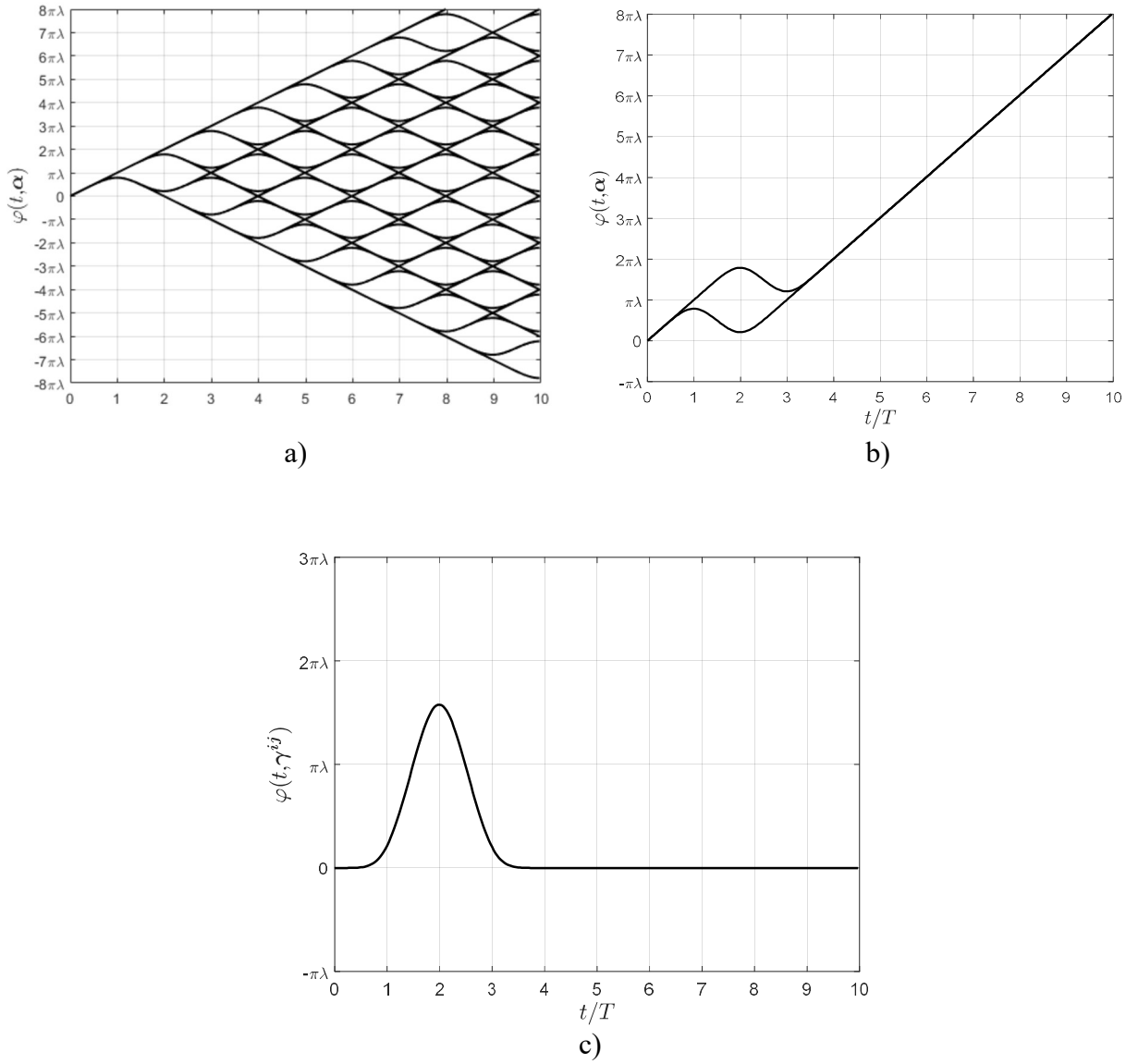

Fig. 2.4 Phase tree for a binary CPM signal with Gaussian pulse shape, $L=3$, considering a) all the phase trajectories, b) two phase trajectories generated by the input sequences $\{+1,-1,\alpha_2,\alpha_3,\ldots\}$ and $\{-1,+1,\alpha_2,\alpha_3,\ldots\}$. c) The difference phase trajectory, $\varphi\left(t,\boldsymbol{\gamma}^{ij}\right)$,

From (1-11) and (1-12), it can be noted that the phase signal depends on the modulation index. Thus, the MSED can vary according to this parameter, as is illustrated in Fig. 2.5. In this

TABLE 2.1. MSED, d_{min}^2, FOR DIFERENT CPM SIGNALING

CPM signaling	d_{min}^2
1REC	2
3REC	1.36
3GAUSS	2

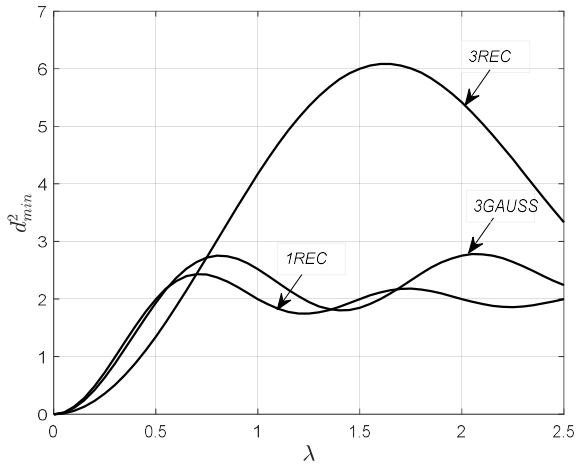

Fig. 2.5 A comparison of the minimum squared Euclidean distance, $d^2_{\min}$, versus the modulation index, λ, between 1REC, 3REC and 3GAUSS CPM signaling.

case, the 3REC CPM signaling exhibits the highest minimum Euclidean at a modulation index greater than 0.75. However, for a modulation index smaller than this value, the 1REC and 3GAUSS show the highest MSED.

The error performance for 1REC, 3REC, and 3GAUSS signaling is determined using the MSED values presented in Table 2.1 for $\lambda = 0.5$. Since only two input symbol sequences are considered ($M = 2$) and the same pair ($K = 1$) meets the minimum squared Euclidean distance, the theoretical error performance described in (2-15) can be written as

$$P_e \leq Q\left(\sqrt{\frac{d^2_{\min} E_s}{N_0}}\right) \tag{2-16}$$

The simulated and theoretical error performance, in terms of BER, for the three different CPM signaling is presented in Fig. 2.6.

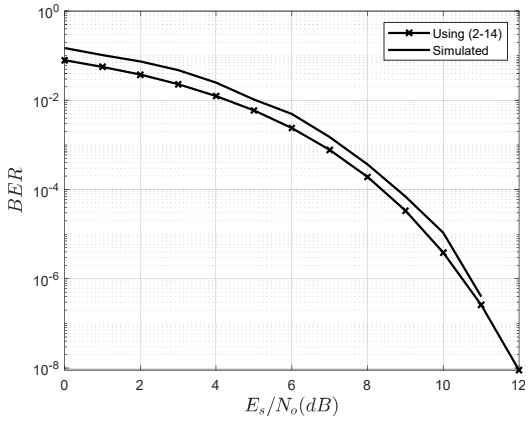

a)

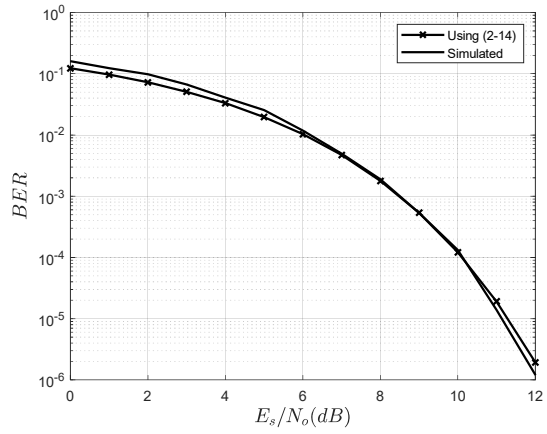

b)

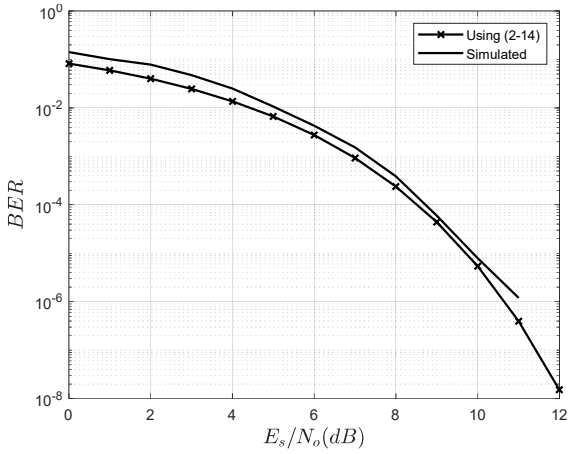

c)

Fig. 2.6 Error performance in terms of bit error rate (BER) for a) 1REC b) 3REC and c) 3GAUSS signaling.

2.3. Conclusions

In this Chapter, the error probability for different GFSK signaling has been analyzed. It is demonstrated that the Euclidean distance is the parameter that determines the error performance. When the Euclidean distance is computed, all the possible phase trajectories of the CPM signal, over a specific time interval, must be considered. Thus, this process becomes unrealizable. However, an upper bound of the error performance can be obtained if pairs of phase trajectories with the MSED are contemplated.

3. Linear Representation of GFSK signals

CPM schemes have high efficiency in power and radio spectrum usage, as well as a constant envelope that allows the use of power amplification with high efficiency. Despite those advantages, CPM schemes are nonlinear systems with a high complexity implementation for both modulators and demodulators. A reduction in the complexity implementation can be achieved by representing the nonlinear modulated signal as a sum of time-limited amplitude modulated pulses [Laurent-86]. This representation is called Laurent decomposition (LD). The importance of LD is evident in different researches that are mainly focused on reducing complexity implementation of communications systems using this approach [Kaleh-89], [Al-Dhahir-98], [Huang-03], [Noha-05]. An interesting alternative to the LD is proposed in [Liang-97], in which a linear approximation of the modulated signal is obtained by sampling the exact CPM signal.

3.1. The Laurent representation of GFSK signals

Considering the exact GFSK signal described in (2-1) and that the modulator takes N symbols, the GFSK signal can be expressed as the product of complex exponentials [Laurent-86]:

$$s(t,\boldsymbol{\alpha}) = \exp\left(j\pi\lambda \sum_{n=0}^{(N-1)-L} \alpha_n\right) \cdot \exp\left(j \sum_{n=(N-1)-L+1}^{N-1} \alpha_n \cdot \Phi(t-nT)\right) \tag{3-1}$$

The first term on the right-hand side of (3-1) represents the cumulative phase up to the symbol $\alpha_{(N-1)-L}$, and the second one is the phase from symbol $\alpha_{(N-1)-L+1}$ up to α_{N-1}. An equivalent form of expression (3-1) can be written as

$$s(t,\boldsymbol{\alpha}) = \exp\left(j\pi\lambda \sum_{n=0}^{(N-1)-L} \alpha_n\right) \cdot \prod_{n=(N-1)-L+1}^{N-1} \exp\left(j \cdot \alpha_n \cdot \Phi(t-nT)\right) \tag{3-2}$$

To characterize the exact CPM signal as a linear superposition of $M_{LD} = 2^{L-1}$ amplitude modulated pulses (AMP), the second term of (3-2) is represented using the Euler´s formula:

$$\exp\left(j \cdot \alpha_n \cdot \Phi(t-nT)\right) = \cos\left(\alpha_n \cdot \Phi(t-nT)\right) + j\sin\left(\alpha_n \cdot \Phi(t-nT)\right) \tag{3-3}$$

Using $\sin(\kappa)$, with $\kappa = \pi\lambda$, and considering

$$\begin{aligned}\cos(\alpha_n\Phi(t-nT)) &= \cos(\Phi(t-nT))\\ \sin\left(\alpha_n\Phi(t-nT)\right) &= \alpha_n\sin\left(\Phi(t-nT)\right)\end{aligned} \tag{3-4}$$

expression (3-3) can be rewritten as

$$\begin{aligned}\exp\left(j\cdot\alpha_n\cdot\Phi(t-nT)\right) &= \frac{\sin\left(\kappa\right)\left[\cos\left(\Phi(t-nT)\right)+j\alpha_n\cdot\sin\left(\Phi(t-nT)\right)\right]}{\sin\left(\kappa\right)}\\ &= \frac{\sin\left(\kappa\right)\cos\left(\Phi(t-nT)\right)}{\sin\left(\kappa\right)}+\frac{j\alpha_n\cdot\sin\left(\kappa\right)\cdot\sin\left(\Phi(t-nT)\right)}{\sin\left(\kappa\right)}\end{aligned} \tag{3-5}$$

The term $\frac{\cos\left(\kappa\right)\sin\left(\Phi(t-nT)\right)}{\sin\left(\kappa\right)}$ is added and subtracted in (3-5) without modifying it

$$\begin{aligned}\exp\left(j\cdot\alpha_n\cdot\Phi(t-nT)\right) &= \frac{\sin\left(\kappa\right)\cos\left(\Phi(t-nT)\right)}{\sin\left(\kappa\right)}-\frac{\cos(\kappa)\sin\left(\Phi(t-nT)\right)}{\sin\left(\kappa\right)}\\ &+\frac{j\alpha_n\cdot\sin\left(\kappa\right)\cdot\sin\left(\Phi(t-nT)\right)}{\sin\left(\kappa\right)}+\frac{\cos(\kappa)\sin\left(\Phi(t-nT)\right)}{\sin\left(\kappa\right)}\end{aligned} \tag{3-6}$$

Considering the first and second term of (3-6) and the fact that $\sin(x)\cos(y)\pm\cos(x)\sin(y)=\sin(x\pm y)$, then (3-6) is rewritten as

$$\begin{aligned}\exp\left(j\cdot\alpha_n\cdot\Phi(t-nT)\right) &= \frac{\sin\left(\kappa-\Phi(t-nT)\right)}{\sin\left(\kappa\right)}+\frac{j\alpha_n\cdot\sin\left(\kappa\right)\cdot\sin\left(\Phi(t-nT)\right)}{\sin\left(\kappa\right)}\\ &+\frac{\cos(\kappa)\sin\left(\Phi(t-nT)\right)}{\sin\left(\kappa\right)}\end{aligned} \tag{3-7}$$

It can be noted that the second and third term of (3-7) have a common factor. Thus, (3-7) can be expressed as

$$\exp\left(j\cdot\alpha_n\cdot\Phi(t-nT)\right)=\frac{\sin\left(\kappa-\Phi(t-nT)\right)}{\sin\left(\kappa\right)}+\frac{\sin\left(\Phi(t-nT)\right)}{\sin\left(\kappa\right)}\left(\cos(\kappa)+j\alpha_n\cdot\sin\left(\kappa\right)\right) \tag{3-8}$$

Considering (3-4) and using the Euler´s formula, expression (3-8) is simplified as

$$\exp\left(j\cdot\alpha_n\cdot\Phi(t-nT)\right)=\frac{\sin\left(\kappa-\Phi(t-nT)\right)}{\sin\left(\kappa\right)}+\exp\left(j\alpha_n\cdot\kappa\right)\frac{\sin\left(\Phi(t-nT)\right)}{\sin\left(\kappa\right)} \tag{3-9}$$

It is important to note that (3-9) is valid only for non-integer values of the modulation index, λ, in other cases $\sin(\kappa)=0$. Finally, the exact CPM signal described in (3-2) can be written as

$$s(t,\boldsymbol{\alpha}) = \exp\left(j\pi\lambda \sum_{n=0}^{(N-1)-L} \alpha_n \right) \cdot \prod_{n=(N-1)-L+1}^{N-1} \left[\frac{\sin(\kappa - \Phi(t-nT))}{\sin(\kappa)} + \exp(j\alpha_n \cdot \kappa) \frac{\sin(\Phi(t-nT))}{\sin(\kappa)} \right] \tag{3-10}$$

By defining the following functions

$$\psi(t) = \begin{cases} \Phi(t) & t < LT \\ \kappa - \Phi(t-LT) & t \geq LT \end{cases} \tag{3-11}$$

$$S_n(t) = \frac{\sin(\psi(t+nT))}{\sin(\kappa)} \tag{3-12}$$

the signal described in (3-10) can be written as:

$$s(t,\boldsymbol{\alpha}) = \exp\left(j\pi\lambda \sum_{n=0}^{(N-1)-L} \alpha_n \right) \cdot \prod_{n=(N-1)-L+1}^{N-1} \left[S_{L-n}(t) + \exp(j\alpha_n \cdot \kappa) S_{-n}(t) \right] \tag{3-13}$$

where

$$S_{L-n}(t) = \frac{\sin[\psi(t+(L-n)T)]}{\sin(\kappa)} = \frac{\sin[\kappa - \Phi(t+(L-n)T - LT)]}{\sin(\kappa)} = \frac{\sin[\kappa - \Phi(t-nT)]}{\sin(\kappa)} \tag{3-14}$$

$$S_{-n}(t) = \frac{\sin[\psi(t-nT)]}{\sin(\kappa)} = \frac{\sin[\Phi(t-nT)]}{\sin(\kappa)} \tag{3-15}$$

In the case of a GFSK signal with $L=3$ and $N=1$, the right-hand side of (3-13) is expanding as

$$\begin{aligned} &\prod_{n=-2}^{0} \left[S_{L-n}(t) + \exp(j\alpha_n \cdot \kappa) S_{-n}(t) \right] = \\ &\left[S_5(t) + \exp(j\alpha_{-2} \cdot \kappa) S_2(t) \right] \\ &\cdot \left[S_4(t) + \exp(j\alpha_{-1} \cdot \kappa) S_1(t) \right] \cdot \left[S_3(t) + \exp(j\alpha_0 \cdot \kappa) S_0(t) \right] = \\ &S_3(t) S_4(t) S_5(t) + \exp(j\alpha_{-2} \cdot \kappa) \cdot S_2(t) S_3(t) S_4(t) + \\ &\exp(j\alpha_{-1} \cdot \kappa) \cdot S_1(t) S_3(t) S_5(t) + \exp \cdot (j\alpha_{-1} \cdot \alpha_{-2} \cdot \kappa) S_1(t) S_2(t) S_3(t) + \\ &\exp(j\alpha_0 \cdot \kappa) S_0(t) S_4(t) S_5(t) + \exp(j\alpha_0 \cdot \alpha_{-2} \cdot \kappa) \cdot S_0(t) S_2(t) S_4(t) + \\ &\exp(j\alpha_0 \cdot \alpha_{-1} \cdot \kappa) \cdot S_0(t) S_1(t) S_5(t) + \exp(j\alpha_0 \cdot \alpha_{-1} \cdot \alpha_{-2} \cdot \kappa) \cdot S_0(t) S_1(t) S_2(t) \end{aligned} \tag{3-16}$$

It can be seen that M_{LD} terms of (3-16) content the factor $S_o(t)$, whereas those that do not contain it are a time-shifted version of the terms with that factor. Then, each product of (3-16) with the factor $S_o(t)$ can be represented using the following expression:

$$\begin{aligned} C_K(t) &= S_0(t)\cdot\prod_{i=1}^{L-1} S_{i+L\cdot\beta_{K,i}}(t) \\ 0 \le t &\le T\cdot\min_{i=1,2,\cdots,L-1}\left[L\left(2-\beta_{K,i}\right)-i\right] \end{aligned} \tag{3-17}$$

where the parameter $\beta_{K,i}$ is obtained with the radix-2 (binary) representation of K:

$$\begin{aligned} K &= \sum_{i=1}^{L-1} 2^{i-1}\cdot\beta_{K,i} \quad (0 \le K \le M_{LD}-1) \\ \beta_{K,i} &\in \{0,1\} \end{aligned} \tag{3-18}$$

Then, the final expression for the linear approximation of the GFSK signal described in (2-1) is written as

$$s(t,\boldsymbol{\alpha}) \approx \sum_{n=0}^{N-1}\sum_{K=0}^{M_{LD}-1} J^{A_{K,n}} C_K(t-nT) \tag{3-19}$$

where $J = \exp(j\pi\lambda)$, and consists in a linear superposition of $M_{LD} = 2^{L-1}$ amplitude modulated pulses $C_K(t)$, each one with a duration of

$$\begin{array}{cc} C_0(t) & (L+1)T \\ C_1(t) & (L-1)T \\ C_2(t), C_3(t) & (L-2)T \\ C_4(t), C_5(t), C_6(t), C_7(t) & (L-3)T \\ \cdots\cdots & \\ C_{M/2}(t), \cdots\cdots, C_{M-1}(t) & T \end{array} \tag{3-20}$$

The coefficients of the K-th component, $C_K(t)$, are determined as follows:

$$A_{K,n} = \sum_{m=0}^{n} \alpha_n - \sum_{i=1}^{L-1} \alpha_{n-i}\cdot\beta_{K,i} \tag{3-21}$$

The pulses $C_0(t), C_1(t), C_2(t)$ and $C_3(t)$, for $L=3$ and $\lambda = 0.5$, are shown in Fig. 3.1. The pulse $C_0(t)$ is the pulse with the most energy, so it is named the "main pulse."

The linear approximation using LD, described in (3-19), is applied to represent a GFSK signal which meets the BLE standard requirements. The modulation process uses frames with $N = 10^6$ symbols at the input of the modulator, a modulation index of 0.5 and a Gaussian pulse with a duration of $L=3$ symbol periods. The demodulator uses the Viterbi algorithm with a traceback of 20 symbol periods. The BER was computed once 100 frames were processed or 10^3 errors were detected for each value of SNR. In order to verify the accuracy of the approximation, a different number of pulses $C_k(t)$, were used to represent the exact signal.

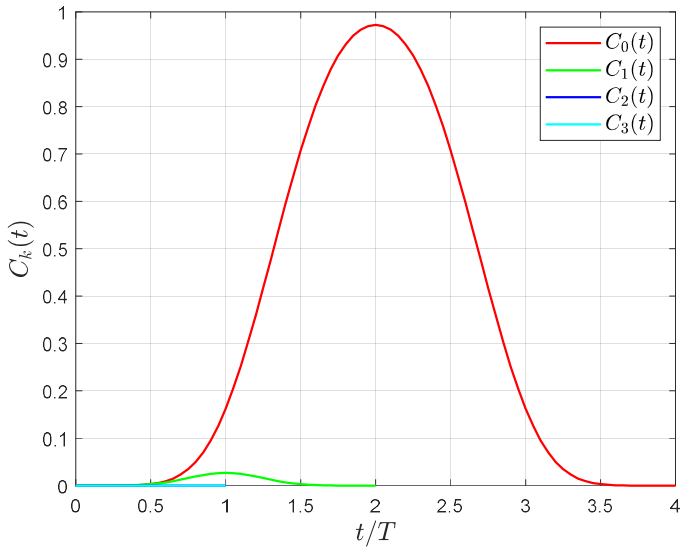

Fig. 3.1 Component pulses $C_0(t), C_1(t), C_2(t)$ and $C_3(t)$ of a linear GFSK signal with $L=3$ and $\lambda=0.5$.

Considering $L=3$, the number of components is $M_{LD}=2^{L-1}=2^2=4$, that corresponds to the pulses $C_0(t), C_1(t)$, $C_2(t)$, $C_3(t)$, each one with a duration of $4T$, $2T$, T and T symbol periods, respectively. Thus, from (3-19), the linear approximation is written as

$$s(t,\boldsymbol{\alpha}) \approx \sum_{n=0}^{N-1} \sum_{K=0}^{3} J^{A_{K,n}} \cdot C_K(t-nT) \tag{3-22}$$

Using (3-18) and considering $K=0$

$$0 = \sum_{i=1}^{2} 2^{i-1} \cdot \beta_{0,i} = 2^0 \cdot \beta_{0,1} + 2^1 \cdot \beta_{0,2} \tag{3-23}$$

then $\beta_{0,1}=0$ and $\beta_{0,2}=0$. Therefore, from (3-21)

$$\begin{aligned} A_{0,n} &= \sum_{m=0}^{n} \alpha_m \\ C_0(t) &= S_0(t) \cdot S_1(t) \cdot S_2(t) \end{aligned} \tag{3-24}$$

Now, for $K=1$

$$1 = \sum_{i=1}^{2} 2^{i-1} \cdot \beta_{1,i} = 2^0 \cdot \beta_{1,1} + 2^1 \cdot \beta_{1,2} \tag{3-25}$$

then $\beta_{1,1}=1$ and $\beta_{1,2}=0$, so

$$\begin{aligned} A_{1,n} &= \sum_{m=0}^{n}\alpha_m - \alpha_{n-1} = A_{0,n} - \alpha_{n-1} \\ C_1(t) &= S_0(t)\cdot S_4(t)\cdot S_2(t) \end{aligned} \tag{3-26}$$

With $K=2$

$$2 = \sum_{i=1}^{2} 2^{i-1}\cdot\beta_{2,i} = 2^0\cdot\beta_{2,1} + 2^1\cdot\beta_{2,2} \tag{3-27}$$

then $\beta_{2,1}=0$ and $\beta_{2,2}=1$, therefore

$$\begin{aligned} A_{2,n} &= \sum_{m=0}^{n}\alpha_n - \alpha_{n-2} = A_{0,n} - \alpha_{n-2} \\ C_0(t) &= S_0(t)\cdot S_1(t)\cdot S_5(t) \end{aligned} \tag{3-28}$$

Finally, with $K=3$

$$3 = \sum_{i=1}^{2} 2^{i-1}\cdot\beta_{3,i} = 2^0\cdot\beta_{3,1} + 2^1\cdot\beta_{3,2} \tag{3-29}$$

then $\beta_{3,1}=1$ and $\beta_{3,2}=1$, thus

$$\begin{aligned} A_{3,n} &= \sum_{m=0}^{n}\alpha_m - \alpha_{n-1} - \alpha_{n-2} = A_{0,n} - \alpha_{n-1} - \alpha_{n-2} \\ C_0(t) &= S_0(t)\cdot S_4(t)\cdot S_5(t) \end{aligned} \tag{3-30}$$

Using (3-22) and the above coefficients, the CPM signal is approximated as

$$\begin{aligned} s(t,\boldsymbol{\alpha}) \approx \sum_{n=0}^{N-1}\Bigg\{ &\exp\left(j\pi\lambda\sum_{m=0}^{n}\alpha_m\right)\cdot\Big[C_0(t-nT) + \exp(-\alpha_{n-1})C_1(t-nT) + \exp(-\alpha_{n-2})C_2(t-nT) \\ &+ \exp(-\alpha_{n-1}-\alpha_{n-2})C_3(t-nT)\Big]\Bigg\} \end{aligned} \tag{3-31}$$

The exact GFSK signal and its Laurent approximation (LA), using the pulses $C_0(t)$, $C_1(t)$, $C_2(t)$ and $C_3(t)$ (for $L=3$ and $\lambda=0.5$) are shown in Fig. 3.2. The power spectral density (PSD) of both signals and the performance, in terms of bit error rate (BER), is shown in Fig. 3.3 and Fig. 3.4, respectively. It can be noted that the BER and PSD for the exact GFSK signal and its LA are practically the same. Examples of LA for CPM signals with different characteristics are also given in [Wiesler-98] and [Wardle-05].

The main benefit of LA consists of the fact that a binary CPM signal can be expressed as

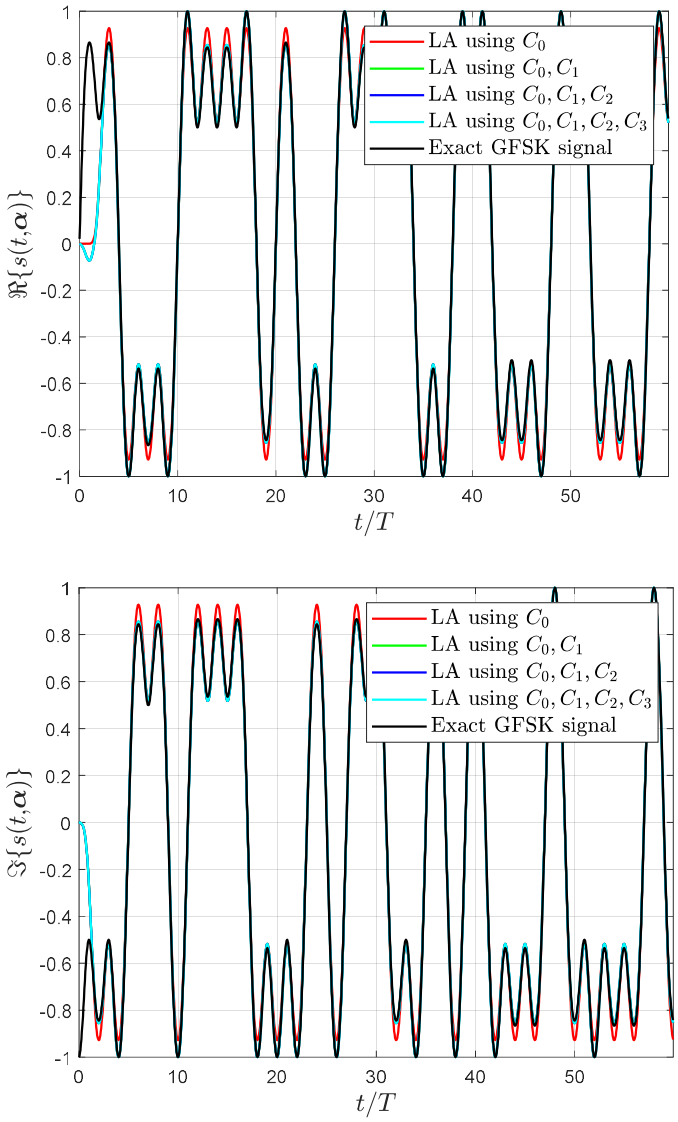

Fig. 3.2 The real and imaginary part of the exact GFSK signal (with $L=3$ and modulation index $\lambda=0.5$) and its approximation using LD using the component pulses $C_0(t), C_1(t)$, $C_2(t)$ and $C_3(t)$.

a linear superposition of pulses. It results in the implementation of receivers with low complexity, as is shown in [Kaleh-89].

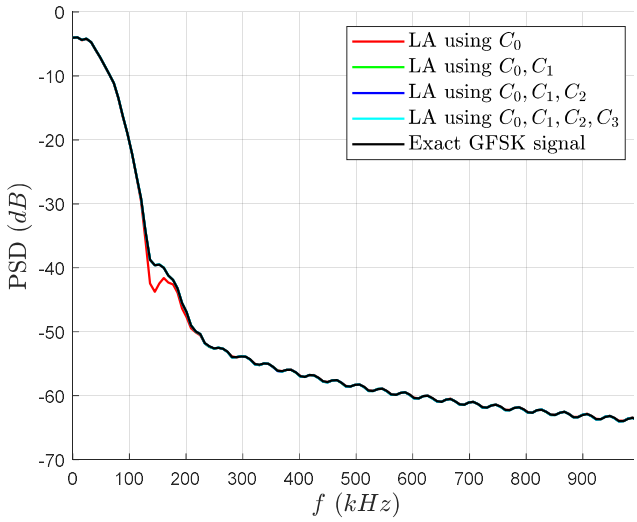

Fig. 3.3 Power spectral density (PSD) of the exact GFSK signal and its Laurent's linear approximation using $C_0(t), C_1(t), C_2(t)$ and pulses.

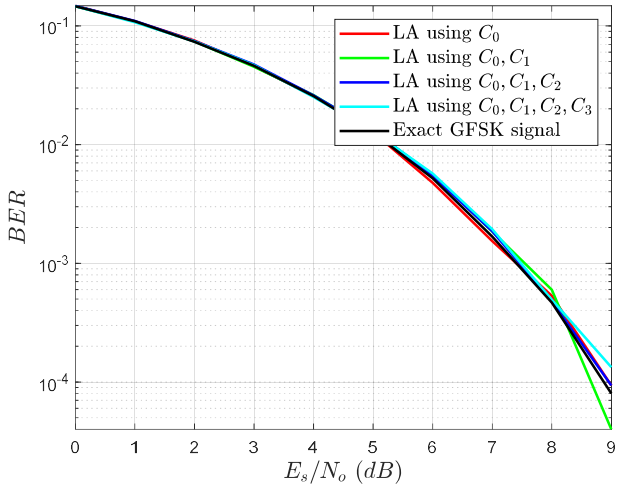

Fig. 3.4 Performance of the GFSK system considering the exact signal (with $L=3$ and modulation index $\lambda=0.5$) and the linear approximation using $C_0(t)$, $C_1(t)$, $C_2(t)$ and $C_3(t)$ pulses at the transmitter. The detector uses the Viterbi algorithm.

3.2. The Liang-Paulraj linear approximation of GFSK.

In order to obtain a linear approximation of the exact GFSK signal described in (2-1), and referring to Fig. 1.2c, the linearization process described in [Liang-97] is applied to the exact GFSK signal as follows. Considering two consecutive samples per symbol period of $s(t)$ and a time deviation T_d in the range $\left[0, \frac{T}{2}\right]$, the sampled signal is described as

$$x(kT + T_d) = \exp\left(j \sum_n \alpha_n \Phi((k-n)T + T_d)\right) \tag{3-32}$$

$$x\left(kT + T_d + \tfrac{T}{2}\right) = \exp\left(j \sum_n \alpha_n \Phi((k-n)T + T_d + \tfrac{T}{2})\right) \tag{3-33}$$

where $k \in \mathrm{Z}$ and T is the symbol-time duration. In Fig. 3.5 is shown the pulse decomposition, $\Phi(t)$, of the phase signal, $\varphi(t)$, and the respective samples used to obtain the linear approximation of $s(t)$. It is important to note that the pulses $\Phi(t)$ have a value of zero at $n > k+1$ and $\frac{\pi}{2}$ for $n < k$.

Defining four samples of the phase signal as $\phi_0 = \Phi(-T + T_d)$, $\phi_1 = \Phi\left(-\frac{T}{2} + T_d\right)$ $\phi_2 = \Phi(T_d)$ and $\phi_3 = \Phi\left(\frac{T}{2} + T_d\right)$, the signal described in (3-32) can be rewritten as

$$x(kT + T_d) = \exp\left[j\alpha_{k+1}\phi_0 + j\alpha_k\phi_2 + j\tfrac{\pi}{2}(\alpha_{k-1} + \alpha_{k-2} + ... + \alpha_0)\right] \tag{3-34}$$

$$x(kT + T_d) = \exp\left(j\alpha_{k+1}\phi_0\right) \cdot \exp\left(j\alpha_k\phi_2\right) \cdot \exp\left(j\tfrac{\pi}{2}\alpha_{k-1}\right) \cdot \exp\left(j\tfrac{\pi}{2}\alpha_{k-2}\right) \cdot ... \cdot \exp\left(j\tfrac{\pi}{2}\alpha_0\right). \tag{3-35}$$

Also, considering that $\alpha_n \in \{-1, +1\}$, $\cos(\alpha_n x) = \cos(x)$, $\sin(\alpha_n x) = \alpha_n \sin(x)$ and $\exp\left(j\alpha_n \tfrac{\pi}{2}\right) = \cos\left(\tfrac{\pi}{2}\right) + j\alpha_n \sin\left(\tfrac{\pi}{2}\right) = j\alpha_n$, the expression in (3-35) is rewritten as

$$x(kT + T_d) = \left[\cos(\alpha_{k+1}\phi_0) + j\sin(\alpha_{k+1}\phi_0)\right]\left[\cos(\alpha_k\phi_2) + j\sin(\alpha_k\phi_2)\right](j\alpha_{k-1})(j\alpha_{k-2})...(j\alpha_0) \tag{3-36}$$

$$x(kT + T_d) = \left[\cos(\alpha_{k+1}\phi_0) + j\sin(\alpha_{k+1}\phi_0)\right]\left[\cos(\alpha_k\phi_2) + j\sin(\alpha_k\phi_2)\right] \cdot j^k \cdot s_{k-1} \cdot \underbrace{s_{k-2} \cdot s_{k-2}}_{1} \cdot \underbrace{s_{k-3} \cdot ... \cdot s_0}_{1} \tag{3-37}$$

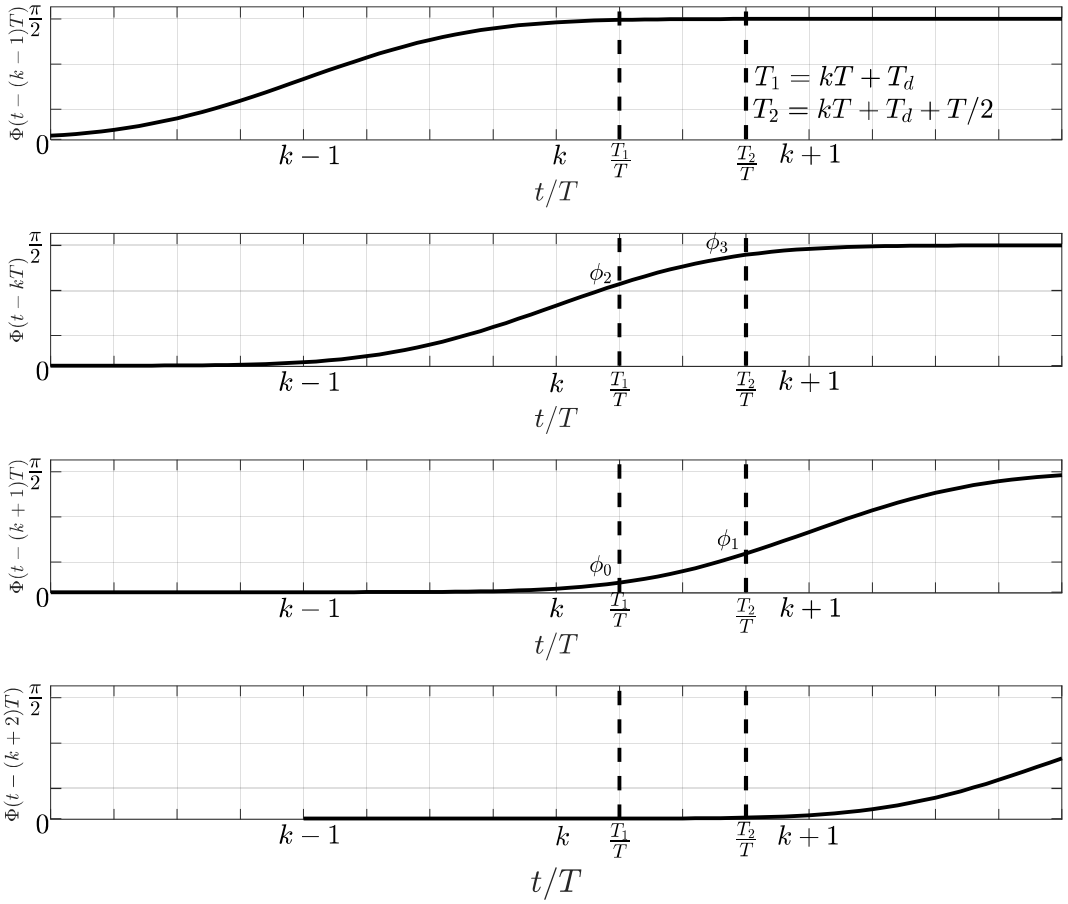

Fig. 3.5 Pulse decomposition, $\Phi(t)$, of the phase signal, $\varphi(t)$, and its respective samples, $\phi_0 ... \phi_3$, used to obtain the linear approximation of $s(t)$.

$$x(kT+T_d) = j^k s_{k-1}[\cos\phi_0\cos\phi_2 + js_k s_{k-1}\cos\phi_0\sin\phi_2 + js_{k+1}s_k\cos\phi_2\sin\phi_0 - s_k s_{k-1}s_{k+1}s_k\sin\phi_0\sin\phi_2] \tag{3-38}$$

$$x(kT+T_d) = j^k\left[s_{k-1}\cos\phi_0\cos\phi_2 + js_k\cos\phi_0\sin\phi_2 + js_{k+1}s_k s_{k-1}\cos\phi_2\sin\phi_0 - s_{k+1}\sin\phi_0\sin\phi_2\right] \tag{3-39}$$

In (3-39), the only nonlinear term is $s_{k+1}s_k s_{k-1}\cos\phi_2\sin\phi_0$. This term is smaller than the others by at least one order of magnitude; thus it can be ignored, and a linear approximation of $x(kT+T_d)$ is given by

$$\hat{x}(kT+T_d) = j^k\left[s_{k-1}\cos\phi_0\cos\phi_2 + js_k\cos\phi_0\sin\phi_2 - s_{k+1}\sin\phi_0\sin\phi_2\right] \tag{3-40}$$

The same process is valid for $x\left(kT+T_d+\frac{T}{2}\right)$. Thus, (3-33) can be rewritten as

$$x\left(kT+T_d+\tfrac{T}{2}\right)=\exp\left[j\alpha_{k+1}\phi_1+j\alpha_k\phi_3+j\tfrac{\pi}{2}\left(\alpha_{k-1}+\alpha_{k-2}+...+\alpha_0\right)\right] \tag{3-41}$$

$$x\left(kT+T_d+\tfrac{T}{2}\right)=\exp\left(j\alpha_{k+1}\phi_1\right)\cdot\exp\left(j\alpha_k\phi_3\right)\cdot\exp\left(j\tfrac{\pi}{2}\alpha_{k-1}\right)\cdot\exp\left(j\tfrac{\pi}{2}\alpha_{k-2}\right)\cdot....\cdot\exp\left(j\tfrac{\pi}{2}\alpha_0\right) \tag{3-42}$$

$$x\left(kT+T_d+\tfrac{T}{2}\right)=\left[\cos\left(\alpha_{k+1}\phi_1\right)+j\sin\left(\alpha_{k+1}\phi_1\right)\right]\left[\cos\left(\alpha_k\phi_3\right)+j\sin\left(\alpha_k\phi_3\right)\right]\left(j\alpha_{k-1}\right)\left(j\alpha_{k-2}\right)...\left(j\alpha_0\right) \tag{3-43}$$

$$\begin{aligned}x\left(kT+T_d+\tfrac{T}{2}\right)=&\left[\cos\left(\alpha_{k+1}\phi_1\right)+j\sin\left(\alpha_{k+1}\phi_1\right)\right]\left[\cos\left(\alpha_k\phi_3\right)+j\sin\left(\alpha_k\phi_3\right)\right]\\&\cdot j^k\cdot s_{k-1}\cdot\underbrace{s_{k-2}\cdot s_{k-2}}_{1}\cdot\underbrace{s_{k-3}\cdot....\cdot s_0}_{1}\end{aligned} \tag{3-44}$$

$$\begin{aligned}x\left(kT+T_d+\tfrac{T}{2}\right)=&j^k s_{k-1}\left[\cos\phi_1\cos\phi_3+js_ks_{k-1}\cos\phi_1\sin\phi_3+js_{k+1}s_k\cos\phi_3\sin\phi_1\right.\\&\left.-s_ks_{k-1}s_{k+1}s_k\sin\phi_1\sin\phi_3\right]\end{aligned} \tag{3-45}$$

$$\begin{aligned}x\left(kT+T_d+\tfrac{T}{2}\right)=&j^k\left[s_{k-1}\cos\phi_1\cos\phi_3+js_k\cos\phi_1\sin\phi_3+js_{k+1}s_ks_{k-1}\cos\phi_3\sin\phi_1\right.\\&\left.-s_{k+1}\sin\phi_1\sin\phi_3\right]\end{aligned} \tag{3-46}$$

The smallest and nonlinear term in (3-46) is $s_{k+1}s_ks_{k-1}\cos\phi_3\sin\phi_1$. Thus, it can be ignored and an estimate of $x\left(kT+T_d+\frac{T}{2}\right)$ is

$$\hat{x}\left(kT+T_d+\tfrac{T}{2}\right)=j^k\left[s_{k-1}\cos\phi_1\cos\phi_3+js_k\cos\phi_1\sin\phi_3-s_{k+1}\sin\phi_1\sin\phi_3\right] \tag{3-47}$$

Writing (3-40) and (3-47) in matrix form leads to

$$\begin{bmatrix}\hat{x}_k\\ \hat{x}_{k+\frac{1}{2}}\end{bmatrix}=j^k\mathbf{A}\begin{bmatrix}s_{k+1}\\ s_k\\ s_{k-1}\end{bmatrix} \tag{3-48}$$

where

$$\begin{aligned}\hat{x}_k&=\hat{x}(kT+T_d)\\ \hat{x}_{k+\frac{1}{2}}&=\hat{x}(kT+T_d+\tfrac{T}{2})\end{aligned} \tag{3-49}$$

and

$$\mathbf{A}=\begin{bmatrix}-\sin\phi_0\sin\phi_2 & j\cos\phi_0\sin\phi_2 & \cos\phi_0\cos\phi_2\\ -\sin\phi_1\sin\phi_3 & j\cos\phi_1\sin\phi_3 & \cos\phi_1\cos\phi_3\end{bmatrix} \tag{3-50}$$

The exact GFSK signal described in (2-1), its linear approximation defined in (3-48), and

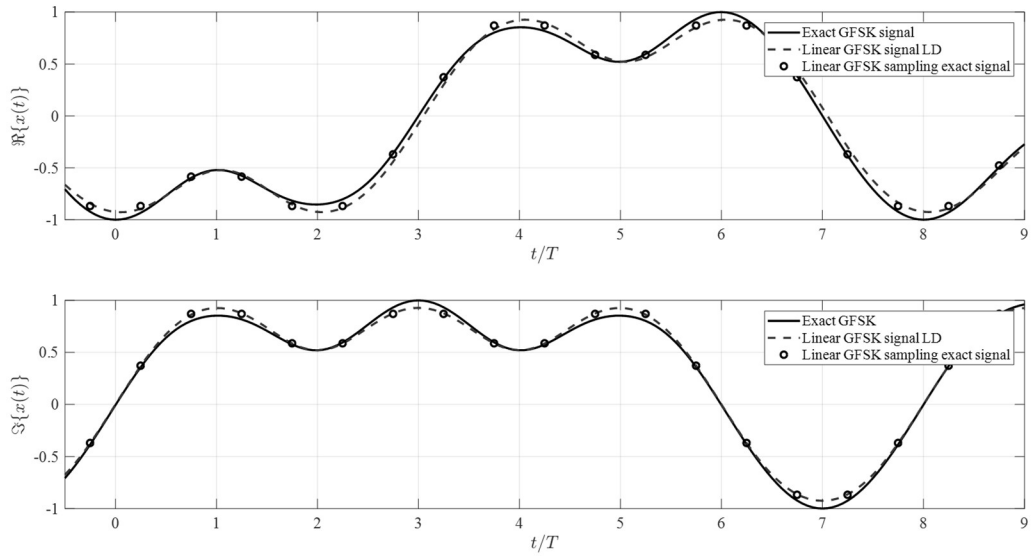

Fig. 3.7 The real and imaginary part of the exact GFSK signal and its linear approximations.

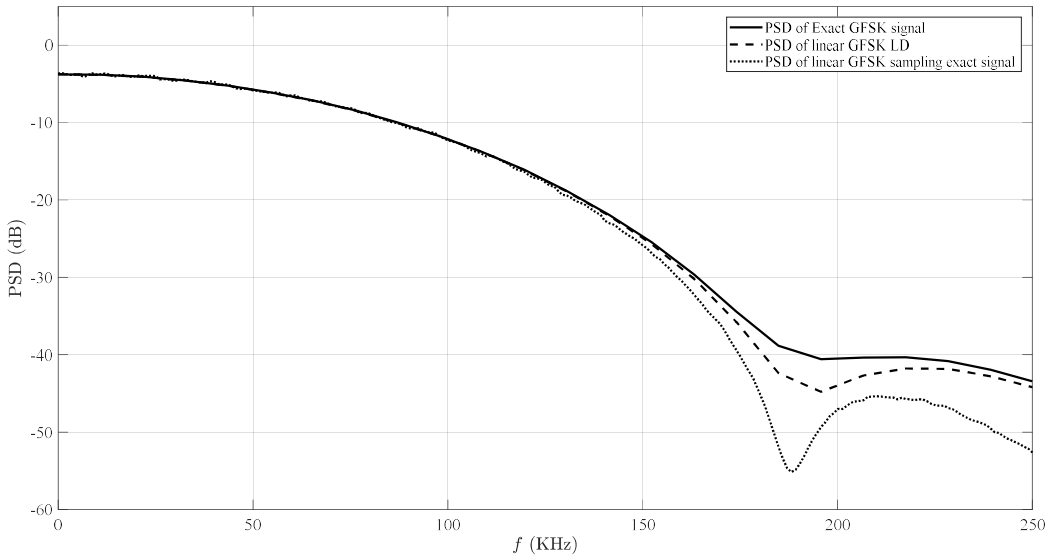

Fig. 3.6 Power spectral density (PSD) of the exact GFSK signal and its linear approximations.

the linear approximation using LD are shown in Fig. 3.7. It can be noted that they match quite well. The power spectral density (PSD) of each signal is shown in Fig. 3.6. It can be observed that the main lobe of the linear approximations is narrower than the main lobe of the exact GFSK signal due to the linearization process.

3.3. Conclusions

In this Chapter, is described in detail the Laurent decomposition which allows to obtain a linear approximation of the CPM signal by superposition of finite amplitude modulated pulses. Although there are some other techniques used for the same purpose, the decomposition of Laurent is widely used in the design of receivers with low complexity.

An essential aspect in Laurent's decomposition is the fact that one pulse concentrates most of the energy. Then, the CPM signal can be approximated from this pulse without altering the transmitted signal, increasing the spectrum, or modifying the performance.

A comparison between a CPM signal that meets Bluetooth low energy requirements, and its LA is presented. Results show excellent accuracy among the two signals, without performance losing or bandwidth increasing.

In addition, it is presented and described a linear approximation of a GFSK signal based on the sampling of the exact signal. The results show a perfect match between the exact signal and its linear approximation using this approach. The results confirm that this linearization process is an excellent alternative to the LD linearization method.

4. Low complexity GFSK detectors

Detectors that use the Viterbi algorithm are used to find the transmitted data sequence in CPM systems [Xiong-06]. A near-optimal detection and a pulse shape that extends over one symbol-time duration (partial-response CPM) are factors that increase the number of phase states in the VA [Proakis-08], [Yang-15]. Thus, the complexity of the demodulator can become highly prohibitive if a good performance or a better spectral efficiency are desired. So, the design of low-complexity CPM schemes with these characteristics is of great importance.

In order to reduce the complexity of the communication system implementation, two approaches are mainly considered: optimization of hardware resources and decomposition of the CPM signals into PAM (pulse amplitude modulation) waveforms.

4.1. Complexity reduction techniques based on optimization of hardware resources

Fully or partially analog modulators that use a frequency synthesizer to generate the CPM signal are found in [Riley-94], where a frequency synthesizer controls the instantaneous frequency and phase of the output signal. As a result, in-phase and quadrature mixer or digital to analog converters (DAC) are not required. In [Krishnapura-98] is described the design of an analog Gaussian pulse-shaping chip whose impulse response approximates quite well the impulse response of the filter used in the digital approach. The main advantage of the proposed analog filter is a reduction of power consumption and chip area compared with the digital implementation. Likewise, [Xia-03] proposes a very simple analog GMSK demodulator based on a zero-crossing detector, whose near-optimal performance, low power consumption, and a simple circuit implementation makes it feasible to be used in CPM systems.

Digital implementations of the modulator are proposed in [Aulin-81b] and [Anderson-86], which are the early ROM-based implementations for full and partial-response CPM systems. In addition, spectral analysis for these implementations shows that partial-response CPM systems have better spectral efficiency than the full-response systems. In [Linz-96] a reduction in memory size is achieved by taking advantage of the symmetrical properties of the shaping filter, and thus

typical processing steps such as modulating waveform ROM lookup, integration, and sine/cosine ROM lookup can be omitted. In [Rimoldi-88] is proposed the decomposition of the CPM system into a continuous phase encoder and a memory-less modulator, in which implementations of CPM signaling and decoding algorithms with a reduction in complexity can be achieved. Recently, in [Svedek-09] is proposed an efficient pulse-shaping implementation based on a 1-bit word length ROM and a sigma-delta digital converter so that 3-times less memory is needed and the use of a complex *n*-bit DAC is not necessary. Moreover, [Ramírez-Pérez-16] presents a reformulation of the CPM signal and proposes a highly reconfigurable architecture for a CPM transmitter that can be used in software radio systems. This architecture takes advantage of the strengths (high signal to quantization noise ratio and low hardware complexity) of ROM-based and integration-based approaches.

4.2. Complexity reduction techniques based on the decomposition of the GFSK signal into PAM waveforms

The second technique is oriented to reducing the complexity of the communication system is based on the representation of the CPM signals using PAM decomposition. Laurent shows in [Laurent-86] that any binary CPM signal can be decomposed into a finite number of PAM pulses. As a result, the signal can be reconstructed with reasonable accuracy by one main pulse, the computation of the power frequency spectrum of the CPM signal becomes simple, and low-complexity modulators and demodulators can be achieved. In [Jung-92] is presented a modulator based on the Laurent decomposition (LD), that allows the CPM signal to be generated in a single step, as opposed to the conventional CPM generation in which two steps (digital generation of the complex envelope and modulation of the carrier by the complex envelope) are required. In [Yang-11] is defined a pulse-shaping function (consisting of overlapping short-duration pulses) that gives to CPM signaling the separable phase property; as a result, the so-called separable phase CPM signaling has a similar or better bandwidth and power performance than the conventional one. In [Kaleh-89] is presented a reduced-complexity Viterbi receiver with a near-optimal performance and a reduced number of matched filters; also, it is given a design method for the optimum receiver filter. In [Taki-06] is proposed a GMSK system based on LD, in which Low-Density Parity Check (LDPC) codes are employed to improve the performance of the system. Furthermore, in [Nelson-

08] is developed a near-optimal detector based on PAM decomposition for CPM signals used in aeronautical telemetry.

Alternatives for complexity reduction of CPM signaling are also available. In [Mengali-95] is proposed a method that, in contrast to LD, decomposes multilevel CPM signals into a sum of PAM components. In [Cariolaro-10] are formulated several classes of decompositions for different purposes, each of which admits an infinite number of different decompositions of the same CPM signal; among this decomposition is LD. Also, a combination of CPM using LD and space-time block coding for multiple-input multiple-output (MIMO) systems is found in [Zhang-03] and [Xian-08]. CPM signaling approximations using Legendre polynomials (useful for signal sets that exhibit relatively large memory lengths and small modulation indices) and spline functions (suitable for a wide variety of pulse shapes, memory lengths, alphabets, and modulation indices) are proposed in [Brown-09].

4.3. A low complexity GFSK detector for IoT devices based on the pseudo-inverse estimation (LPIE-detector)

Based on the linear representation of the exact GFSK signal described in [Liang-97], a novel linear GFSK demodulator is described in this section. The main advantages of this proposal are low complexity, a near-optimal maximum likelihood detector performance in the AWGN channel, and the possibility of operating with different GFSK modulators with a nominal modulation index of 0.5, so it could be employed in BLE devices. This contribution was published in IET Communications Journal [Aldana-Lopez-18].

4.3.1 LPIE2s-detector system model

Considering the linear structure of the GFSK modulator described in (3-48) , and since one symbol-time duration of the modulated signal described contains information about three symbols, the proposed demodulator uses the linear structure to obtain an estimate of each one of these three transmitted symbols. Therefore, by taking a linear combination of these three estimates, one combined estimated symbol can be expressed as

$$\hat{s}_k = h_1\hat{s}_k^{(1)} + h_2\hat{s}_k^{(2)} + h_3\hat{s}_k^{(3)} = \sum_{m=1}^{3} h_m\hat{s}_k^{(m)} \tag{4-1}$$

where $h_m \in \Re$ and the superscript 1 refers to the estimate of s_k obtained from the previous symbol-time duration; likewise, superscripts 2 and 3 refer to the estimates of s_k obtained from the current and the subsequent symbol-time durations, respectively.

Taking two samples in a symbol time duration of the received signal, an estimate of the transmitted symbols can be obtained as follows

$$\begin{bmatrix} \hat{s}_{k+1}^{(1)} \\ \hat{s}_k^{(2)} \\ \hat{s}_{k-1}^{(3)} \end{bmatrix} = \left(j^k\mathbf{A}\right)^{\dagger}\begin{bmatrix} r_k \\ r_{k+\frac{1}{2}} \end{bmatrix} \tag{4-2}$$

where $(\cdot)^{\dagger}$ denotes the Moore-Penrose pseudo-inverse matrix, $r_k = r\left(kT + T_d\right)$ and $r_{k+\frac{1}{2}} = r\left(kT + \frac{T}{2} + T_d\right)$ are two consecutive samples of the received signal described by

$$r(t) = s(t) + \eta(t) \tag{4-3}$$

with $\eta(t)$ denoting a zero-mean additive complex white Gaussian noise with variance $\sigma^2 = N_0/2$ per real and imaginary components and, power spectral density of $N_0/2$.

A weighted estimate of s_k can be derived from (4-2) with the following expression

$$h_2\hat{s}_k^{(2)} = \begin{bmatrix} 0 & h_2 & 0 \end{bmatrix}\left(j^k\mathbf{A}\right)^{\dagger}\begin{bmatrix} r_k \\ r_{k+\frac{1}{2}} \end{bmatrix} \tag{4-4}$$

Making the change $k \to k-1$ to see the demodulator in the previous symbol-time duration results in a second estimate for s_k

$$h_1\hat{s}_k^{(1)} = \begin{bmatrix} h_1 & 0 & 0 \end{bmatrix}\left(j^{k-1}\mathbf{A}\right)^{\dagger}\begin{bmatrix} r_{k-1} \\ r_{k-\frac{1}{2}} \end{bmatrix} \tag{4-5}$$

Also, with $k \to k+1$ for the demodulator, a symbol-time duration after the current one results in a third estimate for s_k

$$h_3\hat{s}_k^{(3)} = \begin{bmatrix} 0 & 0 & h_3 \end{bmatrix}\left(j^{k+1}\mathbf{A}\right)^{\dagger}\begin{bmatrix} r_{k+1} \\ r_{k+\frac{3}{2}} \end{bmatrix} \tag{4-6}$$

In this way, from (4-1) and from (4-4), (4-5) and (4-6), the estimated symbol $\hat{s}_k$ can be

written as a linear combination of the samples $[r_{k-1}, r_{k-\frac{1}{2}}, ..., r_{k+\frac{3}{2}}]$ as follows

$$\hat{s}_k = \begin{bmatrix} W_1 & W_2 & \dots & W_6 \end{bmatrix} \begin{bmatrix} r_{k-1} \\ r_{k-\frac{1}{2}} \\ \vdots \\ r_{k+\frac{3}{2}} \end{bmatrix} \tag{4-7}$$

From (4-5) and with $\mathbf{\Lambda} = \mathbf{A}^{\dagger}$, the coefficient $W_1 \in \mathbb{C}$ can be calculated as

$$W_1 = h_1 \begin{bmatrix} 1 & 0 & 0 \end{bmatrix} \frac{1}{j^{k-1}} \mathbf{\Lambda} \begin{bmatrix} 1 \\ 0 \end{bmatrix} = \frac{h_1}{j^{k-1}} \mathbf{\Lambda}_{11} \tag{4-8}$$

Similarly, the remaining coefficients, $W_i \in \mathbb{C}$, can be calculated as

$$\begin{aligned} W_2 &= \frac{h_1}{j^{k-1}} \Lambda_{12} \qquad W_3 = \frac{h_2}{j^{k}} \Lambda_{21} \\ W_4 &= \frac{h_2}{j^{k-1}} \Lambda_{22} \qquad W_5 = \frac{h_3}{j^{k+1}} \Lambda_{31} \\ W_6 &= \frac{h_6}{j^{k+1}} \Lambda_{32} \end{aligned} \tag{4-9}$$

It is important to note that the coefficients W_i are computed offline since the matrix $\mathbf{A}$ is known a priori.

4.3.2 LPIE1s-detector system model

Because LPIE-2S demodulation scheme requires two samples per symbol-time duration, the following implementation of LPIE, hereafter named LPIE-1S, consists of taking one sample per symbol-time duration. Four estimates associated with one symbol are obtained. Hence, the resulting symbol estimate is given by

$$\hat{s}_k = \sum_{m=1}^{4} h_m \hat{s}_k^{(m)} \tag{4-10}$$

where the super-index 1 refers to the estimate of s_k obtained two symbol-time durations ago; likewise, supper-index 2, 3, and 4 refer to the estimate of s_k obtained from the previous, the current, and the subsequent symbol-time durations, respectively.

From (3-48), two consecutive samples are

$$\hat{x}_k = j^k (A_{11} s_{k+1} + A_{12} s_k + A_{13} s_{k-1}) \tag{4-11}$$

$$\hat{x}_{k+1} = j^{k+1} (A_{11} s_{k+2} + A_{12} s_{k+1} + A_{13} s_k) \tag{4-12}$$

Both (4-11) and (4-12) can be written as

$$\begin{bmatrix} \hat{x}_k \\ \hat{x}_{k+1} \end{bmatrix} = j^k \mathbf{B} \begin{bmatrix} s_{k+2} \\ s_{k+1} \\ s_k \\ s_{k-1} \end{bmatrix} \tag{4-13}$$

with

$$B = \begin{bmatrix} 0 & A_{11} & A_{12} & A_{13} \\ jA_{11} & jA_{12} & jA_{13} & 0 \end{bmatrix} \tag{4-14}$$

Thus, four received symbols can be estimated from (4-13). Likewise, the structure of the demodulator is given by

$$\begin{bmatrix} s_{k+2}^{(1)} \\ s_{k+1}^{(2)} \\ s_k^{(3)} \\ s_{k-1}^{(4)} \end{bmatrix} = \left(j^k B \right)^{\dagger} \begin{bmatrix} r_k \\ r_{k+1} \end{bmatrix} \tag{4-15}$$

and the weighted estimates for this demodulator are written as

$$\begin{aligned} h_1 \hat{s}_k^{(1)} &= \begin{bmatrix} h_1 & 0 & 0 & 0 \end{bmatrix} (j^{k-2} \mathbf{B})^{\dagger} \begin{bmatrix} r_{k-2} \\ r_{k-1} \end{bmatrix} \\ h_2 \hat{s}_k^{(2)} &= \begin{bmatrix} 0 & h_2 & 0 & 0 \end{bmatrix} (j^{k-1} \mathbf{B})^{\dagger} \begin{bmatrix} r_{k-1} \\ r_k \end{bmatrix} \\ h_3 \hat{s}_k^{(3)} &= \begin{bmatrix} 0 & 0 & h_3 & 0 \end{bmatrix} (j^{k} \mathbf{B})^{\dagger} \begin{bmatrix} r_{k} \\ r_{k+1} \end{bmatrix} \\ h_4 \hat{s}_k^{(4)} &= \begin{bmatrix} 0 & 0 & 0 & h_4 \end{bmatrix} (j^{k+1} \mathbf{B})^{\dagger} \begin{bmatrix} r_{k+1} \\ r_{k+2} \end{bmatrix} \end{aligned} \tag{4-16}$$

resulting in a symbol estimate expressed as

$$\hat{s}_k = \begin{bmatrix} W_1 & W_2 & \dots & W_5 \end{bmatrix} \begin{bmatrix} r_{k-2} \\ r_{k-1} \\ \vdots \\ r_{k+2} \end{bmatrix} \tag{4-17}$$

Defining $\boldsymbol{\beta} = \mathbf{B}^{\dagger}$, the coefficients $W_i \in \mathbb{C}$ can be calculated as

$$
\begin{aligned}
W_1 &= \frac{h_1}{j^{k-2}}\beta_{11} \\
W_2 &= \frac{h_1}{j^{k-2}}\beta_{12} + \frac{h_2}{j^{k-1}}\beta_{21} \\
W_3 &= \frac{h_2}{j^{k-1}}\beta_{22} + \frac{h_3}{j^{k-2}}\beta_{31} \\
W_4 &= \frac{h_3}{j^{k}}\beta_{32} + \frac{h_4}{j^{k+1}}\beta_{41} \\
W_5 &= \frac{h_4}{j^{k+1}}\beta_{42}
\end{aligned}
\tag{4-18}
$$

Due to the imperfections of the demodulation, the output of these two proposals are complex in general. So, the following real random variable can describe the output of the demodulators

$$\Gamma = \Re\{\hat{s}_k\} \tag{4-19}$$

where $\Re\{\cdot\}$ is the real component of $\{\cdot\}$.

4.3.3 Error performance of LPIE2S-detector

In this section, the error performance is calculated when the transmitted signal is in the presence of AWGN. Based on the demodulation scheme proposed in (4-2) for LPIE-2S and considering (4-19), the probability of error is defined as

$$P_e = P\left(\{\Gamma > 0\} \cap A_0\right) + P\left(\{\Gamma < 0\} \cap A_1\right) \tag{4-20}$$

where $A_0 = \{s_k = -1\}$ and $A_1 = \{s_k = 1\}$. The definition in (4-20) describes the probability that: a binary symbol, $s_k = -1$, is transmitted and the received and decoded symbol is $\hat{s}_k = 1$, or a binary symbol, $s_k = 1$, is transmitted and the received and decoded symbol is $\hat{s}_k = -1$. Therefore (4-20) can be rewritten as

$$P_e = P\left(\Gamma > 0 \middle| A_0\right) P\left(A_0\right) + P\left(\Gamma < 0 \middle| A_1\right) P\left(A_1\right) \tag{4-21}$$

Since s_k is a discrete random variable with a uniform probability distribution over the set $\{-1,1\}$, then

$$P(A_0) = P(A_1) = \frac{1}{2} \tag{4-22}$$

It can be demonstrated that

$$P(\Gamma > 0 | A_0) = P(\Gamma < 0 | A_1) \tag{4-23}$$

so, using (4-22) and (4-23), (4-21) can be simplified to

$$P_e = P(\Gamma < 0 | A_1). \tag{4-24}$$

Using the conditional probability of Γ defined as

$$P(\Gamma \in B | A_i) = \int_B f_{\Gamma|A_i}(\gamma) d\gamma \tag{4-25}$$

where $f_{\Gamma|A_i}(\gamma)$ is the conditional probability density function, B is any subset of the real numbers and A_i represents the binary events previously described, the probability of error is

$$P_e = \int_{-\infty}^{0} f_{\Gamma|A_i}(\gamma) d\gamma \tag{4-26}$$

Since the demodulator is a linear system, for analysis purposes (4-26) can be calculated by first obtaining $f_{\Gamma|A_1}(\gamma) d\gamma$ and considering the communication system without noise, and then combining the result with the filtered noise.

Taking as a reference [Liang-97] the transmitted signal can be expressed as

$$\begin{aligned} x_k &= \exp\left(j s_{k+1} s_k \phi_0 + j s_k s_{k-1} \phi_2\right) j^k s_{k-1} \\ x_{k+1/2} &= \exp\left(j s_{k+1} s_k \phi_1 + j s_k s_{k-1} \phi_3\right) j^k s_{k-1} \end{aligned} \tag{4-27}$$

Assuming $s_k = 1$, which corresponds to the event A_1, then the discrete random variable x_k takes values from a finite set of the complex numbers given by the combinations of the possible outcomes of s_{k-1} and s_{k+1}, i.e., s_{k-1} and s_{k+1} can only take two values; this implies that x_k can only take four values in (4-27). Therefore, the conditional probability density function of x_k can be expressed as

$$f_{x_k|A_1}(x) = \frac{1}{4} \sum_{m=1}^{4} \delta\left(x - x_k^{(m)}\right) \tag{4-28}$$

where $\delta(x)$ is the Dirac delta and $x_k^{(m)}$ stands for the value of x_k using the m-th combination of the random variables s_{k-1} and s_{k+1}.

Let γ_k be defined as Γ in the k-th symbol-time duration without noise. Using the output of the linear demodulator described in (4-7) and incorporated in (4-19), it can be observed that γ_k depends on x_{k-1}, $x_{k-1/2}$, x_k, $x_{k+1/2}$, x_{k+1}, $x_{k+3/2}$. Computing each one of these samples with (4-27), it becomes evident that all together depend on the random variables s_{k-2}, s_{k-1}, s_{k+1} and s_{k+2}, assuming s_k is known. With all these premises, γ_k is a discrete random variable that can take a value in a discrete set of the real numbers with 2^4 possible outcomes (i.e., it is a function of four independent random variables that take only two values).

Knowing all the possible outcomes, the probability density function (PDF) of γ_k is written as

$$f_{\gamma_k|A_1}(\gamma) = \frac{1}{M}\sum_{m=1}^{M}\delta\left(\gamma-\gamma_k^{(m)}\right) \tag{4-29}$$

where $M=16$ and $\gamma_k^{(m)}$ is the m-th possible outcome of γ_k.

Considering the case with only noise at the input of the demodulator, it can be noticed from (4-7) that the output of LPIE-2S is a linear combination of six independent and identically distributed (i.i.d.) circularly symmetric complex normal random variables, where the real and imaginary parts have a PDF of

$$f_{\mathcal{N}}(\eta) = \frac{1}{\sqrt{2\pi}\sigma}\exp\left(-\frac{\eta^2}{2\sigma^2}\right) \tag{4-30}$$

with a mean of zero and a variance of σ^2.

It is known that a linear combination of Gaussian random variables is also a Gaussian random variable. If the six samples of the noise are labeled as η_i for $i\in\{1,2,\ldots,6\}$, then the output of the demodulator ξ, i.e., the filtered noise, is

$$\xi = \Re\left\{\sum_{i=1}^{6} W_i\eta_i\right\} \tag{4-31}$$

where W_i stands for the coefficients of the filter that describes the demodulator in (4-7).

The variance of ξ can be obtained as

$$\begin{aligned}
\mathrm{var}(\xi) &= \mathrm{var}\left(\Re\left\{\sum_{i=1}^{6} W_i \eta_i\right\}\right) \\
&= \sum_{i=1}^{6} \mathrm{var}\left(\Re\left\{W_i \eta_i\right\}\right) \\
&= \sum_{i=1}^{6} \mathrm{var}\left(\Re\left\{W_i\right\}\Re\left\{\eta_i\right\} - \Im\left\{W_i\right\}\Im\left\{\eta_i\right\}\right) \\
&= \sum_{i=1}^{6} \Re\left\{W_i\right\}^2 \mathrm{var}\left(\Re\left\{\eta_i\right\}\right) + \Im\left\{W_i\right\}^2 \mathrm{var}\left(\Im\left\{\eta_i\right\}\right) \\
&= \sum_{i=1}^{6} \left|W_i\right|^2 \sigma^2 = \sigma^2 G^2
\end{aligned} \tag{4-32}$$

where

$$G^2 = \sum_{i=1}^{6} \left|W_i\right|^2 \tag{4-33}$$

and $\Im\{\cdot\}$ is the imaginary component of $\{\cdot\}$. Then ξ has a PDF expressed as

$$f_{\Xi}(\xi) = \frac{1}{\sqrt{2\pi}\sigma G} \exp\left(-\frac{\xi^2}{2\sigma^2 G^2}\right) \tag{4-34}$$

Using the above results and knowing that the PDF of the sum of two independent random variables is the convolution of their PDF's [Leon-Garcia-08], then

$$f_{\Gamma|A_1}(\gamma) = f_{\gamma_k|A_1} * f_{\Xi}(\gamma) \tag{4-35}$$

Substituting (4-29) and (4-34) in (4-35) leads to

$$f_{\Gamma|A_1}(\gamma) = \left(\frac{1}{M}\sum_{m=1}^{M} \delta\left(\gamma - \gamma_k^{(m)}\right)\right) * \left(\frac{1}{\sqrt{2\pi}\sigma G} \exp\left(-\frac{\gamma^2}{2\sigma^2 G^2}\right)\right) \tag{4-36}$$

Using the property

$$\delta(x-a) * f(x) = f(x-a) \tag{4-37}$$

then (4-36) results in

$$f_{\Gamma|A_1}(\gamma) = \frac{1}{M\sqrt{2\pi}\sigma G} \sum_{m=1}^{M} \exp\left(-\frac{\left(\gamma - \gamma_k^{(m)}\right)^2}{2\sigma^2 G^2}\right) \tag{4-38}$$

Substituting (4-38) in (4-26) the error probability is

$$P_e = \frac{1}{M\sqrt{2\pi}G} \sum_{m=1}^{M} \int_{-\infty}^{0} \exp\left(-\frac{\left(\gamma - \gamma_k^{(m)}\right)^2}{2\sigma^2 G^2}\right) d\gamma \tag{4-39}$$

It can be shown that

$$\int_{-\infty}^{0} \exp\left(-\frac{(x-a)^2}{b}\right) dx = \frac{\sqrt{\pi b}}{2} \operatorname{erfc}\left(\frac{a}{\sqrt{b}}\right) \tag{4-40}$$

where

$$\operatorname{erfc}(x) = \frac{2}{\sqrt{\pi}} \int_{x}^{\infty} \exp\left(-u^2\right) du \tag{4-41}$$

Then, applying (4-40) in (4-39) leads to

$$P_e = \frac{1}{2M} \sum_{m=1}^{M} \operatorname{erfc}\left(\frac{\gamma_k^{(m)}}{\sqrt{2}\sigma G}\right) \tag{4-42}$$

The signal-to-noise ratio (SNR) is related to σ by

$$SNR = 10 \log_{10}\left(T \cdot f_s \frac{P_x}{\sigma^2}\right) \tag{4-43}$$

where T is the symbol period, f_s is the sampling frequency and P_x is the power of the modulated signal calculated as

$$\begin{aligned} P_x &= \lim_{\rho \to \infty} \frac{1}{\rho} \int_{-\rho/2}^{\rho/2} \left|x(t)\right|^2 dt \\ &= \lim_{\rho \to \infty} \frac{1}{\rho} \int_{-\rho/2}^{\rho/2} \left|\exp\left(j\varphi(t)\right)\right|^2 dt = 1 \end{aligned} \tag{4-44}$$

Then using $T \cdot f_s = 2$

$$\sigma^2 = 2 \cdot 10^{-\frac{SNR}{10}} \tag{4-45}$$

4.3.4 Error Performance of LPIE1S-detector

In order to determine the error probability of the demodulator LPIE-1S, it can be observed from the expressions of the estimated symbols in (4-7) and (4-17), that all of them are linear combinations of the received samples weighted by the W_i coefficients. Given this fact, (4-42) can be used for obtaining the error probability of LPIE-1S considering the following arguments:

The value of G is obtained by

$$G^2 = \sum_{i=1}^{5} |W_i|^2 \tag{4-46}$$

where W_i belongs to the LPIE-1S demodulator.

The parameter M in (4-29) can be calculated taking into account the fact that the output of the demodulation filter depends on x_{k-2}, x_{k-1}, …, x_{k+2} and consequently on the six transmitted symbols s_{k-3}, s_{k-2}, s_{k-1}, s_{k+1}, s_{k+2} and s_{k+3}. Therefore γ_k has $M = 2^6$ possible outcomes labeled as $\gamma_k^{(m)}$.

In addition, $T \cdot f_s = 1$ because this demodulator uses one sample per symbol. Hence, the relation between σ and the SNR is

$$\sigma^2 = 10^{-\frac{\text{SNR}}{10}} \tag{4-47}$$

4.3.5 Optimal parameters and computational complexity for LPIE

Due to LPIE performance depends on the value of h_m coefficients, this section describes how they can be chosen by considering the error probability function with the goal of achieving the best performance of the proposed demodulator.

Let $\mathbf{h} = (h_1, h_2, h_3) \in \mathbb{R}^3$ for LPIE-2S and $\mathbf{h} = (h_1, h_2, h_3, h_4) \in \mathbb{R}^4$ for 1S. Then the probability error at a certain SNR can be viewed as a function of $\mathbf{h}$.

The function $P_e(\mathbf{h})$ is indeterminate at $\mathbf{h} = 0$ because it would imply that $\hat{s}_k = 0$, so it is impossible to determine which symbol it represents. It can also be observed that the same value of error probability is achieved for $\mathbf{h}_0$ and $\ell\mathbf{h}_0$ $\forall \ell > 0$, because both points differ only by a positive scalar that does not alter the detection of $\hat{s}_k$.

Therefore, the lines $\mathbf{h} = \ell\mathbf{h}_0$ with $\ell \in (0, \infty)$ are level hypersurfaces of $P_e(\mathbf{h})$. This last statement implies that every proposed value for $\mathbf{h} \neq 0$ can be normalized, so the only relevant place to look for possible values of $\mathbf{h}$ is on the unit hyper-sphere $\|\mathbf{h}\| = 1$, where $\|\mathbf{h}\|$ denotes the Euclidean norm of $\mathbf{h}$. The contour map of $P_e(\mathbf{h})$ for LPIE-2S, considering $SNR = 7\ dB$ and maintaining $h_3 = 0$, is shown in Fig. 4.1. It can be observed how $P_e(\mathbf{h})$ stays constant when

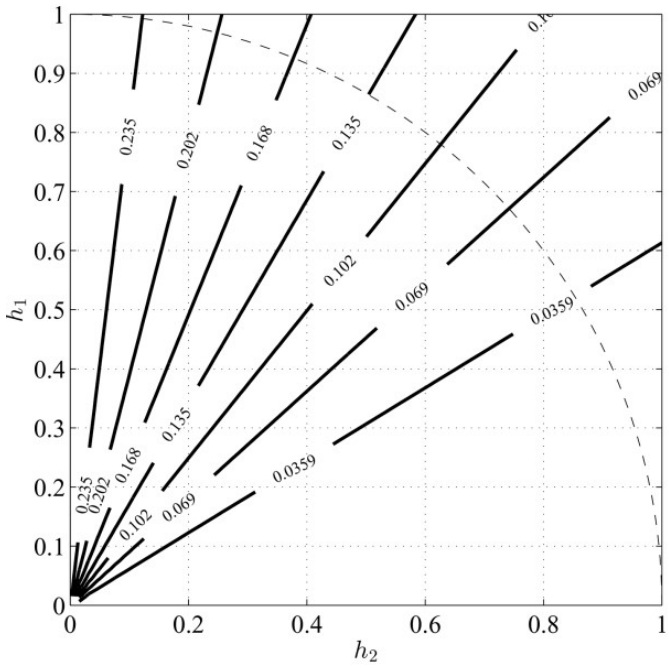

Fig. 4.1 Contour map of $P_e(\mathbf{h})$ for LPIE-2S at $SNR = 7\ dB$ with $h_3 = 0$.

moving along radial lines from the origin, since they correspond to level hypersurfaces of $P_e(\mathbf{h})$. The projection on the plane of the unit sphere $\|\mathbf{h}\| = 1$ is shown in a dotted line, showing that restricting the search space to this surface does not alter the result.

In order to propose a set of possible values of $\mathbf{h}$, a minimization of $P_e(\mathbf{h})$, at a different SNR, was solved (at least locally). The problem is stated as follows:

$$\begin{aligned} &min\ P_e(h), \\ &\text{s.t. } \|h\| = 1. \end{aligned} \tag{4-48}$$

A set of solutions to the problem in (4-48) for different values of SNR are shown in Fig. 4.2. These values were obtained using the interior point algorithm [Byrd-00] with a function tolerance of 10^{-12} and a constraint tolerance of 10^{-6}. It is important to note that these solutions do not intend to guarantee global optimality of (4-48). The optimization algorithm was executed for different SNR values to observe how the solutions for $\mathbf{h}$ change in different conditions. From Fig. 4.2, it can be observed that the numerical solutions for $\mathbf{h}$, which the numerical solver delivered, remained at the same point, for practical purposes, overall tested

TABLE 4.1. VALUES OF **h** FOR THE TWO PROPOSED DEMODULATORS

	h_1	h_2	h_3	h_4
LPIE-2S	0.0731	0.9946	0.0731	n/a
LPIE-1S	0.5293	0.1689	0.7209	0.4090

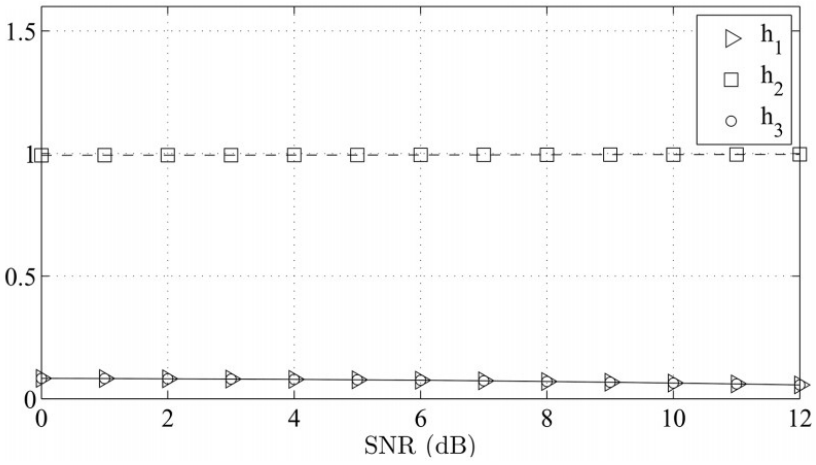

a)

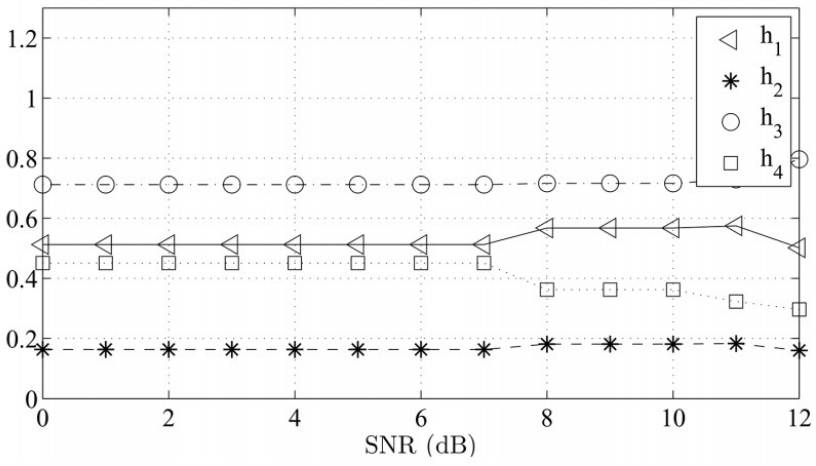

b)

Fig. 4.2 Values of h obtained from solving (4-48) at different values of SNR for LPIE a) Numerical solutions of for LPIE-2S and different values of SNR, b)Numerical solutions of for LPIE-1S and different values of SNR.

SNR values, and the dominant coefficient is h_2 for LPIE-2S.

Table 4.1 shows the mean values of **h** for all tested *SNR* values (from 0 to 12 *dB*). These values will be used in the next section. Moreover, since the optimal parameter **h**, the matrices **A**,

TABLE 4.2. COMPUTATIONAL COMPLEXITY FOR LPIE

	Multiplications	Additions
LPIE-2S	6	5
LPIE-1S	5	4

$\mathbf{\Lambda}$ and the weight W_i are calculated off-line, the complexity of computing every symbol estimate in (4-7) and (4-17), is shown in Table 4.2.

4.3.6 Theoretical and Simulated Performance results for LPIE2s and LPIE1s

In this section, the simulated performance, and the complexity of the LPIE demodulator is presented. The simulation scenario uses either linear or exact GFSK baseband modulators. Likewise, the demodulators employed were the LPIE and the Viterbi-based for GFSK signaling with a modulation index of 0.5. Frames with 10^6 binary symbols were injected into the modulator, computing the BER until 100 frames were processed or 10^3 errors were detected for each value of SNR; this allows the BER values to be statistically representative. Furthermore, the error probability of binary PSK (BPSK) digital modulation is used as a lower boundary.

An AWGN channel with a mean of zero. Its variance is computed using (4-45) and (4-47) for the LPIE-2S and LPIE-1S, respectively, and SNR values between $0\,dB$ and $9\,dB$ are considered.

The modulators were configured with the following parameters: a bandwidth-time product (BT) of 0.5, a pulse g(t) with $L = 3$ symbol periods, and a bit rate R_b of 10^6 bps. The LPIE was configured considering a time deviation of $T_d = 0.25T$, $BT = 0.5$ and the elements of $\mathbf{h}$, computed off-line (before execution) by minimizing the error probability, were taken from Table 4.1. The GFSK Viterbi parameters considered were a pulse length of 3 symbol periods, $BT = 0.5$ and a traceback of 20 symbol periods.

Fig. 4.3 considers the exact modulator (direct generation of GFSK signals) and shows the

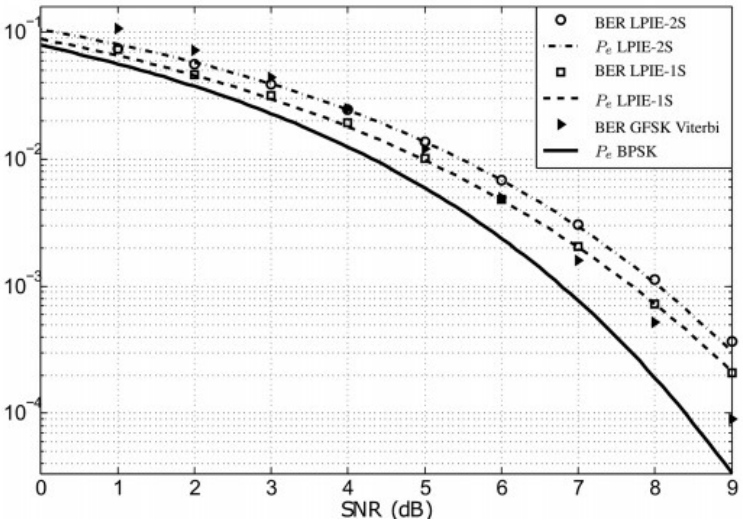

Fig. 4.3 BER performance comparison between the LPIE-2S, the LPIE-1S (theoretical and simulated), the BPSK and the optimal Viterbi demodulator.

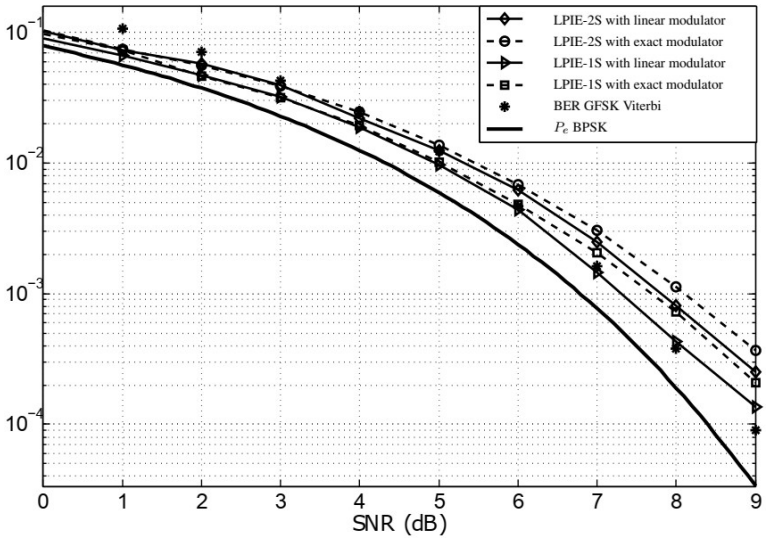

Fig. 4.4 BER performance comparison between the LPIE-2S and the LPIE-1S using linear and exact modulators at the transmitter.

simulated and error probability of the LPIE-2S and LPIE-1S. In addition, the BER performance of the GFSK Viterbi and the error probability of the BPSK are included. It can be seen that the performance of all the proposed demodulators meets the specification for the BLE standard (BER of 0.1% at SNR of $21\ dB$) considering $\lambda = 0.5$.

Furthermore, it can be observed that the LPIE-1S performs better than the LPIE-2S, maintaining an advantage of $0.3\ dB$. Unlike the Viterbi modulator that maintains a nearly constant distance from BPSK, LPIE implementations are closer to BPSK at low SNR values and separate from BPSK as the SNR increases.

Fig. 4.4 shows the BER performance of the linear modulator [Liang-97] described in Section 3.2 and the exact one using the LPIE-2S and LPIE-1S at the receiver. It can be observed that the LPIE has a similar performance when it works with both modulators, and in this sense, it is a robust demodulator.

4.4. A low complexity GFSK detector for IoT devices based on the transformation of the IQ components

Regarding the detection process of GFSK, the optimal receiver uses a maximum likelihood sequence estimator (MLSE). However, its implementation requires a high amount of hardware resources (e.g., memory and processing units), which are limited in IoT platforms.

The Viterbi algorithm can be used as a sequence detector because it reduces the number of sequences in the search as new data arrives at the receiver [Proakis-08], [Fonseka-99]. Even though the VA is less computationally expensive, its hardware resources usage is still unfeasible for most IoT applications. Thus, the reduction of implementation complexity while maintaining a performance close to the MLSE is a problem of interest. In this section, a GFSK receiver based on a new paradigm that transforms the GFSK baseband signal into a signal with a uniform quantized phase is described. This contribution was published in IEEE Internet of Things Journal [Valencia-Velasco-20].

4.4.1 IQT-detector system model

In Fig. 4.5 is shown the block diagram of the GFSK communication system with the IQT-detector. Each block will be discussed in the following sections, as is required. The GFSK

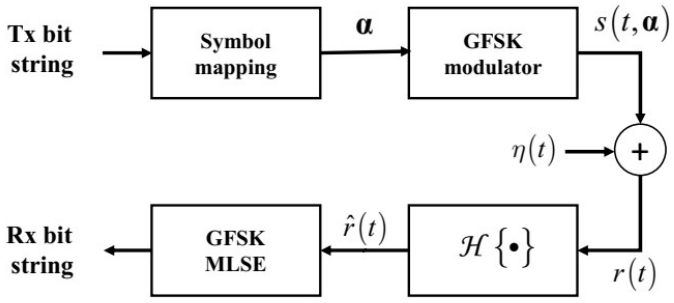

Fig. 4.5 Proposed block diagram of a GFSK wireless communication system.

modulator takes N symbols represented by $\boldsymbol{\alpha}=\{\alpha_0,\alpha_1,\alpha_2,\ldots\alpha_{N-1}\}$ and generates the complex envelope signal described in (2-1). Splitting the phase signal described in (2-2) into two contributions:

$$\varphi(t,\boldsymbol{\alpha})=\sum_{i=k-L+1}^{k}\alpha_i\Phi(t-iT)+\sum_{i=0}^{k-L}\alpha_i\Phi(t-iT) \tag{4-49}$$

and considering (1-14), the second contribution can be simplified; thus, (4-49) can be rewritten as

$$\begin{aligned}\varphi(t,\boldsymbol{\alpha})&=\sum_{i=k-L+1}^{k}\alpha_i\Phi(t-iT)+\frac{\pi}{2}\sum_{i=0}^{k-L}\alpha_i \qquad \text{mod } 2\pi\\ &=\theta(t,\alpha_k,\ldots,\alpha_{k-L+1})+\theta_k \qquad kT\le t<(k+1)T\end{aligned} \tag{4-50}$$

where $\theta(t,\alpha_k,\ldots,\alpha_{k-L+1})$ is the phase contribution in $[kT,(k+1)T]$ determined by the current symbol and the previous $L-1$ symbols, and θ_k represents the cumulate phase up to time $(k-L)T$. For instance, considering (4-50) with $\lambda=0.5$, $BT=0.5$ and a partial response of $L=3$, the complex envelope results in

$$s(t,\boldsymbol{\alpha})=\sqrt{\frac{E_s}{T}}\exp\left\{j\left(\alpha_k\Phi(t-kT)+\alpha_{k-1}\Phi(t-(k-1)T)+\alpha_{k-2}\Phi(t-(k-2)T)+j\theta_k\right)\right\} \tag{4-51}$$

Now, considering that the signal (4-51) is transmitted over a Gaussian noise channel, the received baseband signal $r(t)$, can be described as

$$r(t)=s(t,\boldsymbol{\alpha})+\eta(t) \tag{4-52}$$

TABLE 4.3. QUANTIZED PHASE SIGNAL VALUES

Phase signal $\varphi(t,\boldsymbol{\alpha})$	Corresponding quantized phase signal $\hat{\varphi}(t,\boldsymbol{\alpha})$ value	$cos(\hat{\varphi}(t,\boldsymbol{\alpha}))$	$sin(\hat{\varphi}(t,\boldsymbol{\alpha}))$
$[0, \pi/2)$	$\pi/4$	$\sqrt{\frac{1}{2}}$	$\sqrt{\frac{1}{2}}$
$[\pi/2, \pi)$	$3\pi/4$	$-\sqrt{\frac{1}{2}}$	$\sqrt{\frac{1}{2}}$
$[\pi, 3\pi/2)$	$5\pi/4$	$-\sqrt{\frac{1}{2}}$	$-\sqrt{\frac{1}{2}}$
$[3\pi/2, 2\pi)$	$7\pi/4$	$\sqrt{\frac{1}{2}}$	$-\sqrt{\frac{1}{2}}$

where $\eta(t)$ is a zero-mean additive complex white Gaussian noise with variance $\sigma^2 = N_0/2$ per real and imaginary components and power spectral density of $N_0/2$.

The I and Q components of the baseband signal at the receiver end are transformed into the values -1 and $+1$. This transformation is obtained by the uniform quantization of the phase signal, $\varphi(t,\boldsymbol{\alpha})$, with a step size of $\frac{\pi}{2}$ and an offset of $\frac{\pi}{4}$, as follows:

$$\hat{\varphi}(t,\boldsymbol{\alpha}) = \frac{\pi}{2}\left\lfloor \frac{2}{\pi}\varphi(t,\boldsymbol{\alpha}) \right\rfloor + \frac{\pi}{4} \tag{4-53}$$

where $\lfloor \bullet \rfloor$ is the floor operation, note that the $\hat{\varphi}(t,\boldsymbol{\alpha}) \mod 2\pi$ can only take values in $\left\{\frac{\pi}{4}, \frac{3\pi}{4}, \frac{5\pi}{4}, \frac{7\pi}{4}\right\}$. An example of this quantized phase is shown in Fig. 4.6. It can be observed that the quantized phase signal follows very close to the shape of the phase signal. Table 4.3 shows the quantize phase values according to the range of the phase signal.

Considering (2-1) and the values presented in Table 4.3, the corresponding complex envelope of the quantized phase can be described as

$$\begin{aligned} \hat{s}(t,\boldsymbol{\alpha}) &= \sqrt{E_s/T}\exp\left\{j\hat{\varphi}(t,\boldsymbol{\alpha})\right\} = \sqrt{E_s/T}\left(\cos\left(\hat{\varphi}(t,\boldsymbol{\alpha})\right) + j\sin\left(\hat{\varphi}(t,\boldsymbol{\alpha})\right)\right) \\ &= \sqrt{E_s/2T}\left(sign\left(\cos\left(\varphi(t,\boldsymbol{\alpha})\right)\right) + jsign\left(\sin\left(\varphi(t,\boldsymbol{\alpha})\right)\right)\right) \end{aligned} \tag{4-54}$$

with

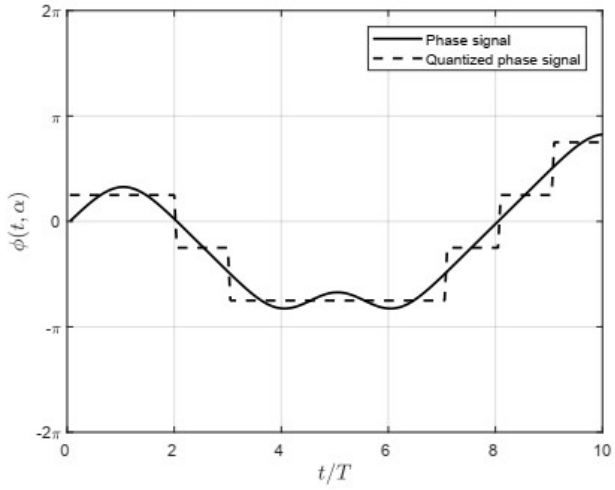

Fig. 4.6 Continuous and quantized phase signal for the symbols $\{-1,-1,-1,+1,-1,+1,+1,+1,+1,-1\}$ using GFSK.

$$sign(x)=\begin{cases}+1 & \text{if } x\geq 0\\ -1 & \text{if } <0\end{cases} \tag{4-55}$$

Such description of the received signal is convenient since it can be represented using only ± 1 instead of an infinite number of values in the interval $[+1,-1]$. An example of this signal is depicted in Fig. 4.7.

This motivate the introduction of the following operator

$$\mathcal{H}\{\bullet\}=\sqrt{E_s/T}\left(sign\left(Re\{\bullet\}\right)+jsign\left(Im\{\bullet\}\right)\right) \tag{4-56}$$

Hence, (4-54) can be expressed as $\hat{s}(t,\alpha)=\mathcal{H}\{s(t,\boldsymbol{\alpha})\}$ and with reference to Fig. 4.5, $\hat{r}(t)=\mathcal{H}\{r(t)\}$ which corresponds to the transformation of the received signal $r(t)$ according to (4-56). In this way, $\hat{r}(t)$ takes values in a finite set of $\sqrt{E_s/T}\{1+j,1-j,-1+j,-1-j\}$.

The complex envelope of the quantized phase signal described in (4-54) can be represented as a quadrature phase shift keying (QPSK) baseband signal. Note that from (4-53) and according to Table 4.3, $\hat{\varphi}(t,\boldsymbol{\alpha})$ mod 2π can only take values in $\{\frac{\pi}{4},\frac{3\pi}{4},\frac{5\pi}{4},\frac{7\pi}{4}\}$. Therefore, by expanding all

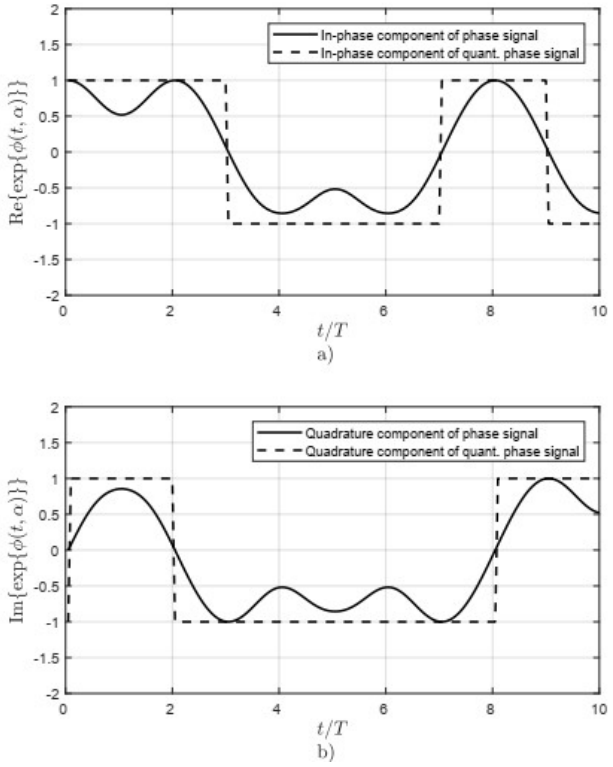

Fig. 4.7 Complex envelope components for the continuous and quantized phase signal using GFSK. a) In-phase component, b) Quadrature component.

possible values of (4-53) in terms of $\alpha_k, \alpha_{k-1}, \alpha_{k-2}$ and θ_k the following relation is obtained:

$$\begin{aligned} \hat{\varphi}_k &:= \hat{\varphi}(t, \boldsymbol{\alpha}) = \frac{\pi}{2}\Theta_k + \frac{\pi}{4} \qquad kT \le t < (k+1)T \\ \Theta_k &= \tfrac{1}{2}\left(\alpha_k + \alpha_{k-1}\right) + \Theta_{k-1} \end{aligned} \tag{4-57}$$

with $\Theta_{-1} = 0$. These conditions can be summarized by the following: the phase $\hat{\varphi}_k$ increases with respect to $\hat{\varphi}_{k-1}$ if

$$\alpha_k = \alpha_{k-1} = 1 \tag{4-58}$$

decreases if

$$\alpha_k = \alpha_{k-1} = -1 \tag{4-59}$$

and stays the same if

$$\alpha_k \neq \alpha_{k-1} \tag{4-60}$$

Henceforth, (4-54) can be rewritten as

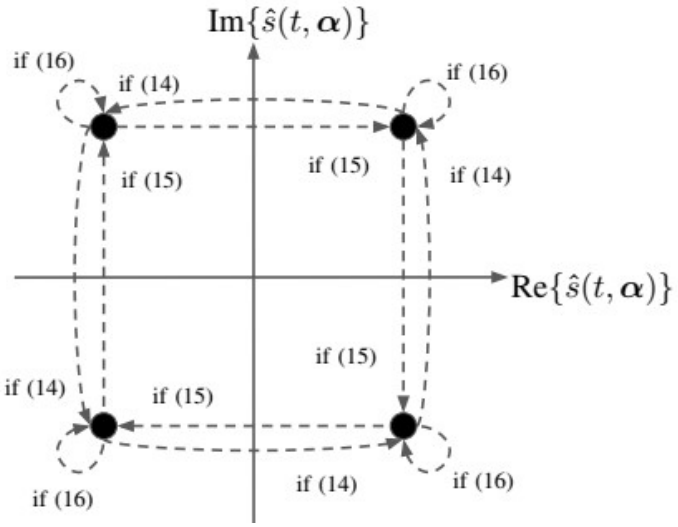

Fig. 4.8 State transitions for $\hat{s}(t,\boldsymbol{\alpha})$ from an interval $(k-1)T \le t < kT$ to $kT \le t < (k+1)T$.

$$\hat{s}(t,\boldsymbol{\alpha}) = \sqrt{E_s/T}\,\exp\{j\hat{\varphi}_k\} \qquad kT \le t < (k+1)T$$
$$\hat{\varphi}_k \mod 2\pi \in \left\{\frac{\pi}{4}, \frac{3\pi}{4}, \frac{5\pi}{4}, \frac{7\pi}{4}\right\} \tag{4-61}$$

which is a representation of a $\frac{\pi}{4}-QPSK$ signal where the input sequence of symbols α is encoded through the state machine to obtain the new sequence of 4-ary symbols $\{\hat{\varphi}_0,\ldots\hat{\varphi}_{N-1}\}$. The phase transitions are represented graphically in Fig. 4.8. For example, considering (4-57) and the input sequence $\boldsymbol{\alpha} = \{-1,-1-1,+1-1,+1,+1,+1,+1,-1\}$, the values of $\hat{\varphi}_k$ are $\left\{\frac{\pi}{4},\frac{\pi}{4},\frac{-\pi}{4},\frac{-3\pi}{4},\frac{-3\pi}{4},\frac{-3\pi}{4},\frac{-3\pi}{4},\frac{-\pi}{4},\frac{\pi}{4},\frac{3\pi}{4},\right\}$.

Hence, the transition rule of the total state vector $\boldsymbol{\sigma}_k$ over the time intervals can be represented by the following vector equation:

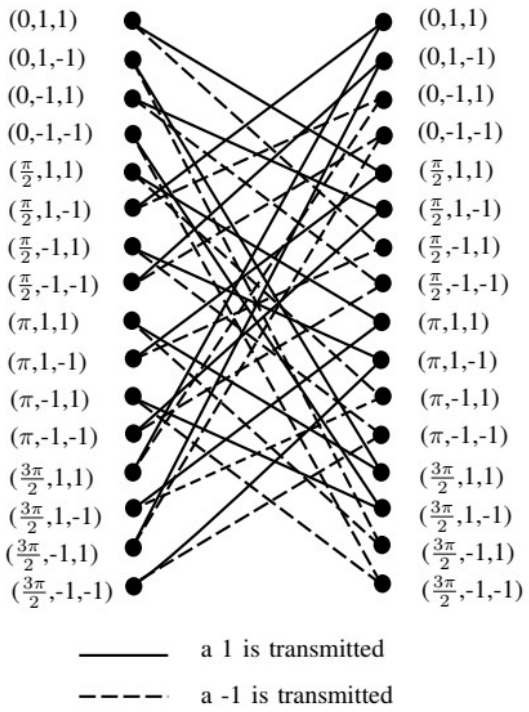

Fig. 4.9 Trellis diagram for a GFSK signal with modulation index of 0.5 and pulse length of 3 symbol periods.

$$\boldsymbol{\sigma}_{k+1} = \begin{pmatrix} 1 & 0 & \frac{\pi}{2} \\ 0 & 0 & 0 \\ 0 & 1 & 0 \end{pmatrix} \boldsymbol{\sigma}_k + \begin{pmatrix} 0 \\ 1 \\ 0 \end{pmatrix} \alpha_k \tag{4-62}$$

Note that since θ_k can only take values in $\left\{0, \frac{\pi}{2}, \pi, \frac{3\pi}{2}\right\}$ for $\lambda = 0.5$, hence, there are 16 possible combinations for $\boldsymbol{\sigma}_k$ when taking into account only $\theta_k \bmod 2\pi$. Therefore, the trellis diagram can be constructed using the possible states of $\boldsymbol{\sigma}_k$ and the transition rule (4-62), as shown in Fig. 4.9. The trellis diagram is extended for T_b intervals, where T_b is known as the traceback. So that, the goal is to estimate the sequence $\alpha_k, \ldots \alpha_{k+T_b-1}$. A well-known estimation algorithm is the Viterbi algorithm [Forney-73], which obtains the maximum likelihood sequence estimation (MLSE). The received signal is compared with a reference signal in a specific path along the trellis using a likelihood metric. The MLSE is chosen to be the path with the best metric value. Ideally, the traceback value would be large enough to cover the entire received sequence. In practice, a heuristic is applied and T_b can be reduced up to

$$T_b = 5 \cdot \log_2 \left(N_s \right) \tag{4-63}$$

where $N_s = 16$ is the number of possible states in the trellis diagram.

4.4.2 Alternative metrics employed in the IQT-Detector

4.4.2.1 Traditional Metric

Traditionally, the metric used in the Viterbi algorithm for CPM signals is calculated as the Euclidean distance [Proakis-08] between the received signal $r(t)$ and the reference signal considering $\boldsymbol{\sigma}_k$ and α_k:

$$J_k(\alpha_k, \boldsymbol{\sigma}_k) = \frac{T}{E_s} \int_{kT}^{(k+1)T} \left\| r(t) - S\left(t, \alpha_k, \boldsymbol{\sigma}_k\right) \right\|^2 dt \tag{4-64}$$

where $S\left(t, \alpha_k, \boldsymbol{\sigma}_k\right)$ is the reference signal defined as

$$\begin{aligned} S\left(t, \alpha_k, \boldsymbol{\sigma}_k\right) &= \sqrt{\frac{E_s}{T}} exp\left(j\Phi\left(t, \alpha_k, \boldsymbol{\sigma}_k\right)\right) \\ \Phi\left(t, \alpha_k, \boldsymbol{\sigma}_k\right) &= \pi\left(\alpha_k \Phi\left(t - kT\right) + \alpha_{k-1} \Phi\left(t - \left(k-1\right)T\right) + \alpha_{k-2} \Phi\left(t - \left(k-2\right)T\right) + \theta_k\right) \end{aligned} \tag{4-65}$$

Thus, the discrete-time version of (4-64) is described as

$$\bar{J}_k(\alpha_k, \boldsymbol{\sigma}_k) = \frac{T}{E_s} \sum_{n=M_p k}^{M_p(k+1)-1} \left\| r(t) - S\left(n, \alpha_k, \boldsymbol{\sigma}_k\right) \right\|^2 \tag{4-66}$$

where the signal is sampled at a rate of M_p samples per symbol. Note that this approach requires the storing of all the reference sequences $S\left(n, \alpha_k, \boldsymbol{\sigma}_k\right)$ in memory in order to compute the MLSE path. Furthermore, the samples should be represented with a given precision, which can be called a single *word* without loss of generality. The size of the *word* defines the size of the adders, subtractors, and multipliers required to implement (4-66).

4.4.2.2 Metric Proposal 1

The Euclidean distance between the signal $\hat{r}(t) \in \sqrt{E_s/T}\left\{1+j, 1-j, -1+j, -1-j\right\}$ and the reference signal is computed by

$$J_k(\alpha_k,\boldsymbol{\sigma}_k)=\frac{T}{E_s}\int_{kT}^{(k+1)T}\left\|\hat{r}(t)-S\left(t,\alpha_k,\boldsymbol{\sigma}_k\right)\right\|^2 dt \tag{4-67}$$

where $\hat{r}(t)=\mathcal{H}\left\{r\left(t\right)\right\}$ and

$$\mathcal{H}\left\{\bullet\right\}=\sqrt{E_s/T}\left(sign\left(Re\left\{\bullet\right\}\right)+jsign\left(Im\left\{\bullet\right\}\right)\right) \tag{4-68}$$

A discrete-time version of (4-67) is given by

$$\overline{J}_k(\alpha_k,\boldsymbol{\sigma}_k)=\frac{T}{E_s}\sum_{n=M_pk}^{M_p(k+1)-1}\left\|\hat{r}(n)-S\left(n,\alpha_k,\boldsymbol{\sigma}_k\right)\right\|^2 \tag{4-69}$$

Note that in this metric, the real and imaginary components of $\sqrt{T/E_s}\hat{r}(t)$ can only be $+1$ or -1. Therefore, the computational complexity of (4-69) is reduced if the following pre-computed signals are stored in memory:

$$\begin{aligned}
D_1(n,\alpha_k,\boldsymbol{\sigma}_k)&=\left\|(1+j)-\sqrt{\tfrac{T}{Es}}S\left(n,\alpha_k,\boldsymbol{\sigma}_k\right)\right\|^2\\
D_2(n,\alpha_k,\boldsymbol{\sigma}_k)&=\left\|(-1+j)-\sqrt{\tfrac{T}{Es}}S\left(n,\alpha_k,\boldsymbol{\sigma}_k\right)\right\|^2\\
D_3(n,\alpha_k,\boldsymbol{\sigma}_k)&=\left\|(1-j)-\sqrt{\tfrac{T}{Es}}S\left(n,\alpha_k,\boldsymbol{\sigma}_k\right)\right\|^2\\
D_4(n,\alpha_k,\boldsymbol{\sigma}_k)&=\left\|(-1-j)-\sqrt{\tfrac{T}{Es}}S\left(n,\alpha_k,\boldsymbol{\sigma}_k\right)\right\|^2
\end{aligned} \tag{4-70}$$

Consequently, a sample of one of these signals is selected depending on the signs of the real and imaginary part of $\hat{r}(t)$, saving multiplication and subtraction operations, and leaving only *word*-sized additions, but requiring four times memory locations with respect to the traditional metric described in (4-64).

4.4.2.3 Metric Proposal 2

An alternative metric is given by comparing $\hat{r}(n)$ with a reference signal $\hat{S}\left(t,\alpha_k,\boldsymbol{\sigma}_k\right)=\mathcal{H}\left\{S\left(t,\alpha_k,\boldsymbol{\sigma}_k\right)\right\}$:

$$J_k(\alpha_k,\boldsymbol{\sigma}_k)=\frac{T}{4E_s}\int_{kT}^{(k+1)T}\left\|\hat{r}(t)-\hat{S}\left(t,\alpha_k,\boldsymbol{\sigma}_k\right)\right\|^2 dt \tag{4-71}$$

A discrete-time version of (4-71) is computed with

TABLE 4.4. COMPARISON OF HARDWARE RESOURCES BETWEEN THE PROPOSED METRICS.

Metric	*Bus size*	*Adders*	*Subs.*	*Mult.*	*Memory*
Traditional (4-66)	1 *word*	$M_p - 1$	M_p	M_p	$2N_s M_p$ *words*
Metric 1 (4-69)	1 *word*	$M_p - 1$	0	0	$8N_s M_p$ *words*
Metric 2 (4-72)	$2 + \log_2(M_p)$ bits	$M_p - 1$	0	0	$4N_s$ bits

$$\bar{J}_k(\alpha_k, \boldsymbol{\sigma}_k) = \frac{T}{4E_s} \sum_{n=M_p k}^{M_p(k+1)-1} \left\| \hat{r}(n) - \hat{S}\left(n, \alpha_k, \boldsymbol{\sigma}_k\right) \right\|^2 \tag{4-72}$$

It simplifies the required precision for the samples, since both $\hat{r}(t)$ and $\hat{S}\left(n, \alpha_k, \boldsymbol{\sigma}_k\right)$ can be represented using just 2 bits for each one. For instance, let $\{r_R, r_I\}$ represents $\hat{r}(t)$ and $\{S_R, S_I\}$ represents $\hat{S}\left(n, \alpha_k, \boldsymbol{\sigma}_k\right)$ e.g., $\{r_R, r_I\} = \{0\ 1\}$ corresponds to $\sqrt{T/E_s}\hat{r}(t) = 1 - j$. Furthermore, the result of $\left(T/4E_s\right)\left\| \hat{r}(n) - \hat{S}\left(n, \alpha_k, \boldsymbol{\sigma}_k\right) \right\|^2$ can only be 0, 1 or 2 and is represented using 2 bits as well $\{b_1, b_2\}$, where $\{0,0\}$ corresponds to 0, $\{0,1\}$ to 1 and $\{1,0\}$ to 2. The relationship between $\{r_R, r_I, S_R, S_I\}$ and $\{b_1, b_2\}$ can be computed by a look-up table or with the Boolean equations:

$$\begin{aligned} b_1 &= \left(r_R \oplus S_R\right) \odot \left(r_I \oplus S_I\right) \\ b_2 &= \left(r_R \oplus S_R\right) \oplus \left(r_I \oplus S_I\right) \end{aligned} \tag{4-73}$$

where $\oplus$ and $\odot$ stands for XOR and AND logical operations, respectively. With these two bits, the values 0, 1 or 2 are added to the metric described in (4-69). Moreover, the amount of memory is reduced since only two bits are needed to store $\hat{S}\left(n, \alpha_k, \boldsymbol{\sigma}_k\right)$, resulting in a total of $2\left(2N_s\right)$ bits considering all states. Furthermore, the adder bus size is reduced since, in the worst case, the metric results in $2M_p$, which require $2 + \log_2\left(M_p\right)$ bits to be represented.

Note that (4-72) turns out equivalent to the following metric:

TABLE 4.5. HARDWARE RESOURCES CONSIDERING IEEE-754 SINGLE PRECISION. $M_p = 20$ AND $N_s = 16$.

Scheme	*Bus size (bits)*	*Adders*	*Subs.*	*Mult.*	*Memory (bits)*
Traditional	32	19	20	20	20,480
Metric 1	32	19	0	0	81,920
Metric 2	7	19	0	0	64

$$\overline{J}_k(\alpha_k, \boldsymbol{\sigma}_k) = \sqrt{\frac{T}{2E_s}} \left(H_k \left(Re\{\hat{r}(n)\}, Re\{S(n, \alpha k, \boldsymbol{\sigma}_k)\} \right) + H_k \left(Im\{\hat{r}(n)\}, Im\{S(n, \alpha k, \boldsymbol{\sigma}_k)\} \right) \right) \tag{4-74}$$

where $H_k(\bullet,\bullet)$ is the Hamming distance operation for signals with range $\sqrt{E_s/T}\{1,-1\}$ and can be computed as

$$H_k\left(x(n), y(n)\right) = \sum_{n=M_p k}^{M_p(k+1)-1} \left| x(n) - y(n) \right| \tag{4-75}$$

which counts the number of different samples between $x(n)$ and $y(n)$ in the interval $\left[M_p k, M(k+1)-1\right]$ [Robinson-08].

The hardware resources for the three metrics analyzed previously are summarized in Table 4.4. For example, in Table 4.5 is shown the hardware required considering the IEEE-754 single-precision standard, where each *word* is represented with 32 bits, assuming $M_p = 20$ samples per symbol and $N_s = 16$ states in the trellis.

4.4.3 Error performance of the IQT-Detector

In this Section, the performance analysis of the low-complexity GFSK receiver is described. The performance when the traditional metric is used is given by (2-15), and is described as

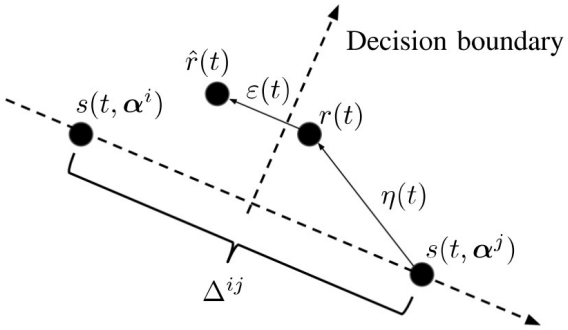

Fig. 4.10 Signal space representation of the received signal $r(t)$ in AWGN channel, the signal $\hat{r}(t)$ and the decision boundary between $s\left(t,\boldsymbol{\alpha}^i\right)$ and $s\left(t,\boldsymbol{\alpha}^j\right)$.

$$P_e \le \frac{2K}{M} Q\left(\sqrt{\frac{d_{min}^2 E_s}{N_0}}\right)$$

where $Q\{\bullet\}$ is the $Q-$ function, $d_{\min}^2$ denotes the minimum squared Euclidean distance (MSED), M is the total number of symbol sequences and K is the number of signal pairs that comply with the MSED.

For the case of metric proposal 1, defined in (4-67) and (4-69), take for instance Fig. 4.10, which shows that $\hat{r}(t) = s\left(t,\boldsymbol{\alpha}^j\right) + \eta(t) + \varepsilon(t)$, where $s\left(t,\boldsymbol{\alpha}^j\right)$ is the complex envelope of a GFSK signal encoded by the sequence of symbols $\boldsymbol{\alpha}^j$, $\varepsilon(t) = \hat{r}(t) - r(t)$ represents the noise obtained by applying the operator $\mathcal{H}\{r(t)\}$, and $\eta(t)$ denotes the Gaussian channel noise. The power of $\varepsilon(t)$ can be approximated by assuming $r(t)$ to be a complex exponential with period T as follows:

$$r(t) = cos\left(\frac{2\pi t}{T}\right) + jsin\left(\frac{2\pi t}{T}\right)$$

therefore,

$$\hat{r}(t) = sign\left(cos\left(\frac{2\pi t}{T}\right)\right) + jsign\left(sin\left(\frac{2\pi t}{T}\right)\right)$$

Hence

TABLE 4.6. ESTIMATION OF d_{min}^2 USING $N=8$.

Metric	M	K	d_{min}^2	Upper bound for P_e
Traditional	256	256	2.0380	Eq. (9)
Proposal 1	256	256	2.0380	Eq. (10)
Proposal 2	256	256	1.992	Eq. (9)

$$Pw^{\varepsilon} = \frac{1}{T}\int_0^T \left|\varepsilon(t)\right|^2 dt = \frac{1}{T}\int_0^T \left|r(t)-\hat{r}(t)\right|^2 dt$$
$$= \frac{1}{T}\int_0^T \left[\left[cos\left(\frac{2\pi t}{T}\right)-sign\left(cos\left(\frac{2\pi t}{T}\right)\right)\right]^2 - \left[sin\left(\frac{2\pi t}{T}\right)-sign\left(sin\left(\frac{2\pi t}{T}\right)\right)\right]^2\right] dt$$
$$= \frac{4}{T}\int_0^{\frac{T}{4}} \left[cos^2\left(\frac{2\pi t}{T}\right)-2cos\left(\frac{2\pi t}{T}\right)sign\left(cos\left(\frac{2\pi t}{T}\right)\right)+sign^2\left(cos\left(\frac{2\pi t}{T}\right)\right)+\right.$$
$$\left. sin^2\left(\frac{2\pi t}{T}\right)-2sin\left(\frac{2\pi t}{T}\right)sign\left(sin\left(\frac{2\pi t}{T}\right)\right)+sign^2\left(sin\left(\frac{2\pi t}{T}\right)\right)\right] dt$$

Considering that $sign\{\bullet\}\in[-1,+1]$ and $\cos^2\{\bullet\}+\sin^2\{\bullet\}=1$, then

$$Pw^{\varepsilon} = \frac{4}{T}\int_0^{\frac{T}{4}} \left[3-2cos\left(\frac{2\pi t}{T}\right)-2sin\left(\frac{2\pi t}{T}\right)\right] dt$$

$$= \frac{4}{T}\left[3t-\frac{Tsin\left(\frac{2\pi t}{T}\right)}{\pi}-\frac{Tcos\left(\frac{2\pi t}{T}\right)}{\pi}\right]_{\sim 0}^{\frac{T}{4}} = 3-\frac{8}{\pi}$$

Therefore, the signal $\varepsilon(t)$ is assumed to be a zero-mean noise uniformly distributed in the interval $\left[\frac{-\epsilon}{2},\frac{\epsilon}{2}\right]$ with variance $\frac{\epsilon^2}{12}$ per real and imaginary components where $\epsilon=\sqrt{12Pw^{\varepsilon}}\approx 2.3329$. Let $f_{\varepsilon}(x)=\frac{1}{\epsilon}$ be the PDF of the signal $\varepsilon(t)$. Hence, the PDF of $\eta(t)+\varepsilon(t)$ is given by the convolution, denoted with the $\circledast$ operator, of both PDFs [Papoulis-91], [Sirca-16]:

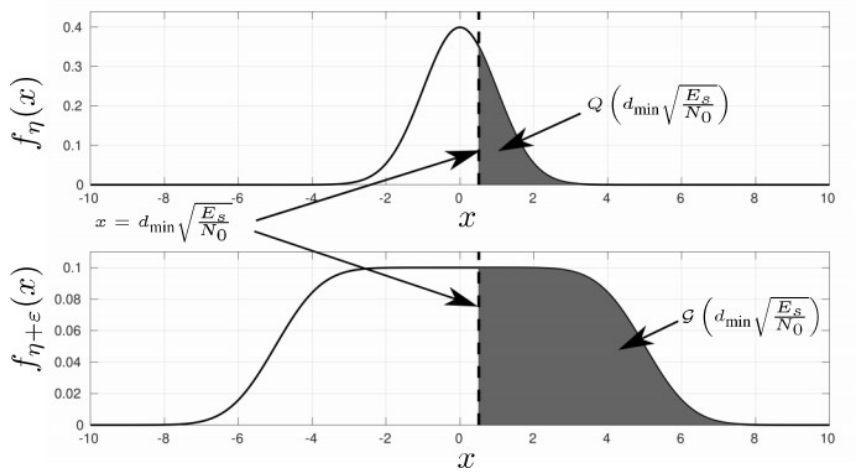

Fig. 4.11 Probability density function $f_\eta(x)$ and $f_{\eta+\varepsilon}(x)$ used to calculate the error probability P_e of the proposal 1.

$$f_{\eta+\varepsilon}(x) = f_\varepsilon(x_\varepsilon) \circledast f_\eta(x) = \int_{-\frac{\epsilon}{2}}^{\frac{\epsilon}{2}} f_\varepsilon(x_\varepsilon) f_\eta(x - x_\varepsilon) = \frac{1}{\epsilon}\frac{1}{\sqrt{2\pi}\sigma}\int_{-\frac{\epsilon}{2}}^{\frac{\epsilon}{2}} \exp\left(-\frac{(x-x_\varepsilon)^2}{\sigma^2}\right)dx_\varepsilon$$

$$= \frac{1}{\epsilon}\frac{1}{\sqrt{\frac{N_0}{2}}}\left[\frac{1}{\sqrt{2\pi}}\int_{-\frac{\epsilon}{2}}^{\infty} exp\left(-\frac{(x-x_\varepsilon)^2}{\sigma^2}\right)dx_\varepsilon - \frac{1}{\sqrt{2\pi}}\int_{\frac{\epsilon}{2}}^{\infty} exp\left(-\frac{(x-x_\varepsilon)^2}{\sigma^2}\right)dx_\varepsilon\right]$$

By using $u = (x - x_\varepsilon)\Big/\left(\frac{N_0}{2}\right)$, the above expression can be rewritten as

$$= \frac{1}{\epsilon}\frac{1}{\sqrt{\frac{N_0}{2}}}\left[\frac{1}{\sqrt{2\pi}}\int_{x-\frac{\epsilon}{2}}^{\infty} exp\left(-\frac{u^2}{2}\right)du - \frac{1}{\sqrt{2\pi}}\int_{x+\frac{\epsilon}{2}}^{\infty} exp\left(-\frac{u^2}{2}\right)du\right]$$

$$= \frac{1}{\epsilon}\left[\frac{1}{\sqrt{2\pi}}\int_{\frac{x-\frac{\epsilon}{2}}{\sqrt{\frac{N_0}{2}}}}^{\infty} exp\left(-\frac{u^2}{2}\right)du - \frac{1}{\sqrt{2\pi}}\int_{\frac{x+\frac{\epsilon}{2}}{\sqrt{\frac{N_0}{2}}}}^{\infty} exp\left(-\frac{u^2}{2}\right)du\right]$$

$$f_{\eta+\varepsilon}(x) = \frac{1}{\epsilon}\left[Q\left(\frac{x-\frac{\epsilon}{2}}{\sqrt{\frac{N_0}{2}}}\right) - Q\left(\frac{x+\frac{\epsilon}{2}}{\sqrt{\frac{N_0}{2}}}\right)\right]$$

that represents the PDF of the addition of two random variables. Both PDFs $f_\eta(x)$ and $f_{\eta+\varepsilon}(x)$ are shown in Fig. 4.11.

Then, the error probability for metric proposal 1 is given by $P_e \leq \frac{2K}{M} \mathcal{G}\left(\sqrt{\frac{d_{min}^2 E_s}{N_0}}\right)$ (4-76)

where $\mathcal{G}(x)$ is the tail probability of $f_{\eta+\varepsilon}(x)$ and is defined as

$$\mathcal{G}(x) = \int_x^{\infty} f_{\eta+\varepsilon}(\xi) d\xi$$

In the case of metric proposal 2, its performance is determined according to (2-15), where the MSED is computed by applying the transform operator, described in (4-68), to the received and reference signals.

Note that P_e represents the sequence error probability rather than the symbol error probability. However, symbol error probability is often approximated by P_e for high values of E_s/N_0 since it is more probable that errors occur in a sequence with only one erroneous symbol [Anderson-86].

4.4.4 Theoretical and simulated performance results for IQT-detector

This section presents the theoretical and simulated results for the performance of the proposed receiver using the metric proposal 1 and 2. The parameters used to compute the upper bound of the error probability P_e for the presented metrics are shown in Table 4.6. The value of the MSED was estimated using N from 4 to 12 symbols. The results show variations of less than 10^{-9} for each metric. The signal space dimension, $M = 2^N$, and the number of signal pairs with the same minimum distance, K, are shown for the case of $N = 8$. The error performance for proposals 2 and 1 is shown in Fig. 4.13.

The simulation parameters of the GFSK communication system are set as follows: a pulse $g(t)$ with $L = 3$ symbol periods and $BT = 0.5$; the modulation index is $\lambda = 0.5$ and the VA has a traceback of 20 symbol periods. As a figure of merit, it is considered the E_s/N_0 required to achieve a BER of 10^{-3}; this value is established in the Bluetooth core specification [S.I.G. Bluetooth-19].

Fig. 4.12 depicts the simulated BER performance of the GFSK communication system using the proposed metrics as well as the performance of the system with the traditional metric, which

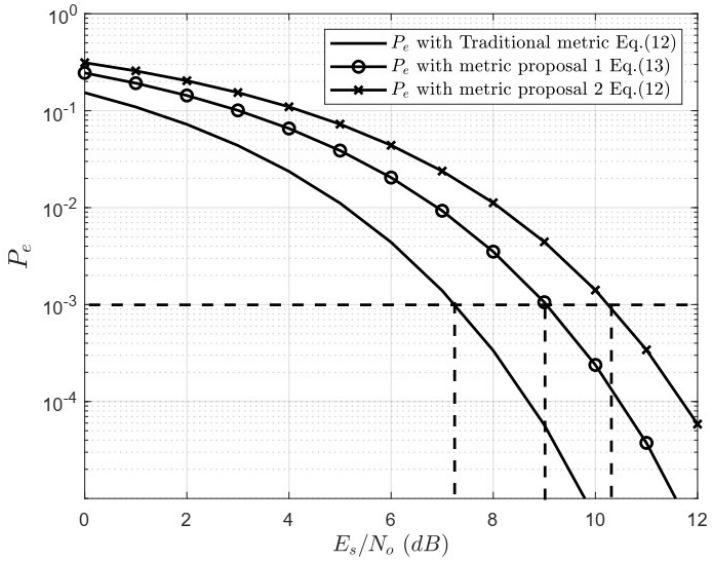

Fig. 4.13 Error performance of GFSK VA using the traditional and proposed metrics.

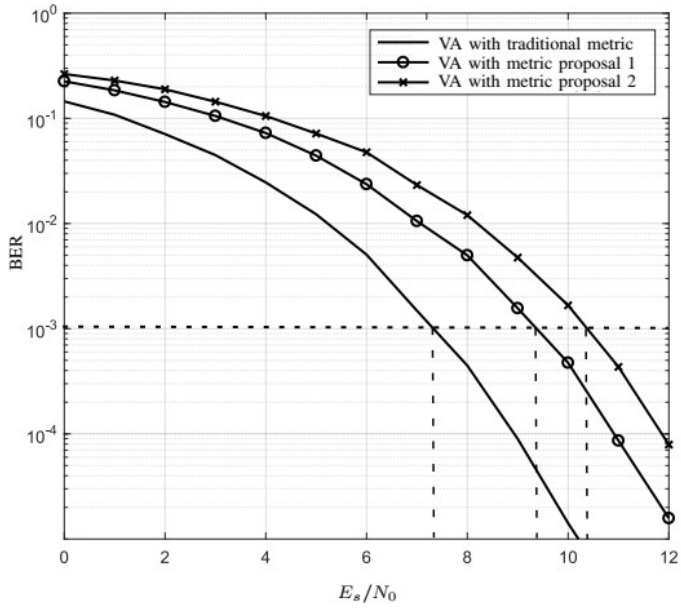

Fig. 4.12 BER performance of GFSK VA using the traditional and the proposed metrics.

matches the MLSE performance obtained from the results presented in [Anderson-86], by considering $3RC$, $\lambda = 0.5$ and $d^2_{\min}$. It can be observed that the receiver system with the proposed metrics 1 and 2 exhibits a loss of $2\ dB$ and $3\ dB$, respectively, when compared with the MLSE performance (traditional metric). However, if the computational complexity and the hardware

resources presented in in Table 4.4 are considered, it is very clear that the proposed metrics implies a significant reduction in hardware resources, since no subtractors and multipliers are required in both proposals.

Furthermore, metric 2 is the best scheme in terms of required memory bits. In addition, it is important to mention that the Bluetooth core specification requires a sensitivity level of $-70\ dBm$ for a BER of 0.1%, which is achieved with $E_s/N_0 = 21\ dB$, In this respect, and taking as a reference this E_s/N_0 level, the proposals 1 and 2 show a gain, with respect to the specification requirements, equal to $21-9.5=11.5\ dB$ and $21-10.5=10.5\ dB$, respectively.

4.5. Conclusions

This Chapter describes a GFSK demodulator with a linear structure (LPIE), whose robustness allows for operation with both exact and linear modulators. Likewise, simulations results for the two implementations of the LPIE in an AWGN channel are shown and compared with a maximum likelihood receiver (implemented with the Viterbi algorithm) and a BPSK system. These results show that the LPIE achieves near-optimal performance in the AWGN channel. Furthermore, it can be seen that the performance of the two implementations of LPIE meets the specification for the BLE standard.

Likewise, a GFSK receiver which transforms the I and Q components of the received baseband signal has been described. The transformation allows representing the components of the baseband signal using only two values (+1 and -1) instead of a set of infinities values. Thus, it is possible to reduce the hardware resources required for the detection process. The error performance for the traditional metric and the proposals is determined by employing the expression derived in Chapter 2. In the case of metric 1, the distortion introduced by the transform operator in the received signal is considered.

The theoretical BER performance for the two proposals was presented and compared with the simulated results. Since both performances match very well, the theoretical analysis is corroborated.

5. Space-Time Diversity Techniques for GFSK Signaling

In the wireless communication environment, the transmitted signal travels through different paths and suffers attenuation, delay, and phase shift. Consequently, the signal in the receiver is a superposition of randomly attenuated, delayed, and phase-shifted copies of the transmitted signal. The communication channel with these characteristics is called fading channel and causes significant performance degradation of the communication system.

Diversity is a set of techniques employed to improve the performance of communication systems under fading channels. The basic idea behind diversity techniques is the transmission of the signal over different uncorrelated fading channels in a way that while some replicas of the transmitted signal suffer deep fading, others may not [Goldsmith-05]. At the receiver, the signals are combined to obtain a signal in which the effects of the channel are reduced or mitigated. The most common diversity techniques employed in communication systems are time, space, and frequency diversity.

Under this context, a description of the fading channel and its characteristics, the diversity techniques used to overcome issues of fading, and some relevant studies on CPM signaling under fading channel are presented.

5.1. Multipath propagation channel model for GFSK signaling

In wireless communication systems, the signal present at the receiver is a composite signal that consists of several replicas of the transmitted signal. Since each replica travels in a different path, the attenuation, time delay, and phase shift are also different. A communication channel that introduces these effects is called fading channel and is characterized by the following parameters [Xiong-06], [Ha-01]:

a) Delay spread is the maximum propagation difference time between two signal replicas at the receiver.

b) Coherence bandwidth (B_c) is the range of frequencies in which all the signal spectral components experience the same attenuation and phase shift.
c) Coherence time is the time duration in which the impulse response of the channel remains without changes.

According to the above parameters, the fading channel can be classified as follows:

a) Flat and frequency-selective fading. If the bandwidth of the signal is smaller than the coherence bandwidth, the different replicas will undergo the same fading effects. Thus, the fading is considered frequency non-selective or "flat." On the contrary, the different frequency components of the signal will experience different levels of fading.
b) Slow and fast fading. In a slow fading channel, the coherent time is larger than the symbol time duration. In fast fading, the impulse response of the channel changes faster than the symbol time duration.

In order to mitigate the effects of the fading channel, diversity techniques are employed. The basis of diversity techniques is to provide the receiver with uncorrelated replicas of the signal using independent paths. As a result, the probabilities of different replicas having the same degree of attenuation, time delay or phase-shifting are low. In what follows, the different methods to achieve diversity are presented.

One method is time diversity, which consists of the transmission of the same information at different time intervals. Since it is essential to have uncorrelated replicas, the transmission time interval must be larger than the coherence time. The main problem in this approach is the reduction of the transmission rate. The second approach is the space diversity technique in which two or more antennas are employed in the transmitter and/or the receiver. As a result, there are different uncorrelated paths for the transmitted signal. Another common diversity method is frequency diversity. It uses different band frequencies; therefore, the transmitted signals will experiment with different levels of fading according to the frequency band. Orthogonal frequency division multiplexing (OFDM) is the most representative frequency diversity technique. In this approach, the separation between bands should be at least the coherence bandwidth. The main disadvantage of this technique is a bandwidth increase.

The replicas are combined at the receiver by using different methods to obtain an improved signal. The selection combing method compares the replica signals and selects the strongest one.

TABLE 5.1. THE ENCODER OUTPUT FOR ALAMOUTI TECHNIQUE

time	Antenna 0	Antenna 1
t	$s_0(t)$	$s_1(t)$
$t+T$	$-s_1^*(t)$	$s_0^*(t)$

In the switched combining approach, it is selected the replica signal with a signal to noise ratio (SNR) above a certain level (threshold). If the SNR of this signal falls under the threshold SNR level, the receiver switches to another signal that is above the specified threshold. In the maximal ratio combining scheme (MRC), the resulting signal is a weighted sum of all the signal replicas; the weights are selected according to the characteristics of the channel. Thus, it implies the need to estimate the channel at the receiver. The equal gain combining technique (EGC) is very similar to MRC, but in this case, the signal replicas are not weighted; hence, a knowledge of the channel is no needed.

Concerning Bluetooth low energy (BLE) devices, which employ a digital CPM modulation scheme, the channel can be modeled as a flat-fading channel due to its bandwidth [S.I.G. Bluetooth-19] of 2MHz is narrower than the coherence bandwidth of a typical wireless channel [Lin-15], [Votis-16] for this kind of applications. In order to combat the impact of fading channel issues, BLE uses frequency hopping [Watteyne-10].

5.2. An implementation of the Alamouti technique

The Alamouti technique [Alamouti-98] is a space-time diversity technique. It can employ two transmitting antennas, and one or two receive antennas. The system consists of an encoder at the transmitter, and a symbol combining scheme with a maximum likelihood sequence estimator (MLSE) at the receiver, as is shown in Fig. 5.1.

The channel fading from the transmit antenna 0 and antenna 1 to the receiver antenna can

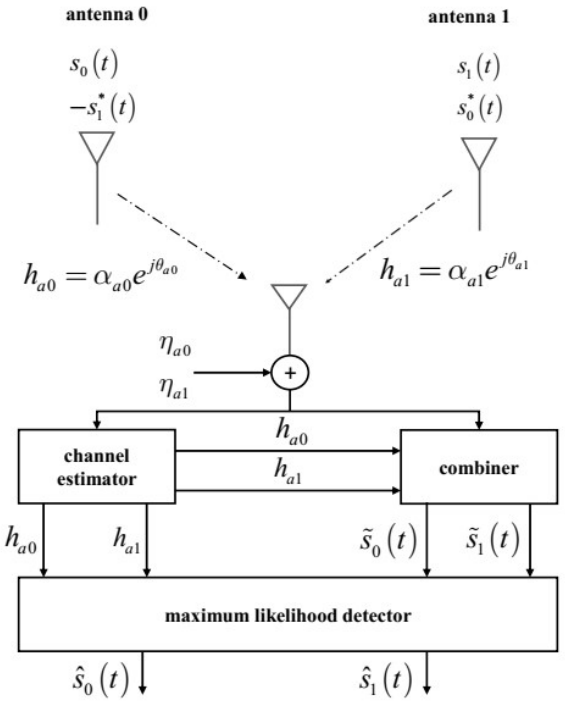

Fig. 5.1 Baseband block diagram of the diversity scheme proposed by Alamouti.

be modeled by the following complex Gaussian random variables:

$$\begin{aligned} h_{a0} &= \alpha_{a0} e^{(j\theta_{a0})} \\ h_{a1} &= \alpha_{a1} e^{(j\theta_{a1})} \end{aligned} \tag{5-1}$$

where α_a is the attenuation factor and follows Rayleigh distribution, and θ_a represents the phase shift and is uniformly distributed over $(0, 2\pi)$.

The encoder generates the transmission sequence in a way that, in a time slot, T, the symbol transmitted from antenna 0 is s_0 and s_1 is transmitted from antenna 1. In the next symbol period, $-s_1^*$ is transmitted from antenna 0 and s_0^*, where the * denotes the complex conjugate operation. In Table 5.1, the output encoder sequence is shown. It is important to mention that it is assumed that the channel is constant at least two consecutive symbol periods.

The received symbols at two consecutive symbol time slots are defined as

$$\begin{aligned} r_{a0} &= h_{a0} s_0 + h_{a1} s_1 + \eta_{a0} \\ r_{a1} &= -h_{a0} s_1^* + h_{a1} s_0^* + \eta_{a1} \end{aligned} \tag{5-2}$$

where η_{a0} represents the additive white Gaussian noise (AWGN), modeled by random variables with zero-mean, variance $\sigma^2 = N_0/2$ per real and imaginary components, and $N_0/2$ denotes the power spectral density of the AWGN.

The combining scheme processes the signals r_{a0} and r_{a1} and provides the following

$$\begin{aligned} \tilde{s}_0 &= h_{a0}^* r_{a0} + h_{a1} r_{a1}^* \\ \tilde{s}_1 &= h_{a1}^* r_{a0} - h_{a0} r_{a1}^* \end{aligned} \tag{5-3}$$

Substituting (5-1) and (5-2) in (5-3), thus

$$\begin{aligned} \tilde{s}_0 &= (\alpha_{a0}^2 + \alpha_{a1}^2) s_0 + h_{a0}^* \eta_{a0} + h_{a1} \eta_{a1}^* \\ \tilde{s}_1 &= (\alpha_{a0}^2 + \alpha_{a1}^2) s_0 - h_{a0} \eta_{a1}^* + h_{a1}^* \eta_{a0} \end{aligned} \tag{5-4}$$

An estimate, $\hat{s}_i$, of the symbol s_i is obtained from the maximum likelihood detector by considering the Euclidean distance as follows: s_i is choose if and only if

$$d^2(\tilde{s}_0, s_i) \leq d^2(\tilde{s}_0, s_k) \qquad \forall i \neq k \tag{5-5}$$

where d^2 is the squared Euclidean distance.

The importance of the Alamouti's technique lies in the fact that it achieves the same diversity order that the classical maximal-ratio receiver combining with one transmit and two receive antennas without bandwidth incremental and feedback from the receiver to the transmitter.

Diversity techniques have been widely studied and applied to overcome fading impairments for linear modulations scheme but not for nonlinear modulations, e.g., CPM, due mainly to the orthogonality and phase continuity requirements [Aygölü-04], [Xiaoxia-01]. Under this scenario, in [Xian-08] is proposed an orthogonal space-time (ST) for CPM signaling with a modulation index of 0.5 based on the Laurent decomposition and the space-time diversity technique proposed by Alamouti. The authors of [Xian-08] claim that the main feature of their proposal is a low complexity implementation while maintaining diversity performance.

At the transmitter, the Laurent decomposition [Laurent-86] is employed to approximate the CPM signal with a linear superposition of weighted PAM pulses. It was demonstrated that among all PAM pulses, only one of them concentrates almost all the energy, so it is named the "main pulse" and is represented as $C_0(t)$. In this way, the pulse $C_0(t)$ can be used to represent the linear approximation of the CPM signal with a significant complexity reduction in the receiver and without losing performance.

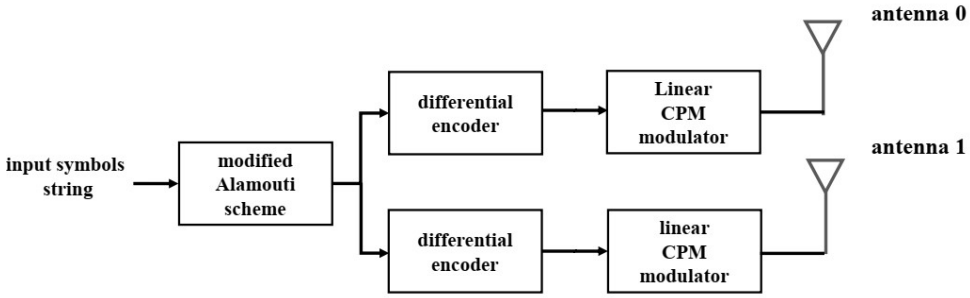

Fig. 5.2 Baseband block diagram of the transmitted proposed in [Xian-08] with the modified Alamouti diversity scheme.

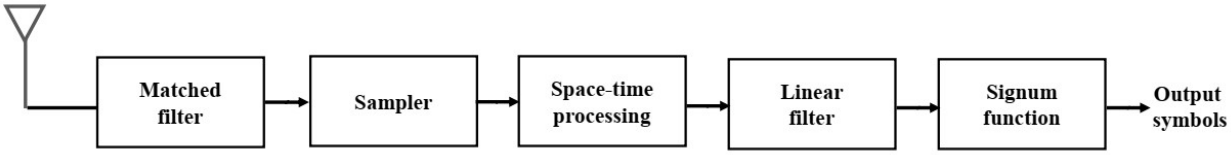

Fig. 5.3 Block diagram of the receiver proposed in [Xian-08].

The diversity technique employed is presented in [Alamouti-88] with a modification that is given in Table 2. This modification allows having one antenna with the same signal as in the case of a single antenna transmission. The block diagram of the system is depicted in Fig. 5.2. The received signal is passed through a matched filter with an impulse response $C_0(-t)$ and sampled each symbol period, the space-time decoding algorithm described in [Alamouti-88] is applied, and the estimated symbols are determined by using the signum function.

A crucial aspect to be considered in this proposal is the fact that the signal at the output of the space-time decoder is equivalent to filter the signal with a filter that can be designed with a structure that allows a low complexity implementation. Fig. 5.3 depicts the block diagram of the receiver. Regarding performance, the proposal shows a loss of $2\ dB$ when compared to BPSK at a BER of 10^{-4}.

In [Shi-10] the authors present a simplified detection algorithm for a full-response CPM system that employs ST diversity for L_T transmitting and L_r receiving antennas. The proposal is based on the extension of the well-known Laurent decomposition for M -ary CPM signaling. By using this decomposition, the CPM signal is represented by the linear superposition of $M-1$

components, which allows simplifying the implementation of the receiver. The structure of the transmitter is shown in Fig. 5.5.

At the receiver, the number of matches filters employed to perform the maximum likelihood metric computation can be reduced to $M-1$ due to the linear approximation of the transmitted CPM signal. In contrast, the optimal maximum likelihood sequence detector (MLSD) implemented with the Viterbi algorithm requires $Q_A\left(2M_A\right)^{LT}$ matched filters, where Q_A denotes the number of states present in the trellis diagram of the CPM signaling. From the simulation results, it can be observed that performance degradation of the proposal is about 0.25 dB at a BER of 10^{-3} when compared with the MLSD. The structure of the receiver is shown in Fig. 5.4.

Likewise, in [Zhao-05] the authors proposed a reduced-complexity receiver for ST CPM signaling, which employs, as in the previous cases, the Laurent decomposition to obtain a linear approximation of the CPM signal. Since this approximation of the signal uses only the pulse with the most energy, at the receiver, only one match filter is used.

The authors expose the specific case of minimum shift keying (MSK), which is a CPM signaling with a full response. Due that the linear approximation of the MSK signaling introduces inter-symbol interference (ISI), there is an increase in complexity implementation of the receiver. Thus, they implement an equalizer that eliminates the ISI, and consequently, a reduction in complexity implementation.

Despite using linear detectors, the complexity of the maximum likelihood detector (MLD) when diversity techniques are used together with CPM schemes are usually high. In this sense, the proposed receiver achieves an additional reduction in the complexity employing the sphere detection method. This method is suboptimum but simpler than MLD.

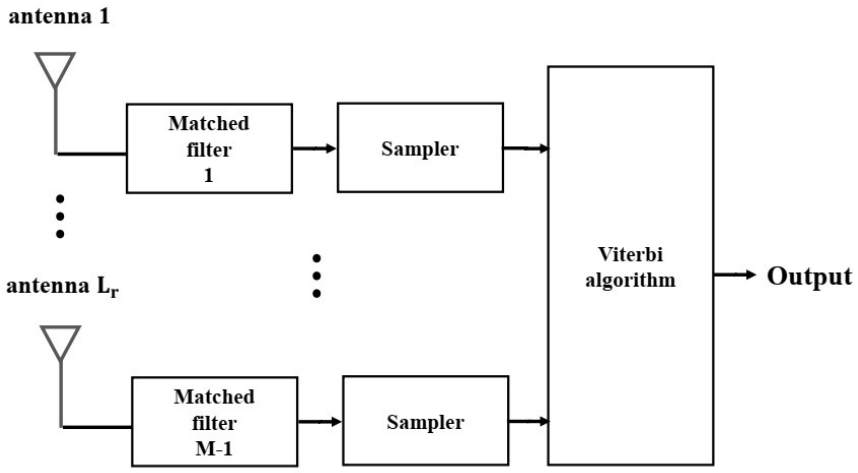

Fig. 5.4 Block diagram of the receiver proposed in [Shi-10].

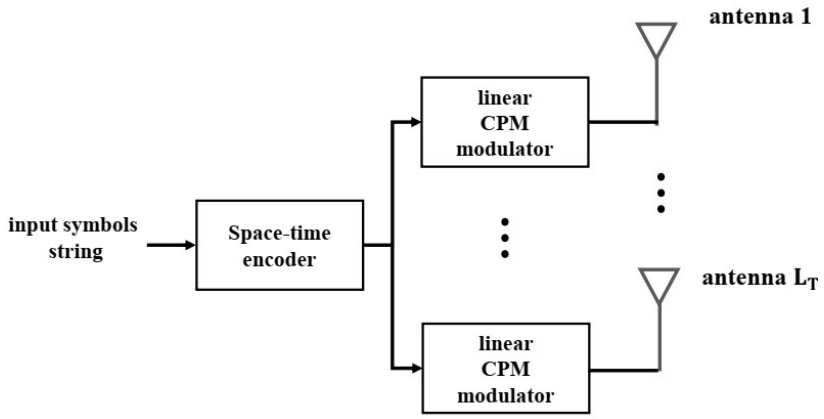

Fig. 5.5 Baseband block diagram of the transmitted proposed in [Shi-10].

5.3. Conclusions

Fading channel and diversity techniques used to overcome its impairments have been described. These techniques have been used mainly for linear modulation schemes, and its implementation for nonlinear modulation schemes is limited due to orthogonality requirements and phase continuity constrain for CPM signaling.

Research on space-time diversity technique for CPM signaling, based in Laurent's approximation, is reviewed. The proposals described in [Xian-08], [Shi-10] and [Zhao-05] give

different approaches to address the complexity problem in MIMO systems.

General Conclusions

In this doctoral dissertation, the design of two novels GFSK detectors for IoT BLE devices have been presented. The main features of the proposals are a low complexity implementation and a near-optimal performance under AWGN channel, which comply with the Bluetooth requirements in terms of BER.

In Chapter 1 was given a mathematical description of the GFSK signal and the different alternatives for its implementation. In Chapter 2, the error probability for different CPM signaling has been presented. It is shown the Euclidean distance is the parameter that determines the error performance. An important tool employed to determine this parameter is the phase tree. Since in the computation of the error performance, the phases trajectories of the signal increase according to the number of symbol time intervals, the phase tree becomes unrealizable. However, an upper bound for the error probability can be determined if only pairs of sequences with the minimum Euclidean distance are considered. Also, it was seen that the Euclidean distance is a function of the modulation index.

In Chapter 3 were presented two methods to approximate the GFSK signal linearly. One approximation is based on the proposal given in [Laurent-86] and represents the signal as a linear superposition of a finite number of amplitude-modulated pulses. It was demonstrated that the pulse that contains most of the signal energy could be used to approximate the GFSK signal. In the second approach, described in [Liang-97], the linear model of the signal is obtained by oversampling the original GFSK signal by two times in one symbol period and then, neglecting the nonlinear components of this oversampled signal.

In Chapter 4, two novel low-complexity GFSK detectors that can be used in BLE for IoT wireless communications devices were proposed. The first proposal, called LPIE, is based in the linear approximation detailed in [Liang-97]. This proposal has the following attractive features: its linear structure and robustness allow for operation with both exact and linear modulators achieving near-optimal performance in the AWGN channel. The theoretical error probability analysis is provided for two different implementations for the AWGN channel. A method for selecting the demodulator parameters was developed based on the minimization of error probability. Simulation results corroborate that the LPIE achieves near-optimal performance in the AWGN channel when

it is compared with the GFSK Viterbi demodulator. Likewise, the theoretical formulas presented for error probability match the simulation results. In the second proposal, the reduction in complexity was achieved through a transformation of the received signal. This processing allows the use of two simplified metrics in the implementation of the VA. The proposed metrics attain a reduction of computational complexity and hardware resources. The theoretical and simulation results show that the receiver using the metric proposal 2 has the most large-scale improvement in hardware resources required for its implementation in comparison with the traditional implementation used by VA. Specifically, there are no adders, subtractors, and multipliers involved.

Finally, in Chapter 5, research on space-time diversity techniques for GFSK signaling was revised. To obtain a reduction of complexity, the proposals presented in [Xiang-08], [Shi-10], and [Zhao-05] employ the Laurent decomposition to obtain a linear approximation of the signal. Furthermore, approaches as the modification of the Alamouti technique, reduction of the number of matched filters at the receiver and, the use of an equalizer to eliminate the ISI at the received signal are used. These studies are a reference to consider for our future work regarding the reduction complexity techniques applied to GFSK systems under fading channels.

Conclusiones Generales

En esta tesis doctoral se presentó el diseño de dos novedosos detectores GFSK para dispositivos IoT BLE. Las principales características de las propuestas son una implementación de baja complejidad y un rendimiento subóptimo bajo el canal AWGN, que cumple con los requisitos de Bluetooth en términos de BER.

En el Capítulo 1 se dio una descripción matemática de la señal GFSK y las diferentes alternativas para su implementación. En el Capítulo 2, se ha determinado la probabilidad de error para diferentes señales CPM. Se muestra que el desempeño de los sistemas de modulación está determinado por la distancia Euclidiana entre las señales. El árbol de fases es una herramienta de suma importancia para determinar este parámetro. Dado que, en el cálculo del desempeño, las trayectorias de las fases de la señal aumentan de acuerdo con el número de periodos de símbolo considerados, el árbol de fases se vuelve irrealizable. Sin embargo, si solo se consideran los pares de secuencias con la distancia Euclidiana mínima, se puede encontrar una cota superior para la probabilidad de error. Adicionalmente, se ha observado que la distancia Euclidiana depende del índice de modulación.

En el Capítulo 3 se presentaron dos métodos para realizar una aproximación lineal de la señal GFSK l. Una de ellas se basa en la propuesta presentada en [Laurent-86] y aproxima la señal mediante la superposición lineal de un número finito de pulsos modulados en amplitud. Se demostró que el pulso que contiene la mayor parte de la energía de la señal puede usarse para representar la señal GFSK. En el segundo enfoque, descrito en [Liang-97], el modelo lineal de la señal se obtiene sobremuestreando la señal GFSK original dos veces en un período de símbolo y descartando los componentes no lineales de esta señal sobremuestreada.

En el Capítulo 4, se propusieron dos nuevos detectores GFSK de baja complejidad que se pueden emplear en dispositivos de comunicaciones inalámbricas de IoT BLE. La primera propuesta, nombrada LPIE, se basa en la aproximación lineal descrita en [Liang-97]. Esta propuesta tiene las siguientes características atractivas: su estructura lineal y robustez permiten operar con moduladores exactos y lineales, logrando un desempeño subóptimo en el canal AWGN. El análisis de probabilidad de error teórico se proporciona para dos implementaciones diferentes bajo el modelo de canal AWGN. Se desarrolló un método para seleccionar los parámetros del

demodulador basado en la minimización de la probabilidad de error. Los resultados de la simulación corroboran que el demodulador LPIE presenta un rendimiento muy cercano al óptimo en el canal AWGN cuando se compara con el demodulador GFSK que emplea el algoritmo de Viterbi. Las fórmulas teóricas que se derivaron para la probabilidad de error coinciden con los resultados de la simulación. En la segunda propuesta, la reducción de la complejidad se logró mediante la transformación de la señal recibida. Esto permite el uso de dos métricas simplificadas en la implementación del algoritmo de Viterbi. Las métricas propuestas logran una reducción en los recursos de hardware y la complejidad computacional. Los resultados teóricos y de simulación muestran que el receptor que utiliza la métrica propuesta 2 presenta una reducción en los recursos de hardware requeridos para su implementación en comparación con la implementación que emplea el algoritmo de Viterbi dado que no utilizan sumadores, restadores ni multiplicadores,

Finalmente, en el Capítulo 5, se hizo una revisión de los trabajos de investigación sobre técnicas de diversidad espacio-temporal para la modulación GFSK. Con el fin de obtener una reducción en la complejidad, las propuestas presentadas en [Xian-08], [Shi-10] y [Zhao-05] utiliza la descomposición de Laurent para obtener una aproximación lineal de la señal. Además, se utilizan estrategias como la modificación de la técnica Alamouti, la reducción del número de filtros acoplados en el receptor y el uso de ecualizadores para eliminar la interferencia intersimbolica en la señal recibida. Estos estudios son una referencia para considerar en nuestro el trabajo futuro con respecto a las técnicas de reducción de la complejidad aplicadas a los sistemas GFSK bajo canales con desvanecimiento.

Appendix

A. LIST OF INTERNAL RESEARCH REPORTS

1) J. M. Valencia and O. H. Longoria-Gandara, "An introduction to Bluetooth low energy," Internal Report *PhDEngScITESO-14-09-R*, ITESO, Tlaquepaque, Mexico, Dec. 2014.

2) J. M. Valencia, R. Aldana-Lopez, and O. H. Longoria-Gandara, "General aspects of continuous phase modulation signaling," Internal Report *PhDEngScITESO-16-15-R*, ITESO, Tlaquepaque, Mexico, Nov. 2016.

3) J. M. Valencia, R. Aldana-Lopez, and O. H. Longoria-Gandara, "An overview of techniques for complexity reduction of CPM systems," Internal Report *PhDEngScITESO-16-23-R*, ITESO, Tlaquepaque, Mexico, Dec. 2016.

4) J. M. Valencia, R. Aldana-Lopez, and O. H. Longoria-Gandara, "Linear representation of continuous phase modulation signaling," Internal Report *PhDEngScITESO-17-30-R*, ITESO, Tlaquepaque, Mexico, Aug. 2017.

5) J. M. Valencia, R. Aldana-Lopez, and O. H. Longoria-Gandara, "Linear approximation of continuous phase modulation signaling using Laurent decomposition," Internal Report *PhDEngScITESO-17-52-R*, ITESO, Tlaquepaque, Mexico, Dec. 2017.

6) J. M. Valencia, R. Aldana-Lopez, and O. H. Longoria-Gandara, "Comparison between CPM signaling and it's Laurent's linear approximation," Internal Report *PhDEngScITESO-17-56-R*, ITESO, Tlaquepaque, Mexico, Dec. 2017.

7) J. M. Valencia, R. Aldana-Lopez, and O. H. Longoria-Gandara, "A digital linear GFSK demodulator based on pseudo-inverse estimation," Internal Report *PhDEngScITESO-18-41-R*, ITESO, Tlaquepaque, Mexico, Dec 2018.

8) J. M. Valencia, R. Aldana-Lopez, and O. H. Longoria-Gandara, "Error performance of linear GFSK demodulator based on pseudo-inverse estimation (LPIE)," Internal Report *PhDEngScITESO-18-45-R*, ITESO, Tlaquepaque, Mexico, Dec 2018.

9) J. M. Valencia, R. Aldana-Lopez, and O. H. Longoria-Gandara, "Low-complexity maximum-likelihood GFSK detector," Internal Report *PhDEngScITESO-18-57-R*, ITESO, Tlaquepaque, Mexico, Dec 2018.

10) J. M. Valencia, R. Aldana-Lopez, and O. H. Longoria-Gandara, "Alternative metrics for Viterbi detector of GFSK signals," Internal Report *PhDEngScITESO-19-22-R*, ITESO, Tlaquepaque, Mexico, Dec 2019.

11) J. M. Valencia, R. Aldana-Lopez, and O. H. Longoria-Gandara, "The importance of the Euclidean distance in the error performance analysis," Internal Report *PhDEngScITESO-19-32-R*, ITESO, Tlaquepaque, Mexico, Dec 2019.

12) J. M. Valencia, R. Aldana-Lopez, and O. H. Longoria-Gandara, “Performance analysis of a low-complexity maximum-likelihood GFSK detector,” Internal Report *PhDEngScITESO-20-01-R*, ITESO, Tlaquepaque, Mexico, Jan. 2020.

13) J. M. Valencia, R. Aldana-Lopez, and O. H. Longoria-Gandara, “An introduction to space-time diversity techniques for CPM signaling,” Internal Report *PhDEngScITESO-20-04-R*, ITESO, Tlaquepaque, Mexico, Apr. 2020.

B. LIST OF PUBLICATIONS

B.1 Conference papers.

1) J. Valencia-Velasco, R. Aldana-Lopez and O. Longoria-Gandara, "Alternative Viterbi Detection Metrics for GFSK Receivers: A Hardware Reduction Approach," *2018 IEEE 10th Latin-American Conference on Communications (LATINCOM)*, Guadalajara, 2018, pp.1-5, doi: 10.1109/LATINCOM.2018.8613225

B.2 Journal papers.

1) R. Aldana-Lopez, J. Valencia-Velasco, O. Longoria-Gandara and L. Pizano Escalante, "Digital linear GFSK demodulator for IoT devices," in *IET Communications*, vol. 12, no. 16, pp. 1997-2004, November 2018, doi: 10.1049/iet-com.2018.5040.
2) J. Valencia-Velasco, O. Longoria-Gandara, R. Aldana-Lopez and L. Pizano-Escalante, "Low-Complexity Maximum-Likelihood Detector for IoT BLE Devices," in *IEEE Internet of Things Journal*, vol. 7, no. 6, pp. 4737-4745, June 2020, doi: 10.1109/JIOT.2020.2966988.

Bibliography

[Alamouti-98] S. M. Alamouti, "A simple transmit diversity technique for wireless communications*," IEEE Journal on Selected Areas in Communications*, vol. 16, no. 8, pp. 1451–1458, Oct. 1998.

[Aldana-Lopez-18] R. Aldana-Lopez, J. M. Valencia-Velasco, O. H. Longoria-Gandara, and L. Pizano-Escalante "A Digital Linear GFSK Demodulator for IoT Devices*," IET Communications Journal*, vol. 12, pp. 1997–2004, Sept. 2018.

[Al-Dhahir-98] N. Al-Dhahir and G. Saulnier, "A high-performance reduced-complexity GMSK demodulator," *IEEE Transactions on Communications*, vol. 46, no. 11, pp. 1409–1412, Nov. 1998.

[Anderson-86] J. B. Anderson, T. Aulin, and C.-E. Sundberg, *Digital Phase Modulation*. New York, USA: Springer Science & Business Media, 1986.

[Aulin-81a] T. Aulin and C. Sundberg, "Continuous Phase Modulation - Part I: Full Response Signaling," *IEEE Transactions on Communications*, vol. 29, no. 3, pp. 196–209, Mar. 1981.

[Aulin-81b] T. Aulin, N. Rydbeck, and C. E. Sundberg, "Continuous phase modulation - part II: partial response signaling," *IEEE Transactions on Communications*, vol. 29, no. 3, pp. 210–225, Mar. 1981.

[Aygölü-04] Ü. Aygölü and M. E. Çelebi, "Space-time MSK Codes for Quasi-Static Fading Channels," *AEU-International Journal of Electronics and Communications*, vol. 58, no. 4, pp. 268–273, Jan. 2004.

[Barnickel-13] J. Barnickel, J. Wang, and U. Meye, "Implementing an Attack on Bluetooth 2.1+ Secure Simple Pairing in Passkey Entry Mode," in *IEEE 11th International Conference on Trust, Security and Privacy in Computing and Communications*, Salamanca, Spain, Sep. 2013, pp. 17–24.

[Byrd-00] Byrd, R.H., Gilbert, J.C., Nocedal, J.: '*A trust region method based on interior point techniques for nonlinear programming*', Math. Program., 2000, 89, (1), pp. 149–185.

[Broekhuis-11] D. Broekhuis, "Feasibility Study of Eavesdropping Using GNU Radio," in *15th Twente Student Conference on IT*, Enschede, The Netherland, Jun. 2011.

[Brown-09] C. Brown and P. J. Vigneron, "Complexity reduction for continuous phase modulation using basis functions," in *2009 IEEE Military Communications Conference*, Boston, MA, USA, Oct. 2009, pp. 1–7.

[Cariolaro-10] G. Cariolaro, "A system-theory approach to decompose CPM signals into PAM waveforms," *IEEE Transactions on Communications*, vol. 58, no. 1, pp. 200–210, Jan. 2010.

[Chen-14] S. Chen, H. Xu, D. Liu, B. Hu, and H. Wang, "A Vision of IoT: Applications, Challenges, and Opportunities with China Perspective," *IEEE Internet of Things Journal*, vol. 1, no. 4, pp. 349–359, Aug. 2014.

[Collota-18] M. Collotta, G. Pau, T. Talty, and O. K. Tonguz, "Bluetooth 5: A Concrete Step Forward toward the IoT," *IEEE Communications Magazine*, vol. 56, no. 7, pp. 125–131, Jul. 2018.

[Forney-73] G. D. Forney, "The Viterbi algorithm," *Proceedings of the IEEE*, vol. 61, no. 3, pp. 268–278, Mar. 1973.

[Gerez-07] Sabih H. Gerez. (2007). Implementation of Digital Signal Processing: Some Background on GFSK Modulation [Online]. Available: http://wwwhome.ewi.utwente.nl/~gerezsh/sendfile/sendfile.php/gfskintro.pdf?sendfile=gfsk-intro.pdf.

[Goldsmith-05] A. Goldsmith, *Wireless Communications*. Stanford, CA: Cambridge University Press, 2005.

[Gomez-12] C. Gomez, J. Oller, and J. Paradells, "Overview and Evaluation of Bluetooth Low Energy: An Emerging Low-Power Wireless Technology," *Sensors*, vol. 12, no. 9, pp. 11734–11753, Aug. 2012.

[Gupta-13] N. Gupta, *Inside Bluetooth Low Energy*. USA: Artech House, 2013.

[Ha-01] Tri T. Ha, *Theory and Design of Digital Communication Systems*. Cambridge, UK: Cambridge University Press, 2001.

[Haartsen-02] J.C. Haartsen, "Bluetooth radio system," *IEEE Personal Communications*, vol. 7, pp. 28–36, Aug. 2002.

[Hassan-14] D. Hassan, U. Aickelin, and C. Wagner, "Comparison of Distance metrics for hierarchical data in medical databases," in *2014 International Joint Conference on Neural Networks (IJCNN)*, 2014, pp. 3636–3643.

[Heydon-13] R. Heydon, *Bluetooth Low Energy the Developer's Hand book*. Crawfordsville, IN: Prentice Hall, 2013.

[Huang-03] X. Huang and Y. Li, "The PAM decomposition of CPM signals with integer modulation index," *IEEE Transactions on Communications*, vol. 51, pp. 543–546, Apr. 2003.

[Ibrahim-12] M.E.A. Ibrahim, H.E. Ahmed, and A. Zekry, "Performance evaluation of digital modulation techniques used in Bluetooth physical/radio layer," in *2012 Seventh International Conference on Computer Engineering & Systems (ICCES)*, Cairo, Egypt, Nov. 2012.

[Jung-92] P. Jung and P. W. Baier, "On the representation of CPM signals by linear superposition of impulses in the bandpass domain," *IEEE Journal on Selected Areas in Communications*, vol. 10, no. 8, pp. 1236–1242, Oct. 1992.

[Kaleh-89] G. K. Kaleh, "Simple coherent receivers for partial response continuous phase modulation," *IEEE Journal on Selected Areas in Communications*, vol. 7, no. 9, pp. 1427–1436, Dec. 1989.

[Kamal-13] F. Kamal, *Using 5.9 GHz DSRC to Aid the Elderly in Vehicular Environments*, Master Thesis, Dept. of Electrical and Computer Eng., University of Alberta, Alberta, Canada, 2013.

[Kamath] S. Kamath and J. Lindh, "*Measuring Bluetooth Low Energy Power Consumption*," Appl. Note AN092, Texas Instruments.

[Krishnapura-98] N. Krishnapura, S. Pavan, C. Mathiazhagan, and B. Ramamurthi, "A baseband pulse shaping filter for Gaussian minimum shift keying," in *Proceedings of the 1998 IEEE International*

Symposium on Circuits and Systems (ISCAS'98), Monterey, CA, May. 1998, vol. 1, pp. 249–252.

[Laurent-86] P. Laurent, "Exact and approximate construction of digital phase modulations by superposition of amplitude modulated pulses (AMP)," *IEEE Transactions on Communications*, vol. 34, no. 2, pp. 150–160, Feb. 1986.

[Leon-Garcia] Alberto Leon-García, *Probability, statistics, and random processes for electrical engineering*. New Jersey, USA: Prentice Hall, 2008.

[Liang-97] J.-W. Liang, B. C. Ng, J.-T. Chen, and A. Paulraj, "GMSK linearization and structured channel estimate for GSM signals," in *Military Communications Conference (MILCOM'97)*, Monterey, CA, Nov. 1997, vol. 2, pp. 817–821.

[Lin-15] J. Lin, T. Talty, and O. K. Tonguz, "On the potential of Bluetooth low energy technology for vehicular applications," *IEEE Communications Magazine*, vol. 53, no. 1, pp. 267–275, Jan. 2015.

[Lin-15] J.-r. Lin, T. Talty, and O. K. Tonguz, "On the potential of bluetooth low energy technology for vehicular applications*," IEEE Communications Magazine*, vol. 53, no. 1, pp. 267–275, Jan. 2015.

[Linz-96] A. Linz and A. Hendrickson, "Efficient implementation of an I-Q GMSK modulator," *IEEE Transactions on Circuits and Systems II: Analog and Digital Signal Processing*, vol. 43, no. 1, pp. 14–23, Jan. 1996.

[Mengali-95] U. Mengali and M. Morelli, "Decomposition of M-ary CPM signals into PAM waveforms," *IEEE Transactions on Information Theory*, vol. 41, no. 5, pp. 1265–1275, Sep. 1995.

[More-10] A. Helge More, "Bluetooth Low Energy: Wireless Connectivity for Medical Monitoring," *Journal of Diabetes Science and Technology*, vol. 4, pp. 457–463, Mar. 2010.

[Morsi-09] K. Morsi, X. Huagang, and G. Qiang, "Performance Estimation and Evaluation of Bluetooth Frequency Hopping Selection Kernel," in *2009 Joint Conferences on Pervasive Computing (JCPC)*, Taipei, China, Dec. 2009, pp. 461 – 466.

[Murota-81] K. Murota and K. Hirade, "GMSK modulation for digital mobile radio telephony," *IEEE Transactions on Communications*, vol. 29, no. 7, pp. 1044–1050, Jul. 1981.

[Nelson-08] T. Nelson, E. Perrins, and M. Rice, "Near optimal common detection techniques for shaped offset QPSK and Feher's QPSK," *IEEE Transactions on Communications*, vol. 56, no. 5, pp. 724–735, May 2008.

[Nielsen-10] J. S. Nielsen and B. Freund-Hansen, *SDR Platform for Wireless Cooperative Protocols*, Master Thesis, Department of Electronic Systems, Aalborg University, Aalborg, Denmark, 2010.

[Noha-05] Ibrahim Noha, *Bluetooth receiver design based on Laurent's decomposition*, Ph.D. Thesis, Dept. of Electrical and Comp. Eng., American University of Beirut, Beirut, Lebanon, 2005.

[Papoulis-91] Papoulis, Athanasios. *Probability, Random Variables and Stochastic Processes*. Third Edition. New York, USA: Mc Graw Hill, 1991.

[Peterson-02] B. W. Peterson, D. R. Stephens, and W. H. Tranter, "DFSE equalization of dual-h CPM over UHF MILSATCOM channels," in *Military Communications Conference (MILCOM 2002)*, Anaheim, USA, Oct. 2002, vol. 2, pp. 1406–1411 vol.2.

[Picod-14] J. M. Picod, A. Lebrun, and J.C. Demay, "Bringing Software Defined Radio to the penetration testing community," *in BlackHat USA*, Las Vegas, Nevada, Aug. 2014.

[Proakis-01] J.G. Proakis, *Digital Communications*. San Diego, CA: Mc Graw Hill, 2001.

[Proakis-08] J. G. Proakis and M. Salehi, *Digital Communications*, 5th ed. San Diego, CA: Mc Graw Hill, 2008.

[Ramírez-Pérez-11] A. Ramírez-Pérez*, Desarrollo del procesador de banda base del estándar Bluetooth*, Master Thesis, Centro de Investigación y de Estudios Avanzados del Instituto Politécnico Nacional Unidad Guadalajara, Jalisco, México, 2011.

[Ramírez-Pérez-16] A. Ramírez-Pérez, R. Parra-Michel, A. Rodríguez-García, and L. F. González-Pérez, "A new single and multi-h CPM transmitter*," IEEE Transactions on Circuits and Systems I: Regular Papers*, vol. 63, no. 99, pp. 1–11, Apr. 2016.

[Rappaport-02] T. S. Rappaport, *Wireless Communications: Principles and Practice*, 2nd ed. New Jersey, USA: Prentice Hall, 2002.

[Riley-94] T. A. D. Riley and M. A. Copeland, "A simplified continuous phase modulator technique," *IEEE Transactions on Circuits and Systems II*: Analog and Digital Signal Processing, vol. 41, no. 5, pp. 321–328, May 1994.

[Rimoldi-88] B. E. Rimoldi, "A decomposition approach to CPM," *IEEE Transactions on Information Theory*, vol. 34, no. 2, pp. 260–270, Mar. 1988.

[Rimoldi-91] B. Rimoldi, "Exact formula for the minimum squared Euclidean distance of CPFSK," *IEEE Transactions on Communications*, vol. 39, no. 9, pp. 1280–1282, Sep. 1991.

[Robinson-08] D. J. S. Robinson, *An Introduction to Abstract Algebra*. Walter de Gruyter, Aug. 2008.

[Roel-02] S. Roel, H. Fokke, and S. Kees, "Bluetooth Demodulation Algorithms and their Performance," in *2nd Karlsruhe Workshop on Software Radios*, Karlsruhe, Germany, Mar. 2002.

[Ryan-13] M. Ryan, "Bluetooth: With Low Energy comes Low Security," in *7th USENIX Workshop on Offensive Technologies*, Washington, D.C, Aug. 2013.

[S.I.G. Bluetooth-19] S.I.G. Bluetooth, "*Bluetooth core specification, version 5.1*," 2019.

[Safak-17] M. Safak, *Digital Communications*. Chichester, UK: John Wiley & Sons, 2017.

[Sánchez-13] J. M. Sánchez Venegas*, Diseño e implementación de la capa MAC del estandar bluetooth*, Master Thesis, Centro de Investigación y de Estudios Avanzados del Instituto Politécnico Nacional Unidad Guadalajara, Jalisco, México, 2013.

[Shi-10] C. Shi and X. Du, "A simplified detection algorithm for full response STC-CPM system," in *2010 2nd International Conference on Future Computer and Communication*, vol. 1, pp. 378–381, May 2010.

[Sirca-16] S. Sirca, *Probability for Physicists*. Ljubljana, Slovenia: Springer, 2016.

[Spill-07] D. Spill, *Implementation of the Bluetooth stack for software defined radio, with a view to sniffing and injecting packets*, Master Thesis, University College London, London, England, 2007.

[Sundberg-86] C. E. Sundberg, "Continuous phase modulation," *IEEE Communications Magazine*, vol. 24, no. 4, pp. 25–38, Apr. 1986.

[Svedek-09] T. Svedek, M. Herceg, and T. Matic, "A simple signal shaper for GMSK/GFSK and MSK modulator based on sigma-delta look-up table," *Radioengineering Journal*, vol. 18, no. 2, pp. 230–237, Jun. 2009.

[Svensson-84] A. Svensson, Sundenberg C., and T. Aulin, "A class of reduced-complexity Viterbi detectors for partial response continuous phase modulation," *IEEE Transactions on Communications*, vol. 32, Oct-1984.

[Taki-06] M. Taki and M. B. Nezafati, "A new method for Detection of LDPC Coded GMSK Modulated Signals," in *2006 International Conference on Wireless Communications, Networking and Mobile Computing*, Wuhan, China, Sep. 2006, pp. 1–5.

[Telemetry Group-16] *Part I: Telemetry Standards Document*, Telemetry Group standard 106-15-2016.

[Townsend-14] K. Townsend, C. Cufí, and R. Davidson, *Getting Started with Bluetooth Low Energy: Tools and Techniques for Low-Power Networking*. Sebastopol, CA: O'Reilly Media, 2014.

[Valencia-Velasco-20] J. Valencia-Velasco, O. Longoria-Gandara, R. Aldana-Lopez and L. Pizano-Escalante, "Low-Complexity Maximum-Likelihood Detector for IoT BLE Devices," in *IEEE Internet of Things Journal*, vol. 7, no. 6, pp. 4737-4745, June 2020

[Virk-01] K. Munir Virk, "*Design of an integrated gfsk demodulator for a Bluetooth receiver*," Project Report, Technical University of Denmark, Lyngby, Denmark, 2001.

[Votis-16] C. I. Votis, V. Christofilakis, and P. Kostarakis, "SIMO channel performance evaluation on indoor environment at 2.4 GHz," *International Journal of Electronics*, vol. 103, no. 4, pp. 648–666, 2016.

[Wardle-05] Mason B. Wardle, *A PAM Decomposition of Weak CPM*, Ph. D. Thesis, Dept. of Electrical and Comp. Eng., Brigham Young University, Utah, USA, 2005.

[Watteyne-10] T. Watteyne, S. Lanzisera, A. Mehta, and K. S. J. Pister, "Mitigating Multipath Fading through Channel Hopping in Wireless Sensor Networks," in *2010 IEEE International Conference on Communications*, May 2010.

[Wiechowsk-14] L. Wiechowsk, K. Siwiec, J. Kopanski, and W. A. Pleskacz, "Simulink Model of GFSK Demodulator Based on Time-to-Digital Converter," in *21st International Conference "Mixed Design of Integrated Circuits and Systems*," Lublin, Poland, Jun. 2014.

[Wiesler-98] A. Wiesler, R. Machauer, and F. Jondral, "Comparison of GMSK and linear approximated GMSK for use in software radio," *IEEE 5th International Symposium on Spread Spectrum Techniques and Applications*. vol. 2, pp. 557–560, Sep. 1998.

[Wilhelmsson-17] L. R. Wilhelmsson, M. M. Lopez, and D. Sundman, "NB-WiFi: IEEE 802.11 and Bluetooth Low Energy Combined for Efficient Support of IoT," in *2017 IEEE Wireless Communications and Networking Conference (WCNC)*, pp. 1–6, Mar. 2017.

[Wright-06] J. Wright. (2006). I Can Hear You Now: Eavesdropping on Bluetooth Headset [Online]. Available: http://www.willhackforsushi.com/presentations/icanhearyounow-sansns2007.pdf.

[Xia-03] B. Xia, C. Xin, W. Sheng, A. Y. Valero-Lopez, and E. Sanchez-Sinencio, "A GFSK demodulator for low-IF Bluetooth receiver," *IEEE Journal of Solid-State Circuits*, vol. 38, no. 8, pp. 1397–1400, Aug. 2003.

[Xian-08] L. Xian, R. Punnoose, and H. Liu, "Simplified receiver design for STBC binary continuous phase modulation," *IEEE Transactions on Wireless Communications*, vol. 7, no. 2, pp. 452–457, Feb. 2008..

[Xiaoxia-01] Xiaoxia Zhang and M. P. Fitz, "Space-time code design with CPM transmission," in *Proceedings. 2001 IEEE International Symposium on Information Theory*, pp. 327-329, Jun. 2001.

[Xiong-06] F. Xiong*, Digital Modulation Techniques*. Norwood, MA: Artech House, Jan. 2006.

[Yang-11] R. H.-H. Yang, M.-T. Lee, C.-K. Lee, and S.-J. Chern, "A novel class of continuous-phase modulation (CPM) with separable phase property," in *2011 International Symposium on Intelligent Signal Processing and Communications Systems (ISPACS)*, Chiang Mai, Thailand, Dec. 2011, pp. 1–6.

[Yang-15] R. H. H. Yang, M. T. Lee, C. K. Lee, and S. J. Chern, "Low complexity receiver for continuous phase modulation using 3RC-TL phase shaping pulses," in *2015 International Symposium on Intelligent Signal Processing and Communication Systems (ISPACS)*, Nov. 2015, pp. 608–613.

[Zanella-14] A. Zanella, N. Bui, A. Castellani, L. Vangelista, and M. Zorzi, "Internet of Things for Smart Cities," *IEEE Internet of Things Journal*, vol. 1, no. 1, pp. 22–32, Feb. 2014.

[Zhang-03] X. Zhang and M. P. Fitz, "Space-time code design with continuous phase modulation," *IEEE Journal on Selected Areas in Communications*, vol. 21, no. 5, pp. 783–792, Jun. 2003.

[Zhao-05] Wanlun Zhao and G. B. Giannakis, "Reduced complexity receivers for layered space-time CPM," *IEEE Transactions on Wireless Communications*, vol. 4, no. 2, pp. 574–582, Mar. 2005.

Author Index

Subject Index

T

V